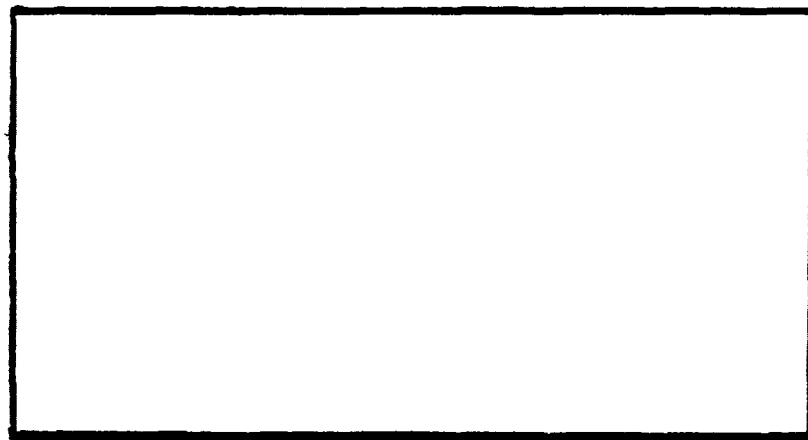
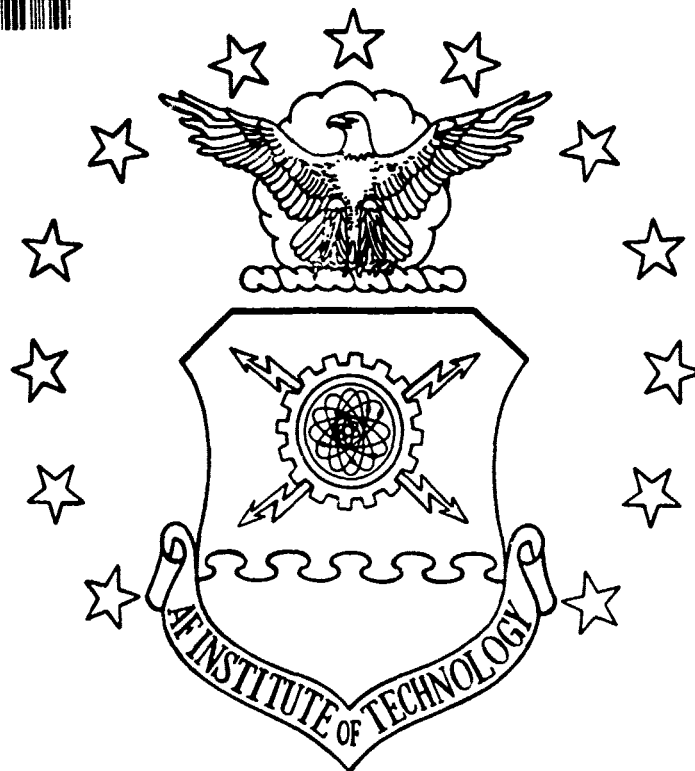


AD-A266 543



1



DISTRIBUTION STATEMENT A
Approved for public release
Distribution Unlimited

DTIC
S **ELECTE** **D**
JUL 08 1993
B

DEPARTMENT OF THE AIR FORCE
AIR UNIVERSITY

AIR FORCE INSTITUTE OF TECHNOLOGY

Wright-Patterson Air Force Base, Ohio

AFIT/GAE/ENY/93J-02

**A COMPARISON OF COMPUTATIONAL AND EXPERIMENTAL
DATA FOR A SUBSCALE HIGH SPEED PROPULSIVE NOZZLE
AT LOW MACH NUMBERS**

THESIS

Yonghee Hyun
Major, ROKAF

AFIT/GAE/ENY/93J-02

Approved for public release, distribution unlimited

93 7 02 006

93-15352


164 pgs

**A COMPARISON OF COMPUTATIONAL AND EXPERIMENTAL DATA FOR
A SUBSCALE HIGH SPEED PROPULSIVE NOZZLE AT LOW MACH NUMBERS**

THESIS

Presented to the Faculty of the School of Engineering

of the Air Force Institute of Technology

Air University

In Partial Fulfillment of the

Requirements for the Degree of

Master of Science in Aeronautical Engineering

Yonghee Hyun, B.A.E

Major, ROKAF

June 1993

DTIC DOCUMENT REQUESTED 8

Accession For	
NTIS GPA&I	<input checked="checked" type="checkbox"/>
DTIC TAB	<input type="checkbox"/>
Unannounced	<input type="checkbox"/>
Justification	
By	
Distribution/	
Availability Codes	
Dist	Special
A-1	

Approved for public release; distribution unlimited

Acknowledgments

In completing this thesis, I had a great deal of help from others. First of all, I would like to thank my advisor, Captain John H. Doty, for his sincere guidance to keep me on a track during my research and for patience during my unexpected visits. Especially, I would like to express thanks to Dr. Datta Gaitonde, whose advice and instruction convinced the computer code to run properly, and who always took time to answer my questions. I also wish to acknowledge Lt. Col. Gerald A. Hasen and Dr. Paul I. King, the members of my thesis committee, for their kind suggestions.

Additionally, I would like to thank Bruce Cochran for allowing me to borrow the experimental model and the Schlieren pictures which helped me gain confidence in my research. Also, I appreciate the effort of Lt. John Soe, who taught the GRIDGEN package and read the original manuscript carefully.

I would like to thank the Korean Air Force and my senior officers who gave me the opportunity to study in the United States. Additionally, I would like to thank my family and my wife's family members for their continuous support and encouragement in the Morning Calm. Finally, I would like to express deeply my appreciation to my wife, Mi-sun, my son, Seung-gyu, and my daughter, So-youn, for their sacrifices and endurance that enabled me to complete this research. Most of all though, my thanks go to God. Only His gifts have enabled me to accomplish everything as much as I have.

Yonghee Hyun

TABLE OF CONTENTS

Acknowledgments	ii
List of Figures	v
List of Tables	xi
List of Symbols	xii
Abstract	xiv
I. INTRODUCTION	1
1.1 Background	1
1.2 Purpose	3
1.3 Scope	3
1.3 Approach	5
II. GOVERNING EQUATIONS AND NUMERICAL METHODS	13
2.1 Governing Equations	13
2.2 Discretization	16
2.3 Numerical Flux Split Scheme	19
2.3.1 Flux-Vector Splitting (Van Leer)	19
2.3.2 Flux-Difference Splitting (Roe)	23
III. ANALYSIS OF NOZZLE/COWL FLOW FIELDS	26
3.1 Nozzle/Cowl Model	26
3.2 Numerical Problem Formulation	30
3.2.1 Geometry Definition and Grid Generation	30
3.2.2 Boundary and Initial Conditions	35
3.3 Computer Code Description	37
3.4 Solution Procedure	39
IV. COMPUTATIONAL RESULTS	46
4.1 Grid Resolution Effects	48
4.2 Influence of Initial Conditions	49
4.3 Mach Number Effects	50
4.4 Nozzle Cowl Effects	52
4.5 Nozzle Pressure Ratio (NPR) Effects	53
V. EXPERIMENTAL AND NUMERICAL ANALYSIS	70
5.1 Mach Number Effects	71
5.1.1 Supersonic Effects	71
5.1.2 Subsonic Effects	74

5.2	Nozzle Cowl Effects	75
5.3	NPR Effects	76
VI.	CONCLUSIONS AND RECOMMENDATIONS	103
6.1	Conclusions	103
6.2	Recommendations	104
	Bibliography	106
	APPENDIX A: CN1DAT CONTROL FILE	108
	APPENDIX B: DATA FOR AFTERBODY/NOZZLE	110
	APPENDIX C: PRESSURE CONTOUR	114
	APPENDIX D: MACH NUMBER CONTOUR	131
	Vita	148

List of Figures

<u>Figure</u>	<u>Page</u>
1 - 1 Typical Hypersonic Vehicle with Airframe Integrated Nozzle	8
1 - 2 Hypersonic Nozzle/Afterbody Model Installed in the Trisonic Gasdynamics	8
1 - 3 Baseline Cowl Configuration	9
1 - 4 Long Cowl Configuration	9
1 - 5 Positive 5 Degree (+5) Cowl Configuration	10
1 - 6 Negative 5 Degree (-5) Cowl Configuration	10
1 - 7 Diagram of the Hypersonic Nozzle/Cowl Model	11
3 - 1 Hypersonic Nozzle/Afterbody Dimension and Coordinate System (Physical Domain)	27
3 - 2 Hypersonic Nozzle/Afterbody Pressure Tap Locations	28
3 - 3 Computational Domain of Nozzle/Afterbody	29
3 - 4 Addition of Ghost Point to Grid	32
3 - 5 Nozzle/Afterbody Grid with Baseline Cowl	42
3 - 6 Nozzle/Afterbody Grid with Long Cowl	43
3 - 7 Nozzle/Afterbody Grid with +5 Degree Cowl	44
3 - 8 Nozzle/Afterbody Grid with -5 Degree Cowl	45
4 - 1 Long Cowl Center-Cell Grid (151×101)	55
4 - 2 Long Cowl Center-Cell Grid (201×151)	56
4 - 3 Convergence History (Explicit)	57
4 - 4 Grid Resolution Effects: Long Cowl, $M_\infty=1.9$, NPR=7.0	58

<u>Figure</u>		<u>Page</u>
4 - 5	Grid Resolution Effects: Long Cowl, $M_\infty=3.0$, NPR=16.0	59
4 - 6	Influence of Initial Conditions: Long Cowl, $M_\infty=1.9$, NPR=7.0 . . .	60
4 - 7	Mach Number Effects: Baseline Cowl, NPR=1.0	61
4 - 8	Mach Number Effects: Baseline Cowl, NPR=3.0	62
4 - 9	Mach Number Effects: Baseline Cowl, NPR=5.0	63
4 - 10	Mach Number Effects: Baseline Cowl, NPR=7.0	64
4 - 11	Mach Number Effects: Baseline Cowl, NPR=12.0	65
4 - 12	Nozzle Cowl Effects: Baseline Cowl, $M_\infty=1.9$, NPR=7.0	66
4 - 13	Nozzle Cowl Effects: Baseline Cowl, $M_\infty=3.0$, NPR=16.0	67
4 - 14	NPR Effects: Baseline Cowl, $M_\infty=1.9$	68
4 - 15	NPR Effects: Baseline Cowl, $M_\infty=3.0$	69
5 - 1	Schematic of an Overexpanded and Underexpanded Exhaust at Supersonic Freestream Mach Number	79
5 - 2	Comparison of Experimental and Numerical Pressure Coefficients (Mach Number): Baseline Cowl, $M_\infty=1.9$, NPR=1.0	80
5 - 3	Comparison of Experimental and Numerical Pressure Coefficients (Mach Number): Baseline Cowl, $M_\infty=3.0$, NPR=1.0	81
5 - 4	Comparison of Experimental and Numerical Pressure Coefficients (Mach Number): Baseline Cowl, $M_\infty=1.9$, NPR=3.0	82
5 - 5	Comparison of Experimental and Numerical Pressure Coefficients (Mach Number): Baseline Cowl, $M_\infty=3.0$, NPR=3.0	83
5 - 6	Comparison of Experimental and Numerical Pressure Coefficients (Mach Number): Baseline Cowl, $M_\infty=1.9$, NPR=5.0	84

<u>Figure</u>		<u>Page</u>
5 - 7	Comparison of Experimental and Numerical Pressure Coefficients (Mach Number): Baseline Cowl, $M_\infty=3.0$, NPR=5.0	85
5 - 8	Comparison of Experimental and Numerical Pressure Coefficients (Mach Number): Baseline Cowl, $M_\infty=1.9$, NPR=7.0	86
5 - 9	Comparison of Experimental and Numerical Pressure Coefficients (Mach Number): Baseline Cowl, $M_\infty=3.0$, NPR=7.0	87
5 - 10	Comparison of Experimental and Numerical Pressure Coefficients (Mach Number): Baseline Cowl, $M_\infty=1.9$, NPR=12.0	88
5 - 11	Comparison of Experimental and Numerical Pressure Coefficients (Mach Number): Baseline Cowl, $M_\infty=3.0$, NPR=12.0	89
5 - 12	Three-Dimensional Effects for the Supersonic Cases: Baseline Cowl, $M_\infty=1.9$, NPR=3.0	90
5 - 13	Three-Dimensional Effects for the Supersonic Cases: Baseline Cowl, $M_\infty=3.0$, NPR=3.0	91
5 - 14	Three-Dimensional Effects for the Supersonic Cases: Baseline Cowl, $M_\infty=0.6$, NPR=3.0	92
5 - 15	Comparison of Experimental and Numerical Pressure Coefficients (Nozzle Cowl Effects): Baseline Cowl, $M_\infty=1.9$, NPR=7.0	93
5 - 16	Comparison of Experimental and Numerical Pressure Coefficients (Nozzle Cowl Effects): Long Cowl, $M_\infty=1.9$, NPR=7.0	94
5 - 17	Comparison of Experimental and Numerical Pressure Coefficients (Nozzle Cowl Effects): +5 Degree Cowl, $M_\infty=1.9$, NPR=7.0	95
5 - 18	Comparison of Experimental and Numerical Pressure Coefficients (Nozzle Cowl Effects): -5 Degree Cowl, $M_\infty=1.9$, NPR=7.0	96
5 - 19	Comparison of Experimental and Numerical Pressure Coefficients (Nozzle Cowl Effects): Baseline Cowl, $M_\infty=3.0$, NPR=16.0	97
5 - 20	Comparison of Experimental and Numerical Pressure Coefficients (Nozzle Cowl Effects): Long Cowl, $M_\infty=3.0$, NPR=16.0	98

<u>Figure</u>		<u>Page</u>
5 - 21	Comparison of Experimental and Numerical Pressure Coefficients (Nozzle Cowl Effects): +5 Degree Cowl, $M_\infty=3.0$, NPR=16.0	99
5 - 22	Comparison of Experimental and Numerical Pressure Coefficients (Nozzle Cowl Effects): -5 Degree Cowl, $M_\infty=3.0$, NPR=16.0 . . .	100
5 - 23	Comparison of Experimental and Numerical Pressure Coefficients (NPR Effects): Baseline Cowl, $M_\infty=3.0$, NPR=16.0	101
5 - 24	Comparison of Experimental and Numerical Pressure Coefficients (NPR Effects): Baseline Cowl, $M_\infty=3.0$, NPR=20.0	102
C - 1	Nozzle/Afterbody Pressure Contour: Baseline Cowl, $M_\infty=1.9$, NPR=1.0	115
C - 2	Nozzle/Afterbody Pressure Contour: Baseline Cowl, $M_\infty=3.0$, NPR=1.0	116
C - 3	Nozzle/Afterbody Pressure Contour: Baseline Cowl, $M_\infty=1.9$, NPR=3.0	117
C - 4	Nozzle/Afterbody Pressure Contour: Baseline Cowl, $M_\infty=3.0$, NPR=3.0	118
C - 5	Nozzle/Afterbody Pressure Contour: Baseline Cowl, $M_\infty=1.9$, NPR=5.0	119
C - 6	Nozzle/Afterbody Pressure Contour: Baseline Cowl, $M_\infty=3.0$, NPR=5.0	120
C - 7	Nozzle/Afterbody Pressure Contour: Baseline Cowl, $M_\infty=1.9$, NPR=7.0	121
C - 8	Nozzle/Afterbody Pressure Contour: Baseline Cowl, $M_\infty=3.0$, NPR=7.0	122
C - 9	Nozzle/Afterbody Pressure Contour: Baseline Cowl, $M_\infty=1.9$, NPR=12.0	123
C - 10	Nozzle/Afterbody Pressure Contour: Baseline Cowl, $M_\infty=3.0$, NPR=12.0	124

<u>Figure</u>		<u>Page</u>
C - 11	Nozzle/Afterbody Pressure Contour: Long Cowl, $M_\infty=1.9$, NPR=7.0	125
C - 12	Nozzle/Afterbody Pressure Contour: +5 Degree Cowl, $M_\infty=1.9$, NPR=7.0	126
C - 13	Nozzle/Afterbody Pressure Contour: -5 Degree Cowl, $M_\infty=1.9$, NPR=7.0	127
C - 14	Nozzle/Afterbody Pressure Contour: Baseline Cowl, $M_\infty=3.0$, NPR=16.0	128
C - 15	Nozzle/Afterbody Pressure Contour: Long Cowl, $M_\infty=3.0$, NPR=16.0	129
C - 16	Nozzle/Afterbody Pressure Contour: +5 Degree Cowl, $M_\infty=3.0$, NPR=16.0	130
D - 1	Nozzle/Afterbody Mach Number Contour: Baseline Cowl, $M_\infty=1.9$, NPR=1.0	132
D - 2	Nozzle/Afterbody Mach Number Contour: Baseline Cowl, $M_\infty=3.0$, NPR=1.0	133
D - 3	Nozzle/Afterbody Mach Number Contour: Baseline Cowl, $M_\infty=1.9$, NPR=3.0	134
D - 4	Nozzle/Afterbody Mach Number Contour: Baseline Cowl, $M_\infty=3.0$, NPR=3.0	135
D - 5	Nozzle/Afterbody Mach Number Contour: Baseline Cowl, $M_\infty=1.9$, NPR=5.0	136
D - 6	Nozzle/Afterbody Mach Number Contour: Baseline Cowl, $M_\infty=3.0$, NPR=5.0	137
D - 7	Nozzle/Afterbody Mach Number Contour: Baseline Cowl, $M_\infty=1.9$, NPR=7.0	138

<u>Figure</u>		<u>Page</u>
D - 8	Nozzle/Afterbody Mach Number Contour: Baseline Cowl, $M_\infty=3.0$, NPR=7.0	139
D - 9	Nozzle/Afterbody Mach Number Contour: Baseline Cowl, $M_\infty=1.9$, NPR=12.0	140
D - 10	Nozzle/Afterbody Mach Number Contour: Baseline Cowl, $M_\infty=3.0$, NPR=12.0	141
D - 11	Nozzle/Afterbody Mach Number Contour: Long Cowl, $M_\infty=1.9$, NPR=7.0	142
D - 12	Nozzle/Afterbody Mach Number Contour: +5 Degree Cowl, $M_\infty=1.9$, NPR=7.0	143
D - 13	Nozzle/Afterbody Mach Number Contour: -5 Degree Cowl, $M_\infty=1.9$, NPR=7.0	144
D - 14	Nozzle/Afterbody Mach Number Contour: Baseline Cowl, $M_\infty=3.0$, NPR=16.0	145
D - 15	Nozzle/Afterbody Mach Number Contour: Long Cowl, $M_\infty=3.0$, NPR=16.0	146
D - 16	Nozzle/Afterbody Mach Number Contour: +5 Degree Cowl, $M_\infty=3.0$, NPR=16.0	147

List of Tables

<u>Table</u>		<u>Page</u>
1 - 1	Parametric Cases for Numerical Methods	12
3 - 1	Solution Integration Parameters	38
3 - 2	Flowfield Conditions	39
3 - 3	Boundary Conditions	39
3 - 4	Control Parameters	39
B - 1	Data for Mach Number Effects	111
B - 2	Data for Nozzle Cowl Effects	112
B - 3	Data for NPR Effects	113

List of Symbols

a	Speed of Sound
A	Flux Vector Jacobian Matrix
B	Flux Vector Jacobian Matrix
C_p	Coefficient of Pressure
D	Difference Operator: $Df = f_{i+1/2} - f_{i-1/2}$
e	Specific Internal Energy
E_t	Total Energy
f	Similarity Momentum Function
F	Inviscid Flux Vector
F_v	Viscous Flux Vector
G	Inviscid Flux Vector
G_v	Viscous Flux Vector
J	Jacobian Matrix
k	Thermal Conductivity
M_∞	Freestream Mach Number
p_∞	Freestream Static Pressure
p_{Tn}	Total Pressure of Nozzle Exhaust
p_i	Local Pressure
q	Heat Transfer Rate per unit area; Dynamic Pressure, Equation (3-11)
Q	Heat; Volume Flow Rate
Q	Corresponding Matrix of Eigenvectors, Equation (2-31)

RE	Reynolds Number
T_{wall}	Wall Temperature
u	Cartesian Coordinate X-component of Velocity
v	Cartesian Coordinate Y-component of Velocity
U	Density, Momentum, and Energy Vector

Greek

α	Angle of Attack
δ	Difference Operator: $\delta f = f^{n+1} - f^n$
$\delta_{i,j}$	Kronecker Delta
λ	Second Coefficient of Viscosity
λ_i	Eigenvalue
Λ	Eigenvalue Matrix
μ	First Coefficient of Viscosity
ρ	Density
$\tau_{i,j}$	Stress tensor
ξ	Computational Streamwise Axis
η	Computational Normal Axis

Abstract

A sub-scale nozzle/cowl configuration was previously studied experimentally to determine the low speed performance of a high speed nozzle. The current computational study investigated the same configuration and compared the experimental and computational data for the hypersonic nozzle/cowl performance at off-design conditions (subsonic through supersonic). A combination of Van Leer and Roe flux-splitting algorithm, developed at WL/FIMC was used to solve the flow field. The explicit formulation used assumed laminar, planar flow and the perfect gas equation of state. A validation for the CFD algorithm was accomplished by comparing the experimental data according to the parametric cases and the grid refinement. Grid refinement, geometry, and operating conditions all influenced the comparison of the experimental and computational data. Generally, as the Mach number and NPR (Nozzle Pressure Ratio) increased, the consistency between the experimental and the computational results showed better agreement, although the computational investigation was performed on the basis of planar, laminar flow. For the different cowl configurations, the results for baseline and -5 degrees cowl show a better agreement than the long and +5 degree cowl. But the discrepancy between the planar model and the three-dimensional model caused the inconsistency at the secondary separation bubble.

I. INTRODUCTION

1.1 Background

Hypersonic flight is a vital link in the advancement of transportation within and beyond the earth's atmosphere. Whether it requires the relatively short exposure of a re-entry vehicle, or the prolonged cruise of a hypersonic transport, surviving the aerothermodynamic environment characteristic of this flight regime constrains the design of a wide class of aerospace vehicles. The success of hypersonic air-breathing vehicles, such as the proposed National AeroSpace Plane (NASP), depends largely on efficient design of integrated propulsion and aerodynamic systems. Much of the recent increase of interest in hypersonic aerodynamics can be attributed to the effort centered around the development of the envisioned NASP (1). The NASP utilizes a supersonic combustion ramjet (SCRAMjet) propulsion system. The location of this SCRAMjet on the underside of the airframe, and the shaping of the forebody and afterbody are of prime concern to propulsion/airframe integration (2). Figure 1-1 shows an integrated airframe-propulsion concept for a hypersonic airplane, wherein the entire undersurface of the vehicle is part of the SCRAMjet engine.

Integrating airframe and propulsion systems in transonic and supersonic flight has been an area of active research over the past decade. Because these flowfields are complex and defy solution by simple analytical methods, the preponderance of reports represent joint experimental/computational studies. As discussed in Reference 3, a vehicle such as NASP, which would be required to operate efficiently at high speed, would be

heavily influenced by the aero-thermo design constraints of hypersonic flight. However, with the additional requirement of operating from a runway, the subsonic and transonic regimes of its flight envelope also become important considerations (1).

The hypersonic propulsion system operates at extremely high pressure ratios (SCRAMjet total pressure divided by ambient pressure, P_{Tt}/P_{∞}) at hypersonic speeds. The nozzle/afterbody geometry is very important in efficiently extracting thrust from the propulsion system. For hypersonic speeds, the exhaust flow is generally underexpanded, and exerts high pressure on the afterbody, which translates into additional thrust. At subsonic and low supersonic Mach numbers, the nozzle/afterbody is operating at an extremely overexpanded condition, and the pressures in the afterbody are below ambient pressure, causing drag and reducing effective thrust (4).

A major element of the integrated design is the interaction between the multiple jet plume flow, the external flow and the afterbody. Unfortunately, major portions of the hypersonic flight envelope cannot be simulated by existing ground-test facilities. Therefore, accurate and validated computational fluid dynamics (CFD) codes are needed to provide simulations of realistic flight conditions. The experimental validation data should, of course, model as many of the realistic flight conditions as possible. The validated codes can then be used to provide the most reliable predictions of the increments in performance or design parameters associated with the differences between the available test conditions and the flight environment (1). This research addresses the nozzle/afterbody integration of the hypersonic propulsion system at low speed, off-design conditions between Mach numbers of 0.6 to 3.0.

1.2 Purpose

Propulsive nozzles for hypersonic vehicles represent an extremely demanding test for CFD codes. The flowfield of a propulsive nozzle is a complicated structure with expansion waves, shock waves, contact surfaces, and the interaction among all three and surface boundaries such as the nozzle wall or cowl. Several CFD codes have been developed to resolve the propulsive nozzle flowfield of a hypersonic vehicle.

One such CFD algorithm used to obtain a computational flow solution is an explicit flux-vector splitting (FVS) and flux-difference splitting (FDS) finite volume scheme. The FVS algorithm is quite robust near sonic points with continuously differentiable flux contributions and the FDS (Roe-averaged scheme) is particularly desirable due to its shock capturing capability and stability at high Mach numbers (5).

The purpose of this research is to compare results between experimental and CFD data for hypersonic nozzle/cowl performance at off-design conditions (subsonic through supersonic). The development of the NASP will be based on the effective combination of CFD and experimental testing to arrive at the aircraft's final configuration efficiently and with a large degree of confidence.

1.3 Scope

This research effort compares the computational data obtained from the flux splitting code with experimental data for a hypersonic propulsive nozzle flowfield. Cochran (4) conducted experiments investigating the low speed, off-design performance

of a generic two-dimensional hypersonic nozzle/afterbody configuration in the Wright Laboratory (WL) Two-Foot Trisonic Gasdynamic Facility.

In the numerical method, the flow in the two-dimensional hypersonic nozzle is assumed to be unsteady and laminar at zero degrees angle of attack and may have complex shock wave interactions. It also involves strong shock - laminar boundary-layer interactions which may result in separated regions. The major interests in the CFD simulation data of the experimental results will be the comparison of the length and thickness of the separation bubble on the top surface of the nozzle. The fluid in the nozzle was treated as a calorically and thermally perfect gas.

The present investigation of the nozzle/cowl CFD code was conducted for three parametric cases: Mach number effects, nozzle cowl configuration effects, and nozzle pressure ratio (NPR) effects. The parametric test matrices for numerical implementation are presented in Table 1-1. The Mach number effects have a Mach number range of subsonic and supersonic. The subsonic cases included Mach numbers of 0.6 and 0.8, while the supersonic cases were Mach numbers of 1.9 and 3.0. To determine the effects of the nozzle lower cowl, four different cowl configurations were tested: the baseline (BL, no extended cowl) (Figure 1-3), the long (L, 0.5 inch straight extension) (Figure 1-4), the positive 5 degrees (+5, 0.5 inch extension angled 5 degrees toward the nozzle centerline) (Figure 1-5), and the negative 5 degree (-5, 0.5 inch extension angled 5 degrees away from the nozzle centerline) (Figure 1-6) Photographs of the cowls installed on the model are shown in Figure 1-2. The NPR effects for the baseline cowl configuration were conducted for Mach numbers 0.6, 0.8, 1.9, and 3.0, respectively. The NPR is the ratio of

nozzle exhaust flow total pressure (P_{Tn}) and the tunnel static pressure.

The initial external and internal (nozzle) flowfield values were determined by applying the uniform freestream conditions on the nozzle/afterbody ramp surface and the internal nozzle flow conditions at a five probe total pressure rake (Figure 1-7). The rake location is 3.25 inches upstream of the nozzle throat to measure the internal nozzle flow total pressure. The nozzle flow total pressure equals the average of these five probes. Nozzle/afterbody ramp surface pressure were measured at desired NPR. The significant area of interest in comparison of numerical and experimental model was the consistency. The algorithm, implemented by Gaitonde (7), is also quite robust relative to grid skewness and is accurate to second order in both space and time. Numerical pressure from the CFD code will be compared to the experimental data. Additionally, Mach numbers will be obtained by the numerical solutions. The calculations and post processing were performed on the Silicon Graphics Workstations at the AFIT Computer Lab.

1.4 Approach

The performance of two flux-split algorithms in unsteady two-dimensional perfect gas laminar flows are investigated for this research. The flux-vector split method of Van Leer and the flux-difference split method of Roe are applied due to their demonstrated accuracy in the prediction of similar high speed flows.

The flowfield was initially calculated with the Van Leer method, which exhibits shock structures spanning no more than two interior cells, whereas Roe's scheme may violate the entropy condition near sonic or stagnation points. Numerical convergence is

based on the computed pressure and heat transfer on nozzle surface. When the solutions in the investigation properly converged to a steady state, the control parameter for flux splitting method is converted from Van Leer's scheme to Roe's flux-difference splitting, which is based upon accurate prediction of wave interactions between interfaces through a linearized equation.

A sequence of grids is utilized to perform a grid resolution study and the results are compared with experimental values. The formulation is finite-volume with second order accuracy obtained with MUSCL (Monotonic Upstream Schemes for Conservation Laws) approach in conjunction with a limiter to prevent oscillations. The advantages of the MUSCL approach usually accrue for two reasons (5). The fluxes are split according to the local cell interface Mach number. Also, the split fluxes are generally less differentiable than conserved variables when transitioning through sonic and stagnation points. Viscous terms are centrally differenced: the solution is marched in time to steady state with a two stage Runge-Kutta scheme. An implicit Gauss-Seidel line relaxation scheme is also incorporated in the code (7), although this scheme was not used in the present investigation.

The centerline pressures on the afterbody ramp were used for data comparisons between numerical method and experimental, because of the higher density of available data in this region (4). The main parameter for comparison was the pressure coefficient of the nozzle/afterbody ramp, C_p , in dimensionless form, which was calculated from the locally measured static pressure, the upstream wind tunnel test section, and the dynamic pressure, respectively. Numerical results were obtained using the finite volume scheme,

where the flow properties indicate values at each cell center.

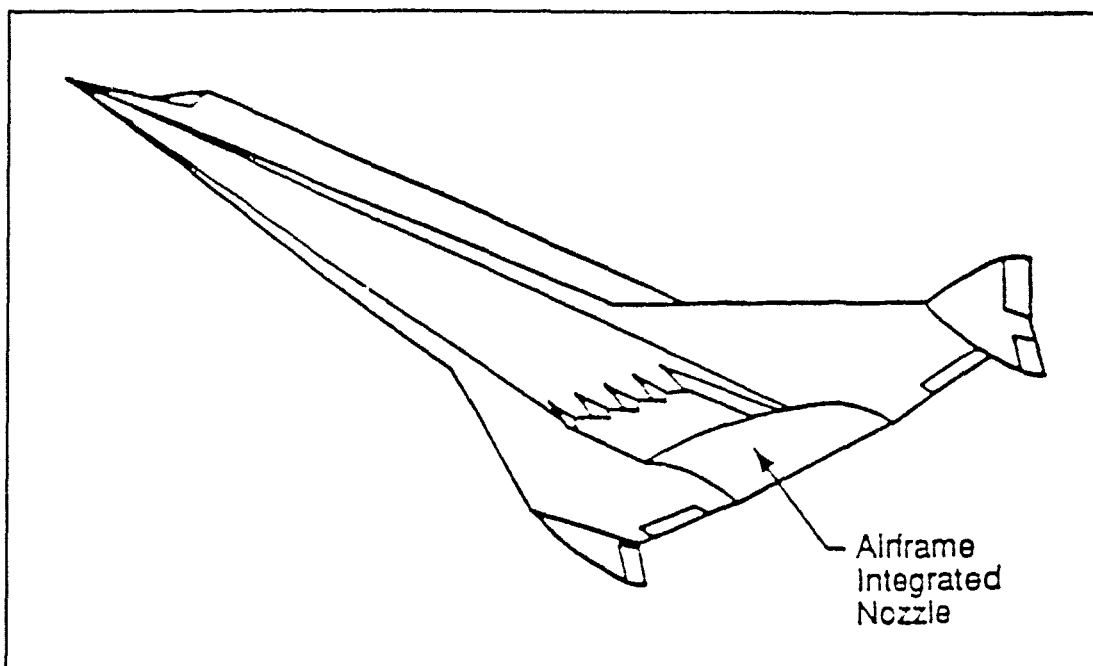


Figure 1-1 Typical Hypersonic Vehicle with Airframe Integrated Nozzle

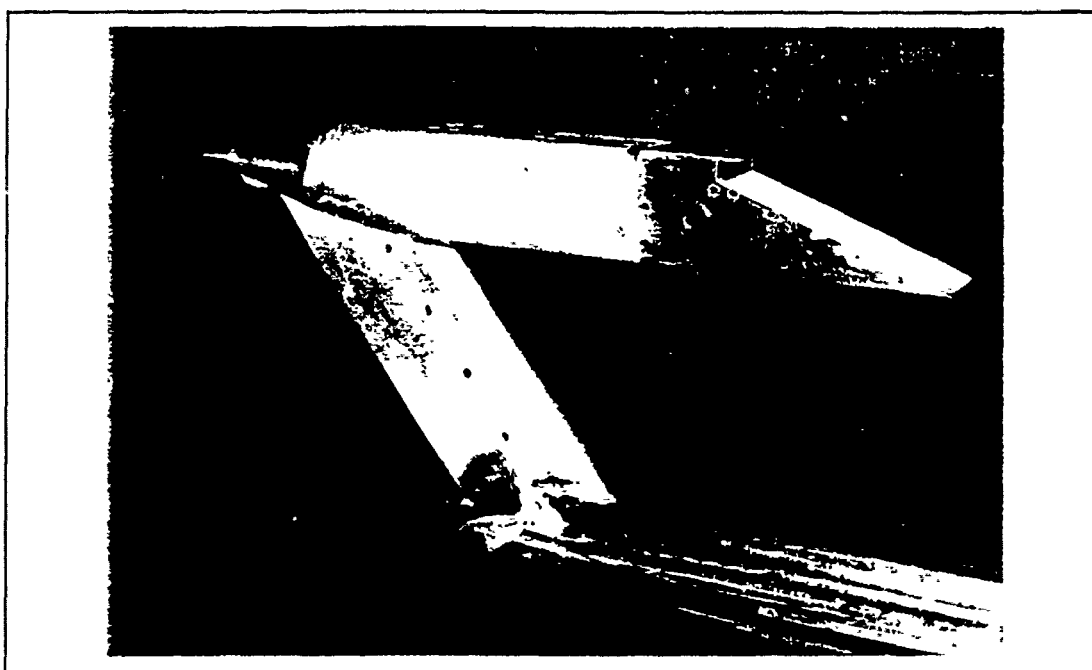
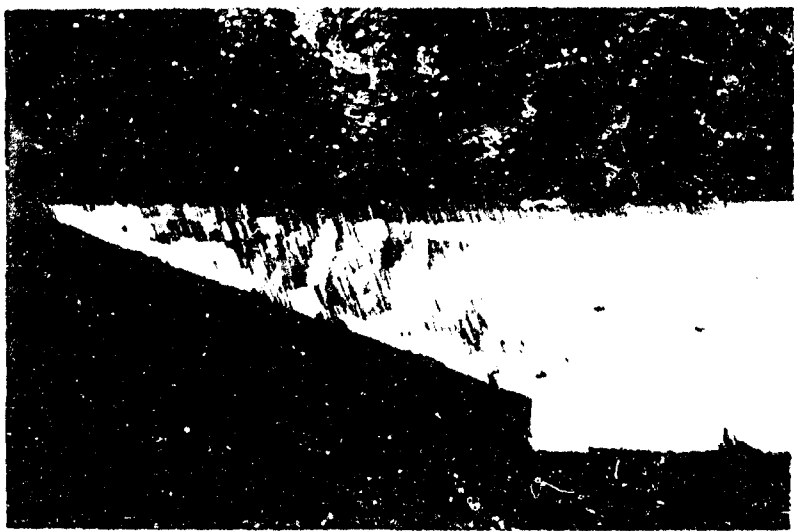
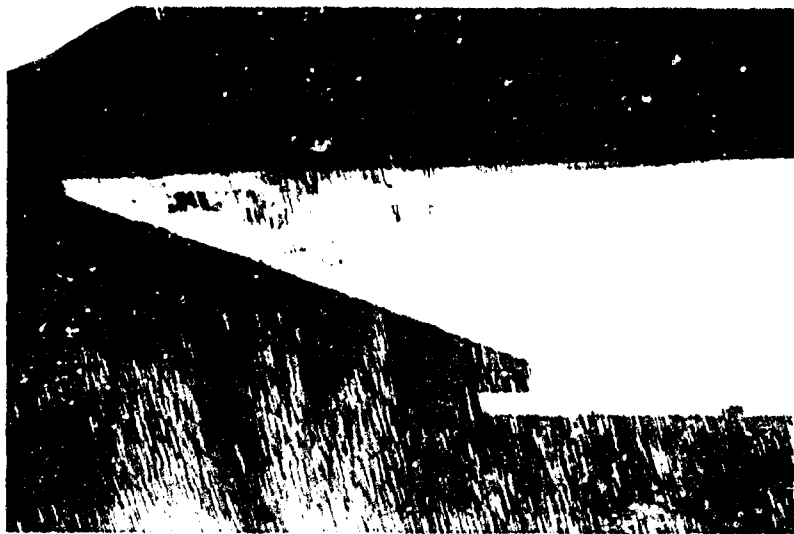


Figure 1-2 Hypersonic Nozzle/Afterbody Model Installed in the Trisonic Gasdynamics Facility



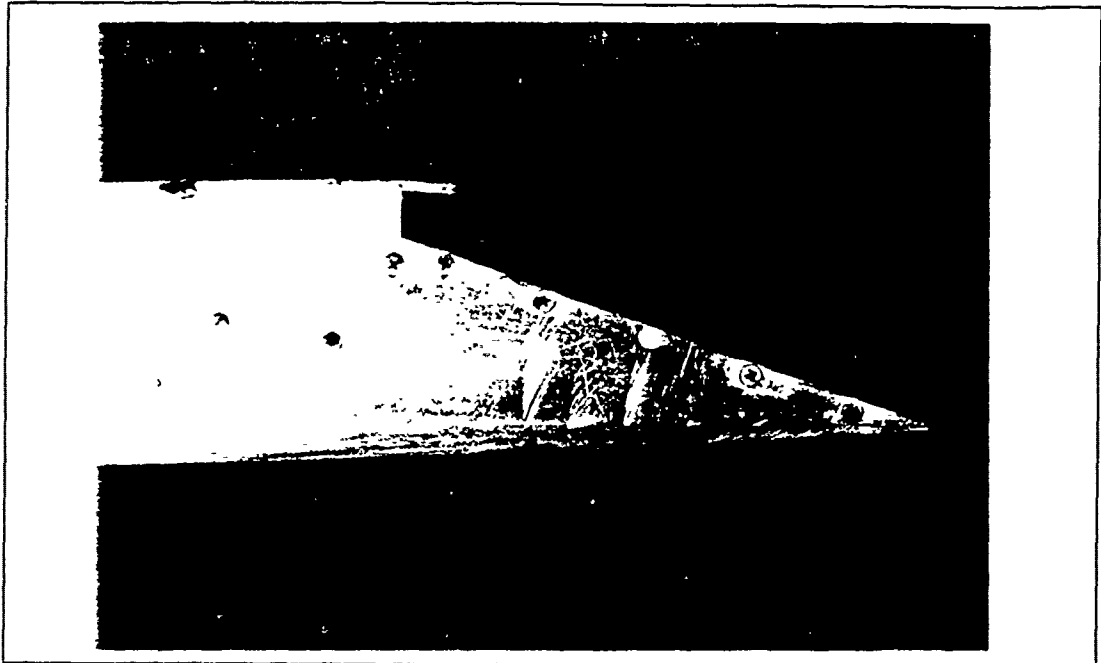


Figure 1-5 Positive 5 Degree (+5) Cowl Configuration

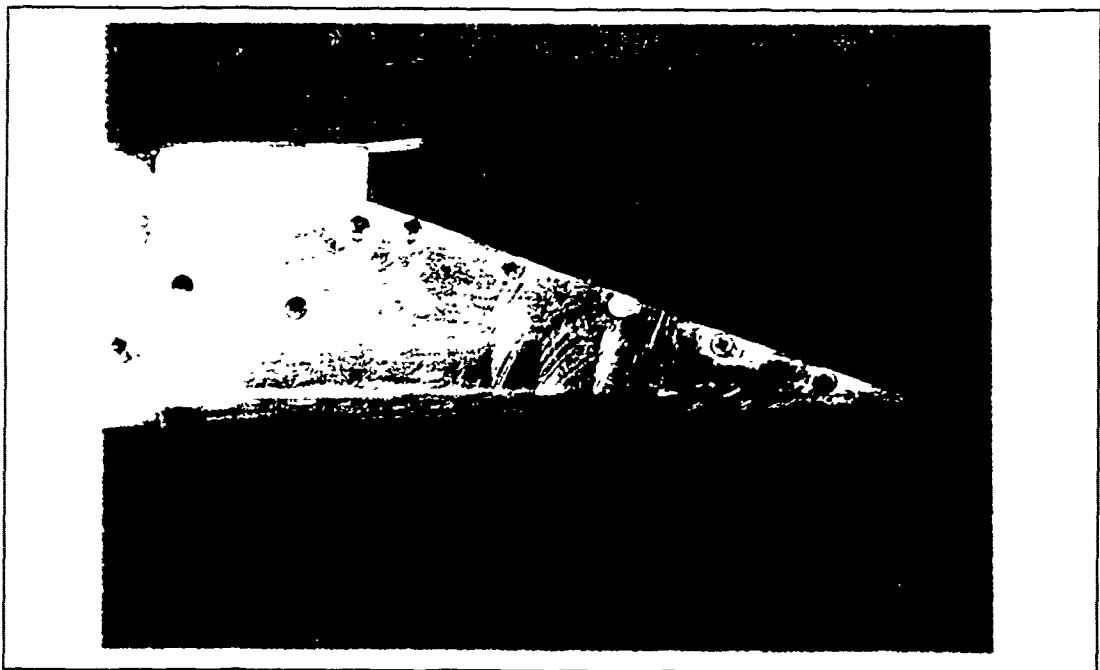


Figure 1-6 Negative 5 Degree (-5) Cowl Configuration

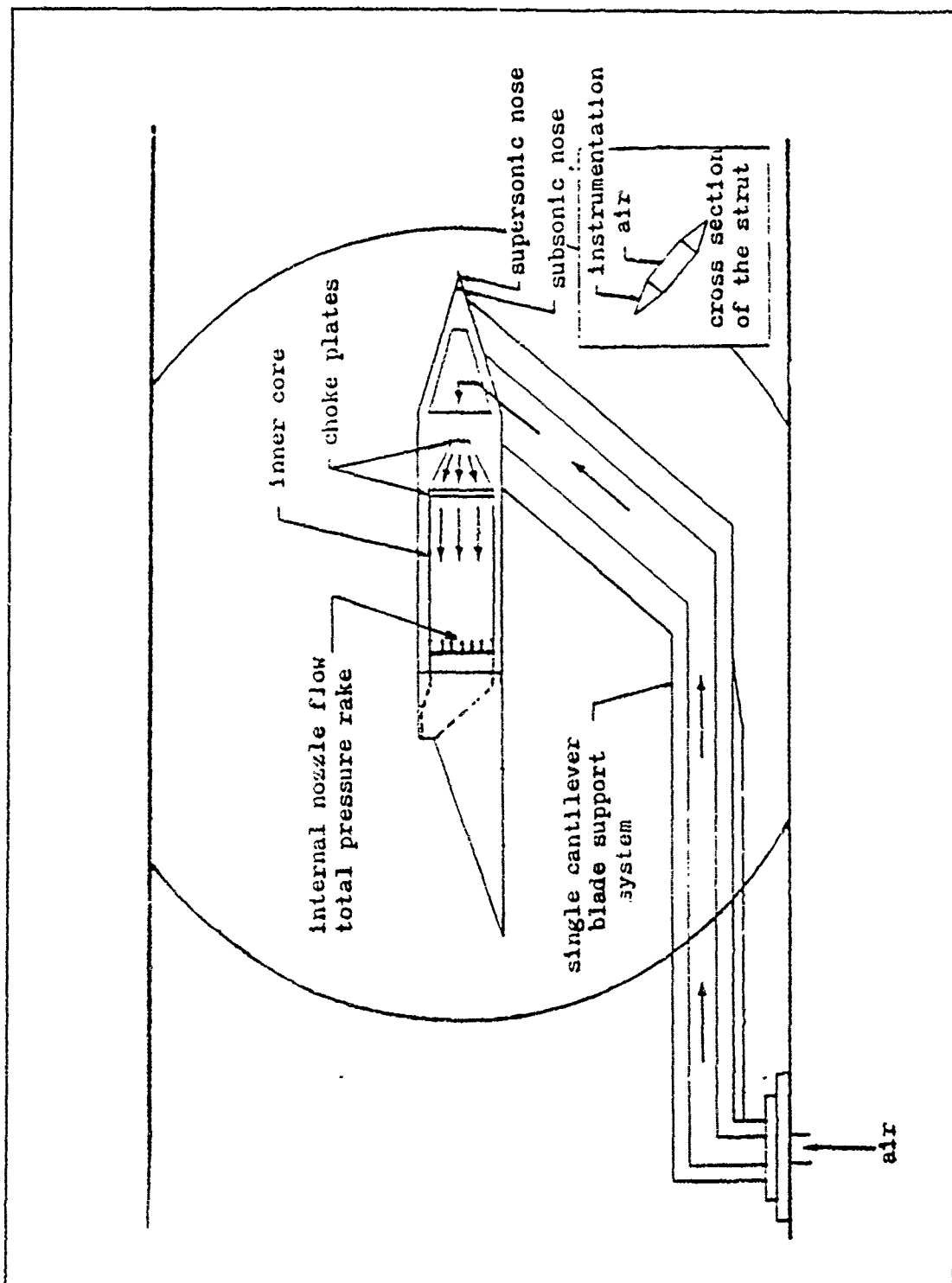


Figure 1-7 Diagram of the Hypersonic Nozzle/Afterbody Model

Table 1-1 Parametric Cases for Numerical Methods

CASE 1 : Mach Number Effects				
NPR 0.9	MACH 0.6	MACH 0.8	MACH 1.9	MACH 3.0
3.0	0.6	0.8	1.9	3.0
5.0	0.6	0.8	1.9	3.0
7.0	×	×	1.9	3.0
12.0	×	×	1.9	3.0
CASE 2 : Nozzle Cowl Effects				
MACH 0.6	BASELINE	LONG	+5 DEG	-5 DEG
0.8	BASELINE	LONG	+5 DEG	-5 DEG
1.9	BASELINE	LONG	+5 DEG	-5 DEG
3.0	BASELINE	LONG	+5 DEG	×
CASE 3 : NPR Effects				
MACH 0.6	NPR 0.9	NPR 2.0	NPR 3.0	NPR 4.9
0.9	0.8	3.0	5.0	6.1
1.9	0.9	5.0	7.0	12.1
3.0	0.9	5.1	12.2	20.3

II. GOVERNING EQUATIONS AND NUMERICAL METHODS

2.1 Governing Equations

The compressible form of the Navier-Stokes equations adequately describes aerodynamic flow at standard temperature and pressure. By neglecting body forces and heat sources, the unsteady, viscous compressible form of the Navier-Stokes equations may be written (10):

$$\frac{\partial \rho}{\partial t} + \frac{\partial \rho u_j}{\partial x_j} = 0 \quad (\text{Continuity equation}) \quad (2-1)$$

$$\frac{\partial \rho u_i}{\partial t} + \frac{\partial \rho u_i u_j}{\partial x_j} + \frac{\partial p}{\partial x_i} - \frac{\partial \tau_{ij}}{\partial x_j} = 0 \quad (\text{Momentum equation}) \quad (2-2)$$

$$\frac{\partial e}{\partial t} + \frac{\partial (E_t + p)}{\partial x_j} - \frac{\partial (u_i \tau_{ij} - q_j)}{\partial x_j} = 0 \quad (\text{Energy equation}) \quad (2-3)$$

$$p = f(e, \rho) = f\left(\frac{E_t}{\rho} - \frac{\bar{u}^2}{2}, \rho\right) \quad (\text{Equation of state}) \quad (2-4)$$

where indicial notation has been used (repeated indices are summed) and

u_i = component of velocity in the x_i direction

τ_{ij} = viscous stress

$$\tau_{ij} = \lambda \delta_{ij} \frac{\partial u_k}{\partial x_k} + \mu \left(\frac{\partial u_i}{\partial x_j} + \frac{\partial u_j}{\partial x_i} \right) \quad (2-5)$$

where δ_{ij} = the Kronecker delta.

μ, λ = first and second coefficients of viscosity, respectively.

$$q_j = -k(\partial T / \partial x_j)$$

where k = coefficient of thermal conductivity

The two-dimensional Navier-Stokes equations in Cartesian coordinates can be written in vector form as

$$\frac{\partial \bar{U}}{\partial t} + \frac{\partial \bar{F}}{\partial x} + \frac{\partial \bar{G}}{\partial y} = 0 \quad (2-6)$$

where the conserved variables are $\bar{U} = \{\rho, \rho u, \rho v, E_t\}^T$ and the flux vectors are separated into inviscid (F, G) and viscous (F_v, G_v) terms.

The inviscid flux vectors are

$$F = \begin{bmatrix} \rho u \\ \rho u^2 + p \\ \rho uv \\ (E_t + p)u \end{bmatrix} \quad G = \begin{bmatrix} \rho v \\ \rho uv \\ \rho v^2 + p \\ (E_t + p)v \end{bmatrix} \quad (2-7)$$

and the viscous fluxes are

$$F_v = \begin{bmatrix} 0 \\ \tau_{xx} \\ \tau_{yx} \\ u_j \tau_{xy} + k \frac{\partial T}{\partial x} \end{bmatrix} \quad G_v = \begin{bmatrix} 0 \\ \tau_{xy} \\ \tau_{yy} \\ u_j \tau_{xy} + k \frac{\partial T}{\partial y} \end{bmatrix} \quad (2-8)$$

The perfect gas equation-of-state closes the set of equations

$$p = (\gamma - 1) \rho e \quad e = E_t / \rho - \frac{1}{2}(u^2 + v^2) \quad (2-9)$$

The molecular dynamic viscosity μ is given by Sutherland's law (6):

$$\mu = C_1 \frac{T^{\frac{3}{2}}}{T + C_2} \quad (2-10)$$

where C_1 and C_2 are constants. For air, these values are $C_1 = 2.27\text{E-}08 \text{ lb}_m / (\text{ft-sec.R}^{1/2})$ and $C_2 = 198.9 \text{ R}$.

The conservation law form of the Navier-Stokes equations given in Equations (2-6) to (2-8) is more flexible than that in Equations (2-1) to (2-3) for purposes of coding the Navier-Stokes equations into a CFD algorithm: especially for the finite volume applications.

Transforming the Navier-Stokes equations from the physical space to the computational coordinate system is necessary (11). This transformation drastically simplifies the applications of the boundary conditions and may include various options on grid point clustering and orthogonality, both being extremely important for the solution of the Navier-Stokes equations, so that the equations are consistent with the computational domain. Equation (2-6) can be transformed for use in a general coordinate system (ξ, η) as follows (6):

$$\frac{\partial \bar{U}}{\partial t} + \frac{\partial \bar{F}}{\partial \xi} + \frac{\partial \bar{G}}{\partial \eta} = 0 \quad (2-12)$$

where

$$\bar{U} = J^{-1}U \quad (2-13)$$

$$\bar{F} = J^{-1}[\xi_x(F-F_v) + \xi_y(G-G_v)] \quad (2-14)$$

$$\bar{G} = J^{-1}[\eta_x(F-F_v) + \eta_y(G-G_v)] \quad (2-15)$$

and J is the Jacobian of the transformation:

$$J^{-1} = x_\xi y_\eta - x_\eta y_\xi \quad (2-16)$$

As a result, the general transformed form of Navier-Stokes equation for two-dimensions is (12):

$$\begin{aligned} & \frac{\partial}{\partial t} \left(\frac{U}{J} \right) + \frac{\partial}{\partial \xi} \left\{ \frac{1}{J} [\xi_x(F - F_v) + \xi_y(G - G_v)] \right\} \\ & + \frac{\partial}{\partial \eta} \left\{ \frac{1}{J} [\eta_x(F - F_v) + \eta_y(G - G_v)] \right\} = 0 \end{aligned} \quad (2-17)$$

2.2 Discretization

The code developed at **WL/FIMC** and applied in the present research uses several methods in conjunction with each other to discretize the Navier-Stokes equations. The viscous terms in the flux vectors are simply handled by central differences. The inviscid terms are handled by a combination of flux vector splitting and flux difference splitting as described below.

Consider the one-dimensional, inviscid model equation:

$$\frac{\partial U}{\partial t} + \frac{\partial F(U)}{\partial x} = 0 \quad (2-18)$$

A first-order explicit discretization of Equation (2-18) with the forward Euler method produces

$$\frac{U_i^{n+1} - U_i^n}{\Delta t} + \frac{F_{i+\frac{1}{2}}^n - F_{i-\frac{1}{2}}^n}{\Delta x} = 0 \quad (2-19)$$

where $F_{i+1/2}$ is derived from some combination of state of the flow at adjacent grid points [e.g. $F_{i+1/2} = \frac{1}{2}(F_i + F_{i+1})$]. Rearranging Equation (2-19) for the explicit discretization yields

$$\frac{(\delta U^n)_i}{\Delta t} = - \frac{F_{i+\frac{1}{2}}^n - F_{i-\frac{1}{2}}^n}{\Delta x} \quad (2-20)$$

where

$$\delta U^n \equiv U^{n+1} - U^n \quad (2-21)$$

The two-dimensional system in Equation (2-6) is discretized in a similar manner. In order to compute the right hand side, or residual, of the two-dimensional version of Equation (2-20), the fluxes in each direction are successively balanced. Thus

$$\begin{aligned} LHS_1 &= \frac{F_{i+\frac{1}{2}}(U^n) - F_{i-\frac{1}{2}}(U^n)}{\Delta x} \\ LHS_2 &= LHS_1 + \frac{G_{i+\frac{1}{2}}(U^n) - G_{i-\frac{1}{2}}(U^n)}{\Delta y} \end{aligned} \quad (2-22)$$

where LHS_1 refers to the left hand side of the two-dimensional version of Equation (2-20).

The left hand side of Equation (2-20) is evaluated by a two-stage Runge-Kutta scheme (Heun's method), while the right hand side of Equation (2-20) is evaluated by a combination of Van Leer's flux-vector splitting and Roe's flux-difference splitting methods.

The two-stage time stepping scheme is formulated as (13):

$$\delta U^n = - \frac{\Delta t}{\Delta x} (F_{i+\frac{1}{2}}^n - F_{i-\frac{1}{2}}^n) \quad (2-23)$$

in which

$$\begin{aligned} U^{(n+1,0)} &= U^n \\ U^{(n+1,1)} &= U^n - \alpha_1 \Delta t (F_{i+\frac{1}{2}}^{(n,0)} - F_{i-\frac{1}{2}}^{(n,0)}) \\ U^{(n+1,2)} &= U^n - \alpha_2 \Delta t (F_{i+\frac{1}{2}}^{(n,1)} - F_{i-\frac{1}{2}}^{(n,1)}) \\ U^{n+1} &= U^{(n+1,2)} \end{aligned} \quad (2-24)$$

where the second term in the superscript denotes each stage and its coefficients are $\alpha_1 = 1.0$, $\alpha_2 = 0.0$.

For robustness, especially in supersonic expansion regions, the right hand side of Equation (2-20) is initially calculated using Van Leer's flux-vector splitting method. Equation (2-20), where the inviscid flux is split into positive and negative components for appropriate upwind differencing:

$$F_{i+\frac{1}{2}} = F^+(U^L) + F^-(U^R) \quad (2-25)$$

When the solution properly converged to the steady state, the flux splitting scheme is converted to Roe's scheme (14):

$$F_{i+\frac{1}{2}} = \frac{1}{2} \left[F(U^L) + F(U^R) - \frac{1}{2} \hat{A} (U^R - U^L) \right] \quad (2-26)$$

The terms U^R and U^L , vectors of conserved variables which describe the state of the flow at each interface, are obtained from the MUSCL approach described in Section 2.3.2. The " $\hat{\cdot}$ " indicates a Roe averaged term, also described in Section 2.3.2.

2.3 Numerical Flux Split Scheme

2.3.1 Flux-Vector Splitting Scheme (Van Leer)

Flux vector splitting is a widely used technique not only to make computational schemes more robust, but also to improve the computational efficiency of finite-difference schemes with varying degrees of success. The basic aim is to split the flux vectors such that an upwind finite-difference scheme may be used at all points within the flow. This is performed by the simple method of separating the flux vectors into upwind and downwind parts.

A description of upwinding may be made by reference to the following inviscid equation (5):

$$\frac{\partial U}{\partial t} + \frac{\partial F}{\partial x} + \frac{\partial G}{\partial y} = 0 \quad (2-27)$$

where F and G are the inviscid flux vectors. Denoting the flux Jacobians by A and B

respectively, where for the first-order homogeneous property, $F = AU$ and $G = BU$,
i.e.

$$F = AU ; A = \frac{\partial F}{\partial U} \quad G = BU ; B = \frac{\partial G}{\partial U} \quad (2-28)$$

A finite-difference form of Equation (2-27) can be written as:

$$\frac{\delta U_i^n}{\Delta t} = - \left[\frac{DF_i^n}{\Delta x} + \frac{DG_i^n}{\Delta y} \right] \quad (2-29)$$

where δ and D are the time and space difference operators, respectively:

$$\begin{aligned} \delta f &\equiv f^{n+1} - f^n \\ Df &\equiv f_{i+\frac{1}{2}} - f_{i-\frac{1}{2}} \end{aligned} \quad (2-30)$$

In the Steger and Warming scheme, the first-order homogeneous, hyperbolic property of the inviscid flux is utilized to split the flux Jacobian A ,

$$A = Q^{-1} \Lambda Q \quad (2-31)$$

where Λ is a diagonal matrix consisting of the eigenvalues of A , $\Lambda = \text{diag}\{u, u+a, u-a\}$.

The eigenvalues can be decomposed into non-negative and non-positive components

$$\lambda_i = \lambda_i^+ + \lambda_i^- \quad (2-32)$$

where

$$\lambda^\pm = \frac{\lambda_i \pm |\lambda_i|}{2} \quad (2-33)$$

similarly, the eigenvalue matrix A can be decomposed into

$$\Lambda = \Lambda^+ + \Lambda^- \quad (2-34)$$

where Λ^+ is made of the non-negative contributions λ_i^+ and Λ^- is constructed of the non-positive contributions λ_i^- . This splitting of the eigenvalue matrix allows the flux vector F to be rewritten as

$$F_{i+\frac{1}{2}} = F^+(U^L) + F^-(U^R) = A^{L+}U^L + A^{R+}U^R \quad (2-35)$$

For second order accuracy, the vector of conserved variables, U^R and U^L , are obtained at the cell interfaces by extrapolation to the cell surface with the MUSCL approach of Van Leer. In order to avoid oscillations in shock regions, a limiter function that employs local conditions is used as follows (8):

$$U^L = U_i + \frac{1}{2}\tilde{\Delta}_{i-\frac{1}{2}}; \quad \tilde{\Delta}_{i-\frac{1}{2}} = g(\Delta_{j-\frac{1}{2}}, \Delta_{j+\frac{1}{2}}) \quad (2-36)$$

$$U^R = U_{i+1} - \frac{1}{2}\check{\Delta}_{i+\frac{3}{2}}; \quad \check{\Delta}_{i+\frac{3}{2}} = g(\Delta_{j+\frac{3}{2}}, \Delta_{j+\frac{1}{2}}) \quad (2-37)$$

where g is the limiter and $\Delta_{i+1/2} = U_{i+1} - U_i$. For example, Van Leer's limiter is

$$g = \frac{\Delta_{i+\frac{1}{2}} \Delta_{i-\frac{1}{2}} + \left| \Delta_{i+\frac{1}{2}} \Delta_{i-\frac{1}{2}} \right|}{\Delta_{i+\frac{1}{2}} + \Delta_{i-\frac{1}{2}} + \epsilon} \quad (2-38)$$

where ϵ is a small number to prevent division by zero. With the addition of the *minmod* limiter, the algorithm reverts to first order accuracy at shocks in order to preserve monotonicity within the solution.

Note that for locally supersonic and sonic flow on both sides of the interface (5)

$$\begin{aligned}
F^{L+} &= F^L & ; & & F^{R-} &= 0 & \text{ if } & M^L, M^R > 1 ; \\
F^{L+} &= 0 & ; & & F^{R-} &= F^R & \text{ if } & M^L, M^R < -1
\end{aligned}
\tag{2-39}$$

where M represents the local Mach number. This method is quite dissipative and also exhibits a flux discontinuity where the eigenvalues change sign.

One cause of inaccuracy in the Steger and Warming splitting is that the split-flux derivatives are discontinuous when any of the eigenvalues $\lambda_i(A)$ changes sign. This gives rise to instabilities in the numerical solution, unless some extra smoothing is built into the flux formula. To solve this problem, Van Leer developed a continuously differentiable splitting technique.

Van Leer's approach was to split the fluxes so that the forward and backward flux contributions transitioned smoothly at eigenvalue sign changes, i.e. near sonic and stagnation points. Just as for the Steger and Warming splitting, it was required that the Jacobian matrices $(\partial F^+/\partial U)$ have non-negative eigenvalues and $(\partial F^-/\partial U)$ have non-positive eigenvalues so that upwind differencing could be used for spacial derivatives. In addition, it was required that both Jacobians have one zero eigenvalue for $|M| < 1$, which leads to steady transonic shock structures with only two interior zones.

The formulas for F^\pm in one dimension are locally given in terms of the Mach number: for supersonic and sonic flow, $|M| > 1$, we again have;

$$\begin{aligned}
F^{L+} &= F^L & ; & & F^{R-} &= 0 & \text{ if } & M^L, M^R > 1 ; \\
F^{L+} &= 0 & ; & & F^{R-} &= F^R & \text{ if } & M^L, M^R < -1
\end{aligned}
\tag{2-40}$$

and for subsonic flow, $|M| < 1$

$$F^{\pm} = \begin{bmatrix} f_1^{\pm} \\ f_1^{\pm}[(\gamma-1)u \pm 2a] / \gamma \\ f_1^{\pm}v \\ f_1^{\pm}[(\gamma-1)u \pm 2a]^2 / \{2(\gamma^2-1)\} + v^2/2 \end{bmatrix} \quad (2-41)$$

where

$$f^{\pm} = \pm \rho a \left[\frac{1}{2}(M \pm 1) \right]^2 \quad (2-42)$$

2.3.2 Roe's Flux-Difference Splitting Scheme

The Roe scheme for a one dimensional system was presented in Equation (2-26),

$$F_{i+\frac{1}{2}}^n = \left[F_{i+1}^n + F_i^n - \hat{R} |\hat{\lambda}| \hat{R}^{-1} (U_{i+1}^n - U_i^n) \right] \quad (2-43)$$

Once again, higher order accuracy and limiting are achieved with the **MUSCL** approach in conjunction with a limiter. Yee (15) presents the **MUSCL** scheme using a simple, one dimensional hyperbolic equation. Starting from Equation (2-43), the **MUSCL** scheme replaces the U_{i+1} and U_i terms with $U_{i+1/2}^R$ and $U_{i+1/2}^L$, respectively. U^R and U^L are defined for second- and third-order spatial differencing by using various *slope* limiters to eliminate unwanted oscillations. A widely used limiter is the *minmod* limiter, which modifies the upwind-biased interpolation as follows:

$$U_{i+\frac{1}{2}}^R = U_{i+1} - \frac{1}{4} \left[(1-\eta) \tilde{\Delta}_{i+\frac{3}{2}} + (1+\eta) \tilde{\Delta}_{i+\frac{1}{2}} \right] \quad (2-44)$$

$$U_{i+\frac{1}{2}}^L = U_i - \frac{1}{4} \left[(1-\eta)\tilde{\Delta}_{i-\frac{1}{2}} + (1+\eta)\tilde{\Delta}_{i+\frac{1}{2}} \right] \quad (2-45)$$

The spatial order of accuracy is determined by the value of η :

$\eta = -1$: fully upwind scheme

$\eta = 0$: Fromm scheme

$\eta = 1/3$: third-order upwind-biased scheme

$\eta = 1$: three-point central-difference scheme

$$\tilde{\Delta}_{i+\frac{1}{2}} = \text{minmod}(\Delta_{j+\frac{1}{2}}, \omega \Delta_{j-\frac{1}{2}}) \quad (2-46)$$

$$\tilde{\Delta}_{i+\frac{1}{2}} = \text{minmod}(\Delta_{j+\frac{1}{2}}, \omega \Delta_{j+\frac{3}{2}}) \quad (2-47)$$

where

$$\text{minmod}(x, \omega y) = \text{sgn}(x) \cdot \max \{ 0, \min[|x|, \omega y \text{sgn}(x)] \} \quad (2-48)$$

and

$$1 \leq \omega \leq \frac{3-\eta}{1-\eta} \quad \text{with} \quad \eta \neq 1 \quad (2-49)$$

Note that $\text{sgn}(x)$ means the sign of the variable x .

The symbol " \wedge " in the above equations refers to Roe averaging, which is given by:

$$\hat{x} = \frac{\sqrt{\rho_L} x_L + \sqrt{\rho_R} x_R}{\sqrt{\rho_L} + \sqrt{\rho_R}} \quad x = \rho, u, v, \text{ and } h \quad (2-50)$$

The subscripts in Equation (2-50), L and R , refer to the components of the like subscripted vector U in Equations (2-44) and (2-45).

III. ANALYSIS OF NOZZLE/COWL FLOW FIELDS

3.1 Nozzle/cowl Model

The experimental model under consideration was analyzed by Cochran in 1988, who had as his goal the measurement of the nozzle/afterbody pressure drag force. This force was calculated from the integrated external ramp pressure coefficients (C_p) which resulted from the impingement of an overexpanded exhaust plume of the flow downstream of the nozzle throat.

The generic hypersonic nozzle/afterbody was attached to a square forebody (cross section) with a 15 degree half-angle conical section. Figure 1-2 is a photograph of the model installed in the Trisonic Gasdynamics Facility. The conical nose section had a sharp nosepiece for supersonic testing and a round nosepiece for subsonic testing. The model lengths were 23.33 and 22.16 inches for the supersonic and subsonic configurations, respectively.

The two-dimensional hypersonic nozzle/afterbody was designed to be representative of the external geometry of a hypersonic vehicle. Figure 3-1 is a side-view drawing of the nozzle/afterbody with the pertinent dimensions. The nozzle/afterbody had a straight 20 degree expansions ramp and a nozzle expansion area ratio of approximately 6.2. The internal nozzle was convergent and to facilitate fabrication resulted in a 50 degree straight convergent ramp. The nozzle/afterbody had a sharp corner at the nozzle throat to make the performance independent of throat radius. To determine the effects of the nozzle lower cowl, four different cowl configurations were tested: the baseline, the long, the positive 5 degrees, and the negative 5 degrees. The cowls have expansion area

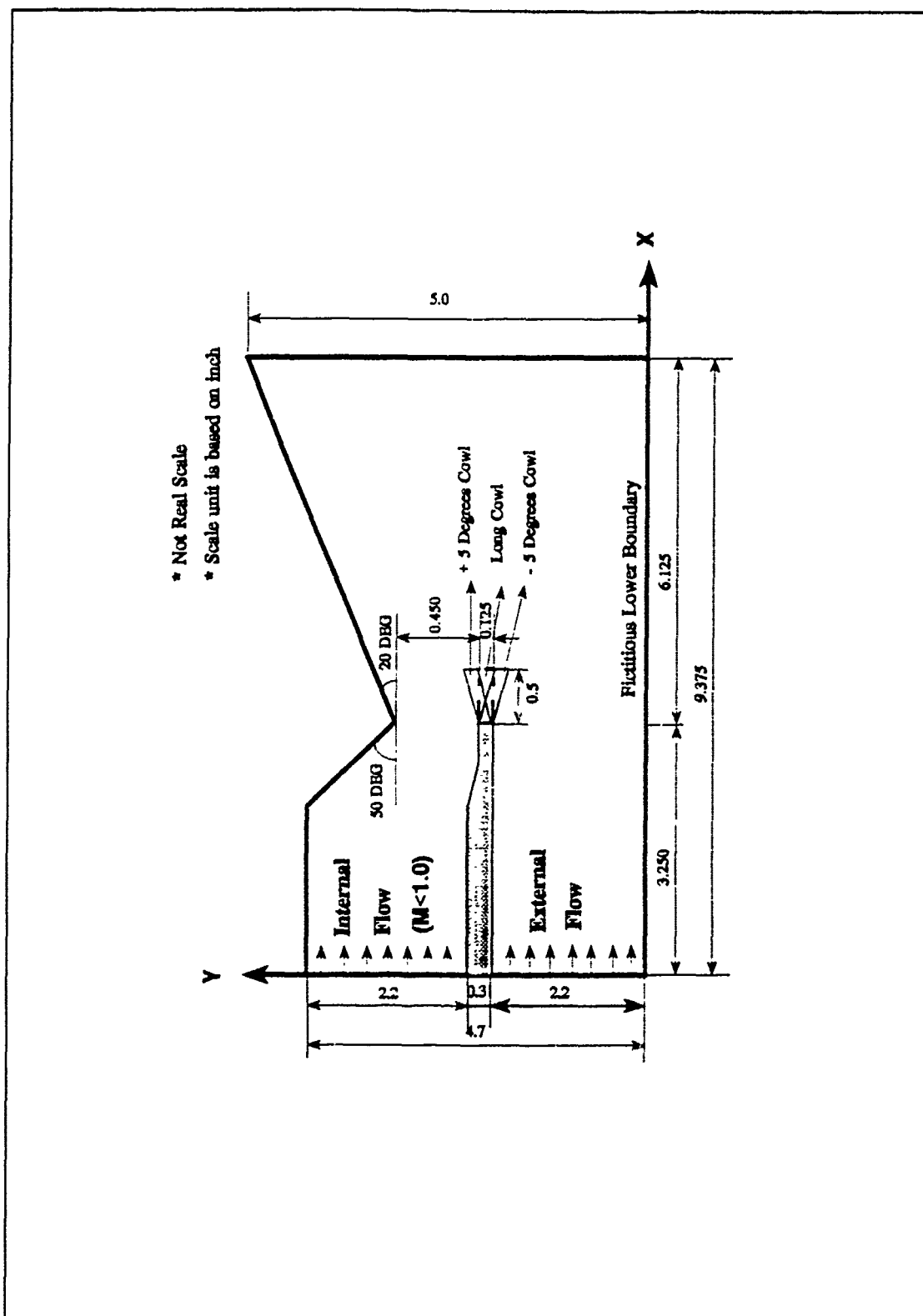


Figure 3-1 Hypersonic Nozzle/Afterbody Dimensions and Coordinate System (Physical Domain)

ratios of 1.0, 1.4, 1.3, and 1.5, respectively. The cowls were 0.125 inches thick with squared-off, blunt trailing edges.

The tests were conducted in the WL two-foot trisonic gasdynamics tunnel operating at subsonic, transonic, and supersonic speeds. The maximum Reynolds number was 2.5 million per foot for the subsonic speed and 5.0 million per foot for the supersonic speed, and the maximum dynamic pressure was 350 pounds per square foot (psf) for the subsonic speed and 1,000 psf for the supersonic speed. The stagnation temperature was maintained at approximately 100 degrees F. Pressure taps were placed in a grid pattern downstream of the nozzle assembly in the internal convergent ramp and the afterbody

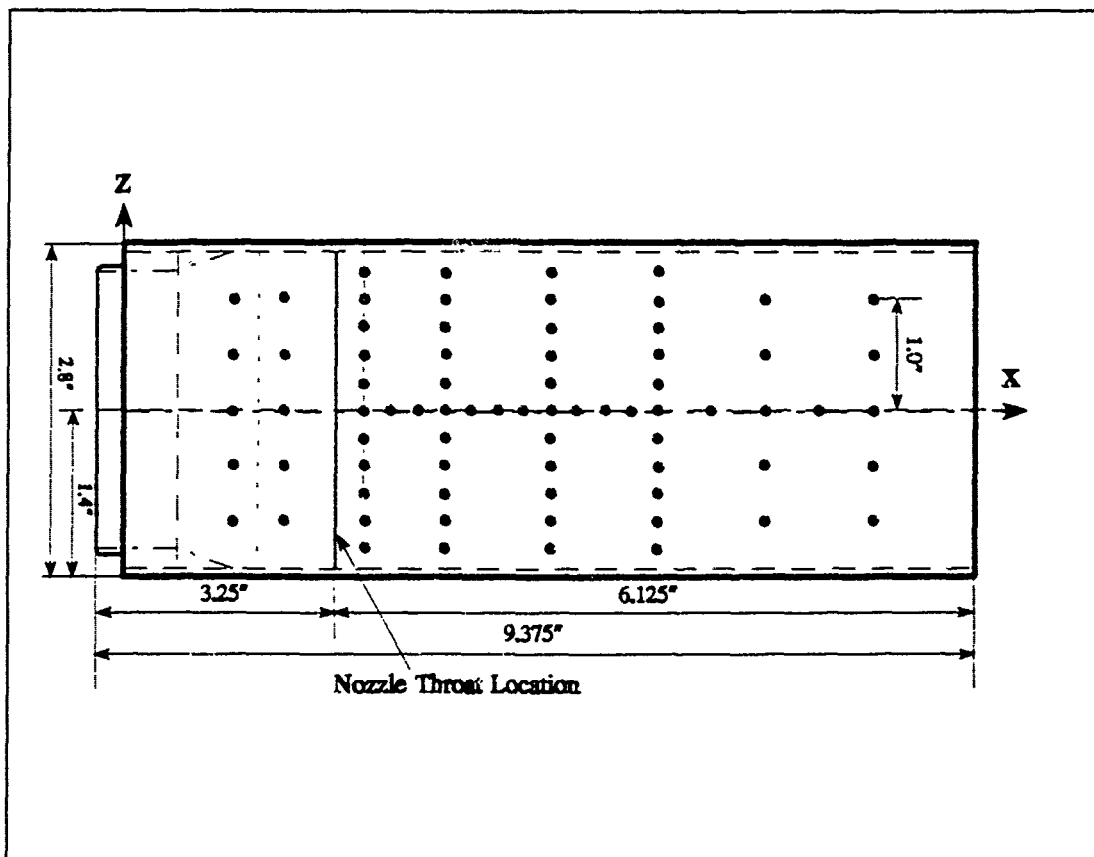


Figure 3-2 Hypersonic Nozzle/Afterbody Tap Locations

expansion ramp. In all, sixteen pressure taps were located along the centerline of the external ramp. Tap locations are shown in Figure 3-2 for the nozzle/afterbody left and right sides, respectively.

Ramp pressure distributions were obtained over a range of NPR for each Mach

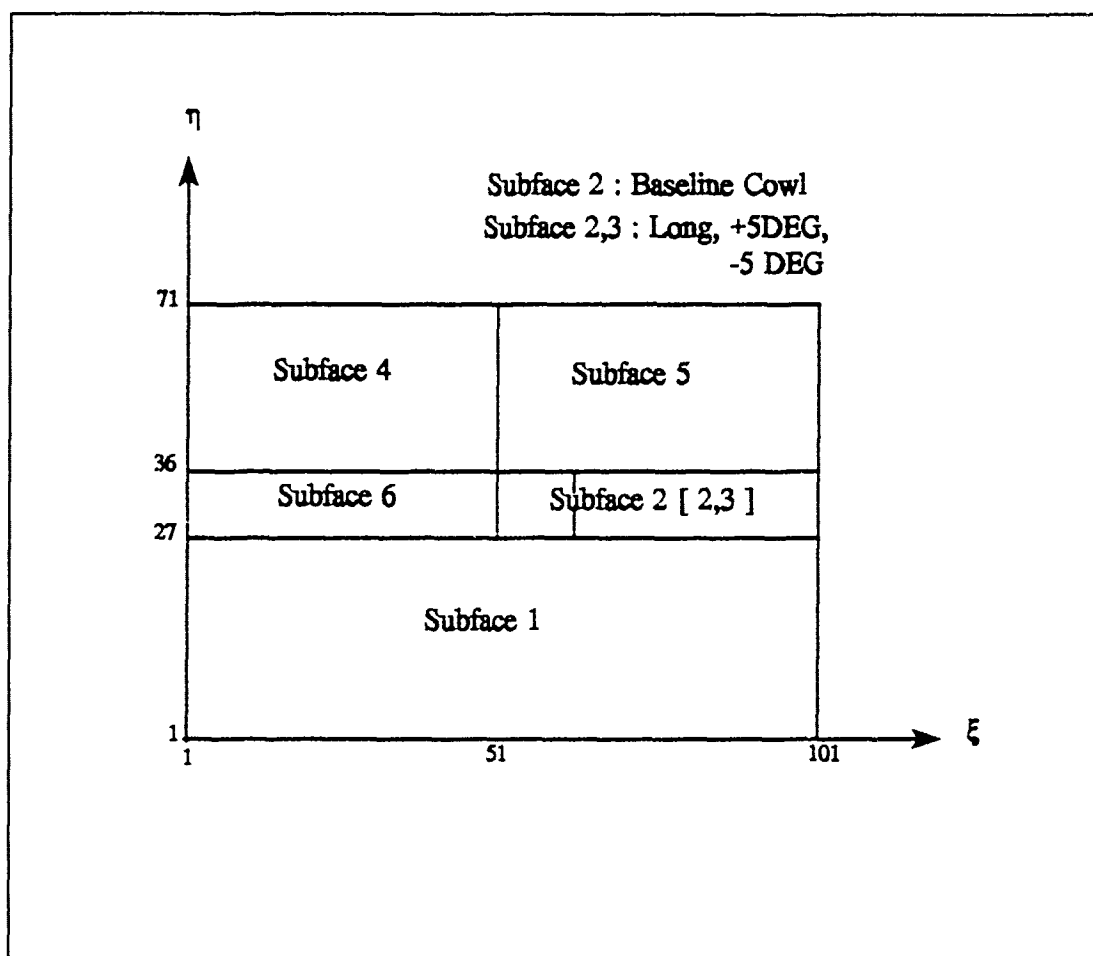


Figure 3-3 Computational Domain of Nozzle/Afterbody

number, cowl configuration, and Reynolds number. The range of NPR varies for the subsonic and supersonic Mach numbers because of the constant pressure air supply for the nozzle exhaust flow and the variation of tunnel static pressure with Mach numbers.

For each test configuration, the tunnel flow conditions (Mach and Reynolds

numbers) were established, and data for zero nozzle exhaust flow were obtained. The high pressure air was then established through the model and nozzle exhaust flow set to the desired NPR. Data were obtained at each NPR. For each test point the tunnel and nozzle flow parameters were recorded during a scanivalve reading and used for the data reduction.

The main performance parameter for the experimental test was the nozzle/afterbody pressure drag coefficient which was calculated from the integrated external ramp pressure coefficients, C_p , by assigning an appropriate area to each pressure tap location and resolving the area into the projected axial component. The centerline pressure were used because of the higher density of pressure taps which characterize the nozzle exhaust flow and the afterbody ramp pressure more accurately. The centerline pressures were also used for the test parameters (Mach number, cowl, and NPR data comparison).

The maximum errors measured in the experimental tests were 0.20% for freestream total pressure, 0.12% for freestream static pressure, 0.57% for local pressure at probe, and 0.43% for total pressure of nozzle exhaust, respectively.

3.2 Numerical Problem Formulation

3.2.1 Geometry Definition and Grid Generation

The parametric variations performed in the experiment made it possible to access the effects of nozzle afterbody, Mach number, nozzle pressure ratio, and nozzle/cowl geometry on the forces and moments induced by the impinging exhaust plumes.

Modelling the same effects computationally presented an opportunity to test the numerical method on a very practical application. The geometry for the nozzle/afterbody lent itself naturally to a Cartesian grid topology, and the two-dimensional grid was generated by GRIDGEN, a interactive graphics based method developed by the Fort Worth Division of General Dynamics Corporation for the Aeromechanics Division of the Flight Dynamics Laboratory , Wright Research and Development Center (16), now WL/FIM.

GRIDGEN is made up of four modules - GRIDBLOCK, GRIDGEN2D, GRIDGEN3D, and GRIDVUE3D. These modules enable users to create three-dimensional multiple block structures grids. However, for this problem, a quasi two-dimensional hypersonic nozzle/afterbody, only a single two-dimensional surface grid is required, GRIDGEN2D was all that was required to develop this surface grid.

GRIDGEN2D is an interactive program written primarily in FORTRAN and C for use on Silicon Graphics, Inc. (SGI) 3000 and 4D series IRIS Workstations and IBM RISC 6000 workstations. In GRIDGEN2D, the distribution of points on each of the four edge boundaries of a surface is performed, resulting in the generation of surface grids via algebraic and elliptic grid generation techniques. The block dimension $(\xi_{\max}, \eta_{\max}, \zeta_{\max})$ is entered to run in a single block. Since a single surface grid is desired, $\zeta_{\max} = 1$ was entered to eliminate the third dimension. For the primary mesh, dimensions of $101 \times 71 \times 1$ were set in the ξ , η , and ζ directions, respectively.

Figure 3-3 shows the grid information pertinent to the inviscid (Euler) and viscous (Navier Stokes) perfect-gas CFD simulations. As mentioned in (17), dividing the spatial grid into two or more zones (or subfaces) offers several advantages for solving complex

flow problems. For example, it permits the domain to be segmented into logical subunits. Appropriate placement of zones also eliminates some grid singularities, such as discontinuous body cross sections. Finer grids can be used in multiple zone calculations than in single zone calculations if the computer's main memory limits the problem size, because only one zone resides in main memory at a time. It is assumed that the nozzle/cowl geometry is composed of four main zones: the internal nozzle flow, the external flow, the solid body, and the plume (jet) boundary zone. The major section of concern is the internal nozzle flow zone, which is divided into two subfaces: surface (4) and surface (5). The boundary between surfaces (4) and (5) (i.e. the throat) was made

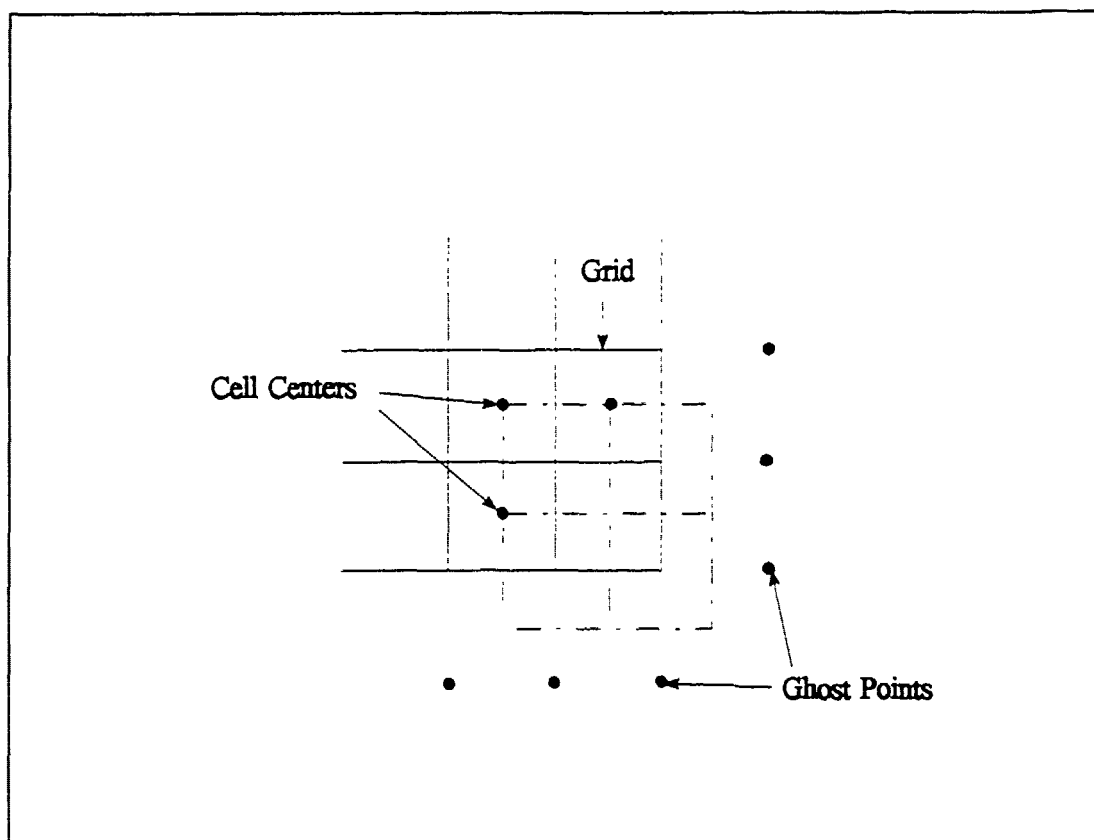


Figure 3-4 Additional Ghost Point to Grid

straight in an attempt to capture the sonic condition. At the solid body surface, the appropriate boundary conditions were applied.

The generation of grid points on a surface begins with the distribution of points on the four bounding edges of the surface. When the coordinates (x,y) have been set on all four edges, interpolation methods are employed to distribute points on the surface interior.

There are three main steps involved in the edge generation process. The first step is to define the shape of the nozzle/afterbody geometry on which the edge grid points are to be distributed. Only straight line segments were needed to define the shape of the nozzle/afterbody. In the second stage, each edge shape is divided into a number of subedges, separated by selected datapoints, called breakpoints, according to the experimental configuration. By breaking the edge into subedges, greater control of grid point placement on the edges was gained. In the third stage, grid points are distributed along each subedge.

Next, algebraic methods are used to define grid points in the interior of each surface. Among types of algebraic solvers, Transfinite Interpolation (TFI) with arclength-based interpolants was used. Essentially, this method uses interpolants based on the relative arclength between edge points, which means that points close together on the edge remain close together on the interior of the surface. This method worked very well for the majority of cases.

Further refinement of the surface interior points is made by accessing the elliptic PDE solvers. On surfaces (4) and (5), GRIDGEN2D's elliptic solver was used to reduce

grid skewness near the throat area. Thomas-Middlecoff control functions, with a relaxation factor of 0.3, were used for the smoothing, because they provided the best results. The small relaxation factor was chosen so that the changes to the grid would be slow enough that when the grid was acceptably smooth the process could be stopped. Approximately 200 iterations were required to produce an acceptable grid. The grid points were clustered not only near body and surface to provide accurate resolution of the boundary layer for viscous calculations, but also near the region where the shock is expected to form.

Figure 3-3 shows perspective views of the grid topology, which were segmented into five subfaces for a baseline cowl and six subfaces for long, +5 degree, and -5 degree cowls. Subfaces (4) and (5) had 51×36 , where 51 points in the streamwise (ξ) direction, 36 points in the normal (η) direction to the stream. For a baseline cowl, subface (2) had 51×10 . But subface (2) had 11×10 , subface (3) had 41×10 for long, +5 degree, and -5 degree cowls, respectively. Subface (1) had 101×27 . The grid totaled 7,171 points. Figure 3-5 to Figure 3-8, depicting the grids on the different nozzle/cowl configurations, are the output of GRIDGEN2D, with ghost points (points within the body surface) added as required for the computational solver. By using a preprocessor, *convgrd.f*, the grid points are converted into the cell centered points. Further, this also inverts the nozzle/afterbody configuration for subsequent convenient examination of developing phenomena with the Flow Analysis Software Toolkit (**FAST**) package under development at NASA Ames Research Center.

The ghost points mentioned above are required because cell-centered finite volume codes, such as the one used here, solve for flux as across cell faces, which requires

knowing the flow variables at cell centers, rather than at the grid points. Ghost points are added to all boundaries, so that cell centers can be calculated. Figure 3-4 illustrates the addition of ghost points to a simple grid, and the resulting network of cell centers.

3.2.2 Boundary and Initial Conditions

For each flow, the boundaries may be categorized into the following: inflow boundaries, surface boundaries, and outflow boundary.

At inflow boundaries, the flow vector $\{\rho, \rho u, \rho v, \rho e\}$ is determined according to the given external and internal freestream values. The freestream conditions were imposed on the ξ_{\min} and the η_{\max} faces. Fluxes on the freestream boundaries were calculated using the values for Mach number, temperature, and pressure assigned in the initial conditions. On the ξ_{\min} face, the inflow conditions are specified by

$$U_{i,j} = U_{\infty} \quad (3-1)$$

where U is the vector given in Equation (3-1).

Similarly, the freestream condition is given on the ξ_{\max} face by

$$U_{i,j_{\max}} = U_{\infty} \quad (3-2)$$

Alternatively, the zero gradient condition $U_{i,j_{\max}+1} = U_{i,j_{\max}}$ was used.

The boundary conditions at the nozzle/cowl surface are more complicated. The viscous terms are calculated directly from the conditions specified at the surface for temperature and zero velocity. Since the computational grid is cell centered, the conditions at the surface are imposed by setting the conditions at the ghost points just within the

surface.

$$\rho \bar{v} = 0 \quad (3-3)$$

For example, for the u -component of velocity

$$u_{1,2} = -u_{1,1}$$

Identical relations are used for other velocity component, v . Furthermore, pressure is held constant between the ghost point and the first point above the surface

$$\frac{\partial p}{\partial \eta} = 0 \quad (3-4)$$

i. e. $p_{1,1} = p_{1,2}$ corresponding to a zeroth-order implementation.

A fixed surface temperature is specified

$$T = T_{wall} \quad (3-5)$$

The inviscid fluxes on the surface calculated directly from the pressure and the metrics. Since the inviscid mass and energy fluxes normal to the surface are both zero, the fluxes are given by

$$U_{i,wall} = \begin{bmatrix} 0 \\ P\eta_x \\ P\eta_y \\ 0 \end{bmatrix} \quad (3-6)$$

At the outflow boundary, the ξ_{max} face, a no-change condition is applied. By simply setting the fluxes at the ghost point to those at the first point upstream of the

boundary, thus

$$U_{imax+1,j} = U_{imax,j} \quad (3-7)$$

Initial conditions are normally prescribed for each set of calculations by assuming the freestream conditions exist at all the grid points except at the boundaries where proper boundary conditions are applied. Initial properties - freestream pressure, Mach number, and static temperature - for the external and internal (nozzle) flow were taken from experimental data at the rake location which was 3.25 inches upstream of the nozzle throat. All properties except the nozzle static pressure were assumed to be constant, whereas the static nozzle pressure was assumed by taking the averaging value. Also, the nozzle static top and bottom pressure, which was within about 5% error compared to the average value, was calculated to verify the significance of the initial conditions.

3.3 Computer Code Description

Wright Laboratory's two-dimensional, flux-splitting, Navier-Stokes code, developed at WL/FIMC, was basically used to solve the viscous, hypersonic, nozzle/cowl problem based on the laminar flow assumption. This code was written in FORTRAN and was run on a Silicon Graphics IRIS Workstations.

Data file, *cn1dat*, was required for execution of the code. The *cn1dat* contains information, such as the version of the code to run (Navier-Stokes or Euler), whether to use an implicit or an explicit formulation, initial conditions, boundary conditions, and so forth. The *cn1dat* file has essentially four parts: solution integration parameters, flowfield conditions, boundary conditions, and control parameters. A sample *cn1dat* file can be

found in Appendix A.

Table 3-1 lists the parameters that control the implementation of the solution, particularly such things as which flux split scheme is used, i.e. Van Leer, Steger and Warming, or Roe. Other parameters include the ending iteration number, whether the flow model is Euler or Navier-Stokes, what the CFL stability criteria is, and how it is handled.

Table 3-2 details the flow field conditions, particularly the external freestream conditions and the internal nozzle freestream conditions. Table 3-3 lists the boundary condition parameters, and the node range in which they apply. Table 3-4 lists the parameters which control the iterations between printing convergence data, the grid formatting from ASCII to binary, and the output file formatting to three-dimensions to monitor the developing situation of the simulation.

Table 3-1, Solution Integration Parameters

ISWVL	Finite Difference Scheme: 3=Van Leer, 4=Roe
NEND	Number of iterations
INS	Flow model: 0=Euler, 1=Navier-Stokes
IL, JL	Grid Dimensions
CFLMAX	Maximum CFL number allowed
CFL	Starting CFL number
CFLEXP	Number of iterations before CFL doubles
ICFL	Number of iterations between CFL increases
IMPLT	Implicit vs. Explicit: 0=Explicit, 1=Implicit

Table 3-2. Flowfield Conditions

IADBWL	Flag to indicate adiabatic wall BC
TWALL	Wall temperature
ALPHA	Freestream Angle of attack
RM	Freestream Mach number
REL	Freestream Reynolds number per foot
TINF	Freestream Temperature
AINLPHA	Nozzle Angle of Attack
RINM	Nozzle Mach number
RINEL	Nozzle Reynolds number per foot
TININF	Nozzle Temperature

Table 3-3. Boundary Conditions

INS	Start and end points for a ξ Solid Body BC
JNS	Start and end points for an η Solid Body BC

Table 3-4. Control Parameters

IREAD	0=Deadstart, 1=Restart
IGRID	Grid format
IP3DOP	Plot3D output file format
MODPR	Iterations between printing convergence data

3.4 Solution Procedure

The calculations to be described were all obtained with the explicit option of the code. The numerical method used in this research is second-order accurate in space and

second-order accurate for time. Convergence is enhanced through the use of local time-stepping methods.

This algorithm provide two important advantages. First, the use of upwind flux approximations for the inviscid components (including pressure) of Navier-Stokes equations provide a method for numerically capturing shocks without the need for additional artificial damping terms which require adjustment by the user. In addition, an explicit integration scheme provides an extremely efficient numerical method on vector or parallel machines for solving systems of equations, because the dependent variables can be explicitly updated using concurrent machine operations.

The conservative variables at interior grid points must be initialized to start the iterative solution algorithm (17). The initial condition for flow variables was implemented by using their freestream properties. Since this condition is far from the converged result, a large perturbation occurs at the first time step. Stability bounds constrained the time step to a small value initially. It was then gradually increased as the solution progressed to the steady state. The code used in this investigation allows specification of the Courant-Friedrichs and Lewy (CFL) number (19), defined as

$$CFL = \frac{\Delta t}{\lambda_{\max}} \quad (3-8)$$

where λ_{\max} is the largest eigenvalue of the flux Jacobians matrices. The time step is then locally calculated from the prescribed CFL number and the maximum eigenvalue. The CFL number was initially set to a value 0.01, and increased to 0.9 for the maximum value using the explicit version of the code.

Two criteria determined convergence of the solution: the integrated root mean square (*RMS*) pressure and heat transfer values over the nozzle surface are monitored. Both must remain constant at convergence with P and Q denoting pressure and heat transfer, respectively.

$$(Q)_{RMS} = \frac{1}{IL} \sqrt{\sum_{i=1}^{IL} (Q_{i,j=surface})^2} \quad (3-9)$$

$$(P)_{RMS} = \frac{1}{IL} \sqrt{\sum_{i=1}^{IL} \left(\frac{P_{i,j=surface}}{P_{\infty}} \right)^2} \quad (3-10)$$

where IL is the number of points in ξ direction.

Convergence is assumed when $(P)_{RMS}$, $(Q)_{RMS}$ do not fluctuate more than 0.05% over a large number of iterations (typically 1,000 at CFL of 0.9, local time-stepping).

The solution of the nozzle/cowl flowfield started from freestream conditions is initiated by Van Leer's flux-splitting with continuously differentiable flux contributions at sonic or stagnation point up to 1,000 iterations. T_{wall} was assumed to be 400.6 R . After that, the solver was switched to Roe's scheme which predicted wave interactions accurately, for up to 2,000 iterations. Solutions were run on the Silicon Graphics Workstations.

The pressure coefficients were calculated from locally calculated static pressure for comparison, using the following relationship

$$C_{p_i} = \frac{p_i - p_{\infty}}{q_{\infty}} \quad (3-11)$$

where p_{∞} and q_{∞} are the tunnel test section static and dynamic pressure, respectively.

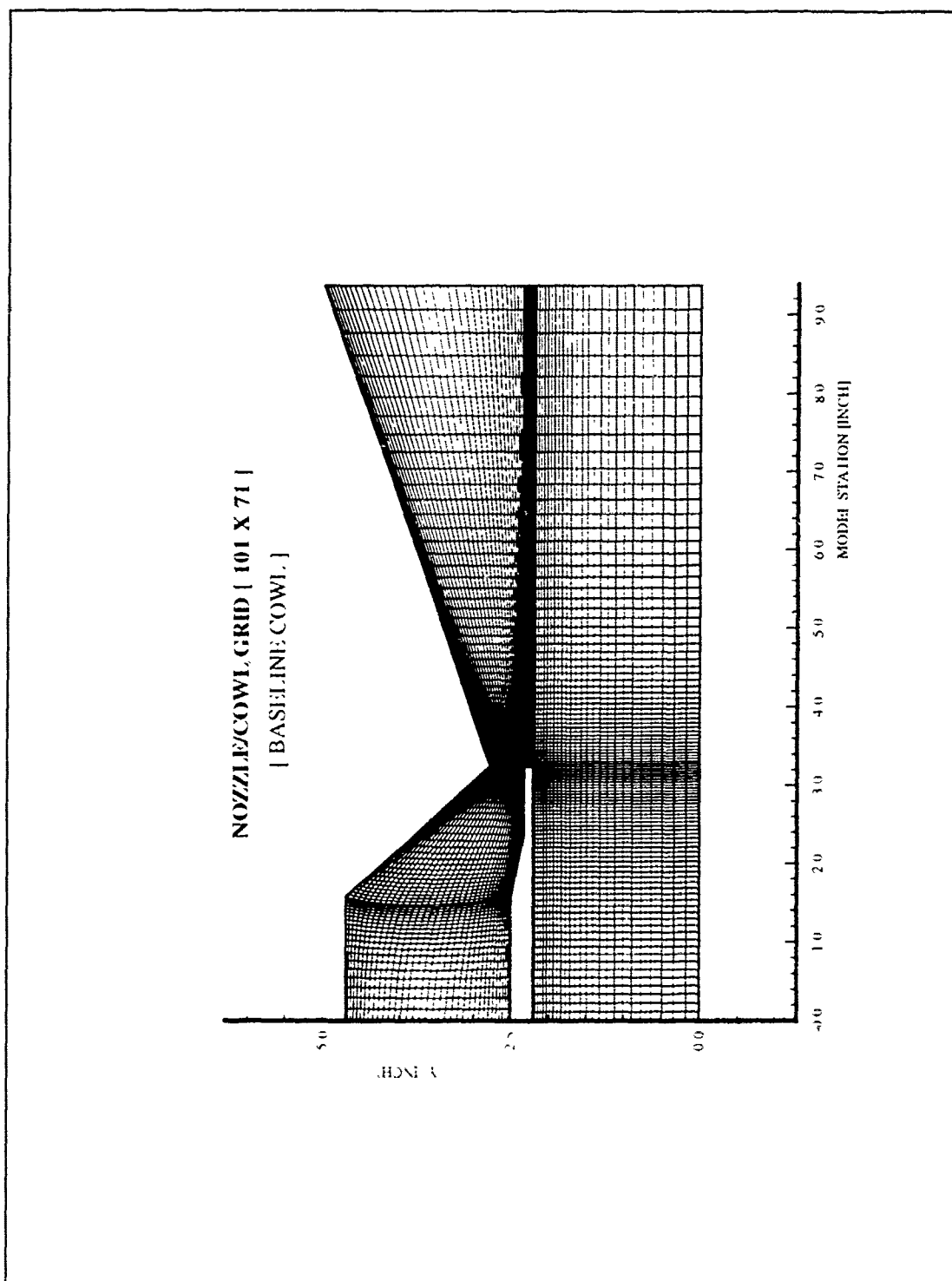


Figure 3-5 Baseline Cowl Grid

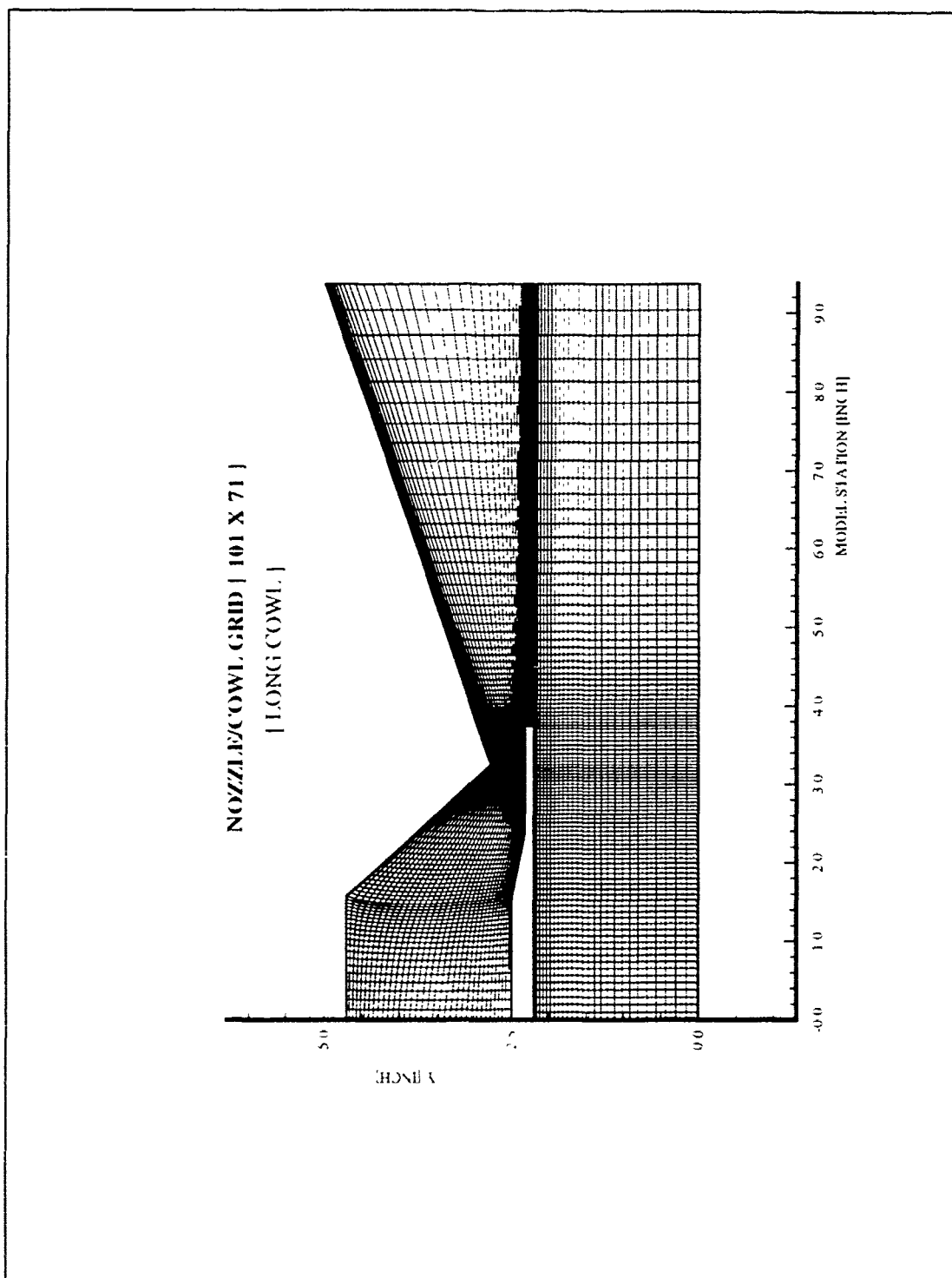


Figure 3-6 Long Cowl Grid

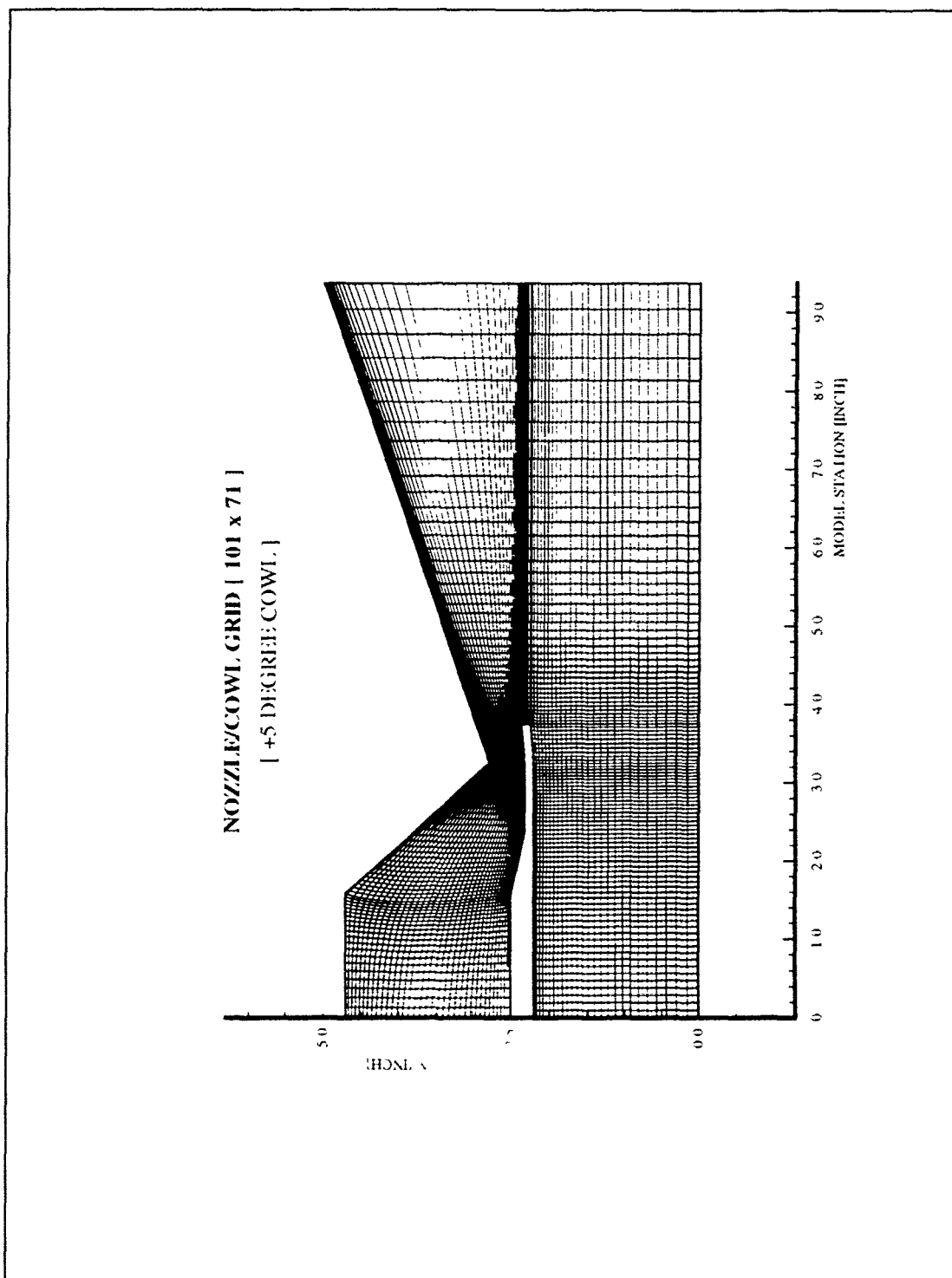


Figure 3-7 +5 Degree Cowl Grid

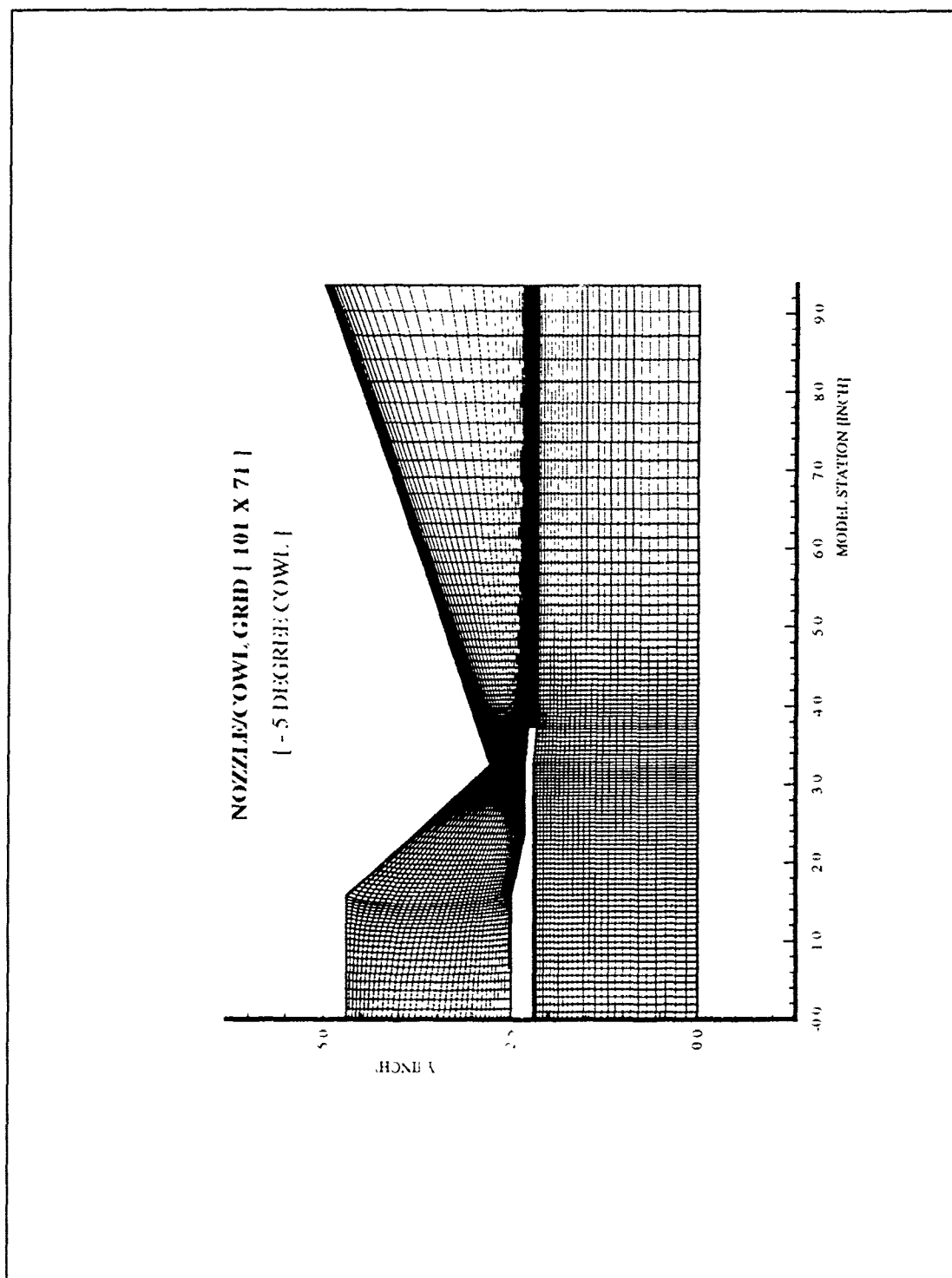


Figure 3-8 -5 Degree Cowl Grid

IV. COMPUTATIONAL RESULTS

Navier-Stokes solutions based on an explicit flux-splitting scheme were obtained for the quasi two-dimensional hypersonic nozzle/afterbody at freestream Mach numbers of 0.6, 0.9, 1.9, and 3.0 at an angle of attack of zero degrees. The external flow, the jet exhaust plume, and the internal nozzle flow were included in the calculations. Nozzle Pressure Ratios (NPRs) of 0.8 to 20.0 were investigated. In addition, four different cowl configurations were tested. In the calculations, laminar flow was assumed over the entire external surface and internal nozzle.

As a necessary step to the nozzle/afterbody investigation, the convergence of the numerical solution is based on the integrated *RMS* pressure and heat transfer over the nozzle surface. Additionally, grid independence of numerical results was tested with a series of grids. A grid refinement was performed at $M_\infty=1.9$, $NPR=7.15$ and $M_\infty=3.0$, $NPR=16.0$ on the long cowl. The *fine grid* had dimensions of 201 points in the streamwise (ξ) direction, and 151 points in the normal (η) direction to the stream, for an overall total of 30,351 points. Next, the *medium grid* had dimensions of 151 (ξ) and 101 (η), for a total of 15,251 points. Finally, the *coarse grid* had dimensions of 101 (ξ) and 71 (η) for a total of 7,171 points. The fine and medium grids based on the cell center for the finite volume scheme are shown in Figures 4-1 and 4-2.

The solution of the nozzle/cowl flowfield was initially performed with Van Leer's flux splitting, for the first 1000 iterations (Figure 4-3). Fortunately, solutions in the present investigation converged to a steady state, using local time stepping, within this 1000 iterations. Finally, the solution was fully converged with Roe's scheme. Solutions

were performed on the Silicon Graphics IRIS Workstations; the code expends about 0.23 microseconds of Central Process Unit (CPU) time per iteration per grid point for the baseline cowl and 0.27 microseconds for the long cowl ($M_\infty=1.9$, $NPR=7.0$). This calculation required 1.216 hours of CPU for Van Leer and 1.233 hours for Roe, totalling 2.449 hours.

As expected, the hypersonic nozzle exhaust flow was dominated by an initial overexpansion of the flow downstream of the nozzle throat for all test conditions. Overexpansion occurs when the atmospheric or ambient pressure is greater than the internal exhaust pressure, causing flow to disturb within the nozzle. The sudden increase in the exhaust flow area of the divergent afterbody expansion ramp and the effect of the sharp corner at the throat caused the flow to overexpand to the low pressure and moved the separation bubble near the throat. The recompression characteristic, after this expansion, depended on the parametric cases: Mach number, cowl configuration, and NPR.

Having gained some appreciation for the dynamics of overexpanded jet impingement, for the supersonic cases, it is now of interest to investigate grid resolution effects, influence of the initial conditions, and parametric variations of nozzle operating conditions. But for the subsonic cases, there was inconsistency between the experimental and the computational results due to discrepancy in the models, computational planar model and experimental three-dimensional model. Therefore, the explanation for the computational results is focused on the supersonic cases at this section. As parameters change, the plume/afterbody interaction will be altered, impacting overall performance.

4.1 Grid Resolution Effects

To study the effects of grid refinement on numerical results and the convergence of the numerical solution, a grid refinement was performed on a series of grids, 101×71 , 151×101 , and 201×151 , at $M_\infty=1.9$, $NPR=7.0$ and $M_\infty=3.0$, $NPR=16.0$ on the long cowl. The long cowl was chosen because the numerical solution is well consistent for the baseline cowl with the assumption of laminar flow. Any finite-difference method or finite volume carries with it's truncation errors arising from approximation to the differentiations (17). Obtaining numerical solutions on a series of grids tests the accuracy and uniqueness of the results on the basis of laminar boundary layer.

Comparison of pressure coefficients among solutions from the three grids and experimental data are shown in Figure 4-4 ($M_\infty=1.9$, $NPR=7.0$). The coarse grid (101×71) and medium grid (151×101) results follow similar trends as the experimental data, but fail to place the reexpansion before the peak of the compression. However, the fine grid (solid line in Figure 4-4) showed that the exhaust flow initially expanded and compressed downstream of the sharp throat. Also, it showed that the flow re-expanded slightly and recompressed until the flow reached the apex of the separation bubble, whose trends were not revealed in the coarse and medium grids. For the second case ($M_\infty=3.0$, $NPR=16.0$), the grid refinement results showed the same trends as the previous numerical results (Figure 4-5). With the encouraging results above, if the finer grid can be generated in the numerical implementation, the results should provide better agreement with the experimental data and more accurately analyze the development of the flowfield phenomena. But even though the finer grid was generated in this research, there were still

difference between the results at the separation bubble due to the difference in the assumption, which is the laminar flow in the numerical performance and the turbulent flow on the experiment. The reference (18) showed favorable results between the laminar and turbulent flow under the same conditions, i.e., two-dimensional computational model. Therefore, it was determined that the laminar flow assumption used in the CFD results was the dominant factor for the initial separation bubble regime. The remainder of the research was then performed using the medium and fine grid.

The convergence for the coarse grid, 101×71 , was already mentioned above. The medium grid converged to the steady state near 2,000 iterations and the fine grid required up to 5,000 iterations. The code requires approximately 0.14 microseconds of CPU time per iteration per grid point for the medium grid and 0.04 microseconds for the fine grid on the long cowl ($M_\infty=3.0$, $NPR=12.0$). This calculation required 5.439 hours of CPU time for medium grid and 23.261 hours for the fine grid on the Silicon Graphics IRIS Workstations.

4.2 Influence of Initial Conditions

To examine the influence of the initial conditions in the numerical implementation, different values for nozzle static pressure - the average, top, and bottom values - were used considering the two-dimensional effects only. With regards to the tolerances of errors from the experimental data, pressure was within the approximately 5% and temperature was constant.

For this purpose the NPR and Reynolds number varied along with the initial

conditions similar to tolerances for the experimental data. As with the grid resolution effects, the long cowl was chosen, since the numerical solution was well consistent to the experimental results for the baseline cowl. Pressure coefficient comparing among solutions in the different initial conditions shown in Figure 4-6 ($M_\infty=1.9$, $NPR=7.0$). Obviously, it is very hard to distinguish the differences between the different initial conditions on the numerical solutions. These results indicate that varying the initial conditions within experimental error doesn't significantly effect the results in the numerical solutions. A further study of very different initial conditions may have produced better agreement between the CFD and experimental data, but that was not the purpose of this investigation.

4.3 Mach Number Effects

The Mach number effects on the pressure coefficient distributions are presented in Figures 4-7 to Figure 4-11 (C_p versus model station plots) at specific NPRs for the baseline cowl configuration. Mach number and pressure distribution contours over all the nozzle/afterbody area are presented in Appendices C and D.

Data for the supersonic conditions (Mach number 1.9 and 3.0), Figure 4-7 (NPR approximately equal to one, i.e., flow off), shows that the external flow overexpands to the negative C_p then compresses at the same location by the separation bubble encountered downstream of the sharp throat. The data at Mach number 1.9 shows a higher rate of overexpansion and compression than for Mach 3.0 condition. For these supersonic conditions, the pressure distributions appear nearly flat after compression.

For the NPR of 3.0 and 5.0, Figures 4-8 and 4-9 show, for the supersonic conditions, that the exhaust flow continues to overexpand to a negative C_p with even higher rate than NPR 1.0 conditions. The Mach number 1.9 flow expands to a lower C_p than Mach number 3.0, but continues to have a higher rate of compression. The Mach 1.9 C_p distribution shows some recompression characteristics near $x=5.0$ caused by the second separation bubble, but the exhaust flow does not recover fully to the ambient pressure. The NPR 5.0 flow has a higher rate of compression than the NPR 3.0. The Mach 3.0 C_p distributions are nearly flat.

For Figures 4-10 and 4-11, nozzle pressure ratios of 7.0 and 12.0, respectively, the pressure distribution characteristics for these supersonic Mach numbers show similar tendencies to the supersonic pressure distributions discussed above. For the Mach number 1.9 pressure distributions, both figures show an initial compression of the exhaust flow downstream of the throat. The exhaust flow again reexpands to a slightly lower pressure, but not to the ambient pressure. The pressure distribution for the Mach number 3.0 condition (Figure 4-10) shows the same compression downstream of the throat, the slight reexpansion and the recompression. The NPR 12.0 flow shows a higher rate of compression than the NPR 7.0 for both case.

Generally, as the NPR increases, the exhaust flow downstream of the throat has the tendency to compress at a higher rate, that is, to form the thicker separation bubble due to the sharp corner at the throat for a given Mach number conditions. Especially the exhaust flow reaches to above ambient pressure for the NPR=12.0. In addition, the flow is affected by the secondary separation bubble causing the flow to recompress. Finally

the nozzle exhaust flow for the supersonic Mach numbers appears to be uniform. Thereafter, the flow does not continue to expand to lower pressure.

Pressure and Mach number contour plots for Mach numbers 1.9 and 3.0, are presented in Appendices C and D, for the baseline cowl at the assumed NPR schedule. In addition to the nozzle exhaust flow re-expansion and recompression region, the plume shock (external exhaust shock), the plume flow boundary, and the shocks in the jet plume flow can be seen.

4.4 Nozzle Cowl Effects

The nozzle cowl configuration effects for the supersonic case are presented in Figures 4-12 and 4-13 for the assumed NPR (7.0 and 16.0) and the Mach numbers (1.9 and 3.0). For supersonic Mach numbers, the pressure distributions show the characteristics of the pressure rise up to above the ambient pressure downstream of the nozzle throat due to the separation bubble for the given NPR.

For the Mach 1.9 condition and NPR 7.0 (Figure 4-12), the exhaust flow expansion (lowest to highest pressure obtained) downstream of the nozzle throat for the cowl configuration are baseline, -5 degree, long, and +5 degree cowl. These results are dependent on the internal expansion area ratios (the nozzle cowl exit divided by the nozzle throat area). The initial compression (lowest to highest pressure) exhibits the same pattern as the initial expansion. The flow then expands and recompresses. The flow reexpands approximately at the $x=3.5$ for the +5 degree cowl, $x=3.6$ for the long cowl, and $x=3.7$ for the -5 degree cowl and baseline cowl, respectively. The flow recompresses

approximately at the $x=5.8$ for the baseline cowl, $x=6.2$ for the long cowl, +5 degree cowl, and -5 degree cowl, respectively. The interaction between the boundary layer on the top surface and the plume shock forms the other separation bubble on the nozzle surface. The recompression properties depended on the cowl configuration (nearly in the reverse order of the initial compression) which decided the location of the separation bubble. The influence of plume shock for the baseline cowl on the nozzle surface, i.e., the location ($x=5.8$) of the separation bubble, preceded the other cases ($x=6.2$). Therefore, the baseline cowl recompresses prior to the cowl, the +5 degree cowl, and the -5 degree cowl on the nozzle/surface

Also, for the Mach 3.0 and NPR 15.0 condition (Figure 4-13), the exhaust flow expansion (lowest to highest pressure) downstream of the throat for the cowl configuration are baseline, long, and +5 degree cowl. The initial compression (lowest to highest pressure) shows the same sequence as the initial expansion. After compression, the flow reexpansion properties are similar and result in nearly the same (negative) C_p . For Mach number 3.0, the cowl shock has smaller deflection angle than Mach number 1.9 so that the interaction of the cowl shock with boundary layer on the nozzle surface is moved downstream of the nozzle surface. Also thickness of the separation bubble is thinner than the Mach number 1.9 and NPR 7.0. As a result, the flow appears to separate without recompression.

4.5 NPR Effects

NPR effects for Mach numbers 1.9 and 3.0, for the baseline cowl configuration

are presented in Figures 4-14 and 4-15. Clearly, the supersonic Mach number characteristics of the higher pressure of the initial compression for the increasing nozzle pressure ratios are presented in Figures 4-11 and 4-12, respectively.

NPR effects for Mach number 1.9 (Figure 4-14) have the properties of expansion, compression, reexpansion, and recompression for all cases. The apex of the separation bubble is correspondingly located at $x=3.7$ approximately except the NPR=0.9, i.e., flow off. And, the thickness of the separation bubble depends on the NPR. For NPRs 7.0 and 12.0, the exhaust flow expands to the ambient pressure. As NPR increase, the location of recompression moves downstream of the nozzle surface from $x=3.9$ (NPR=0.9) to $x=7.2$ (NPR=12.) due to the length of the separation bubble.

NPR effects for Mach number 3.0 (Figure 4-15) exhibit similar trends as the Mach number 1.9 near the initial separation bubble. But, as mentioned for the nozzle/cowl effects, the cowl shock for Mach number 3.0 has smaller angle than Mach number 1.9 so that the interaction of the cowl shock with the boundary layer on the nozzle surface is moved downstream of the nozzle surface. Therefore, the exhaust results in nearly the same (negative) C_p and appears to separate without recompression.

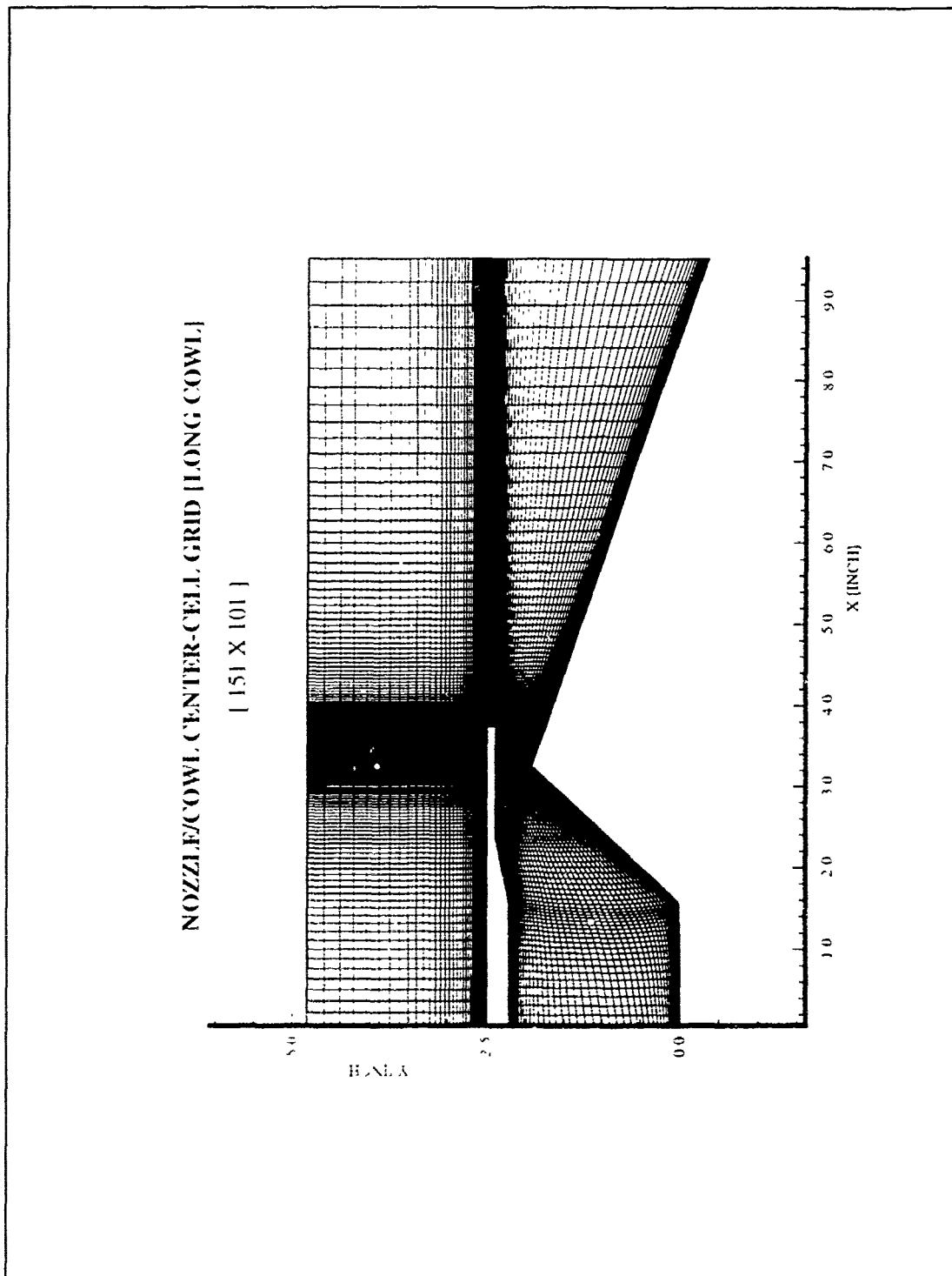


Figure 4-1 Long Cowl Center-Cell Grid (151×101)

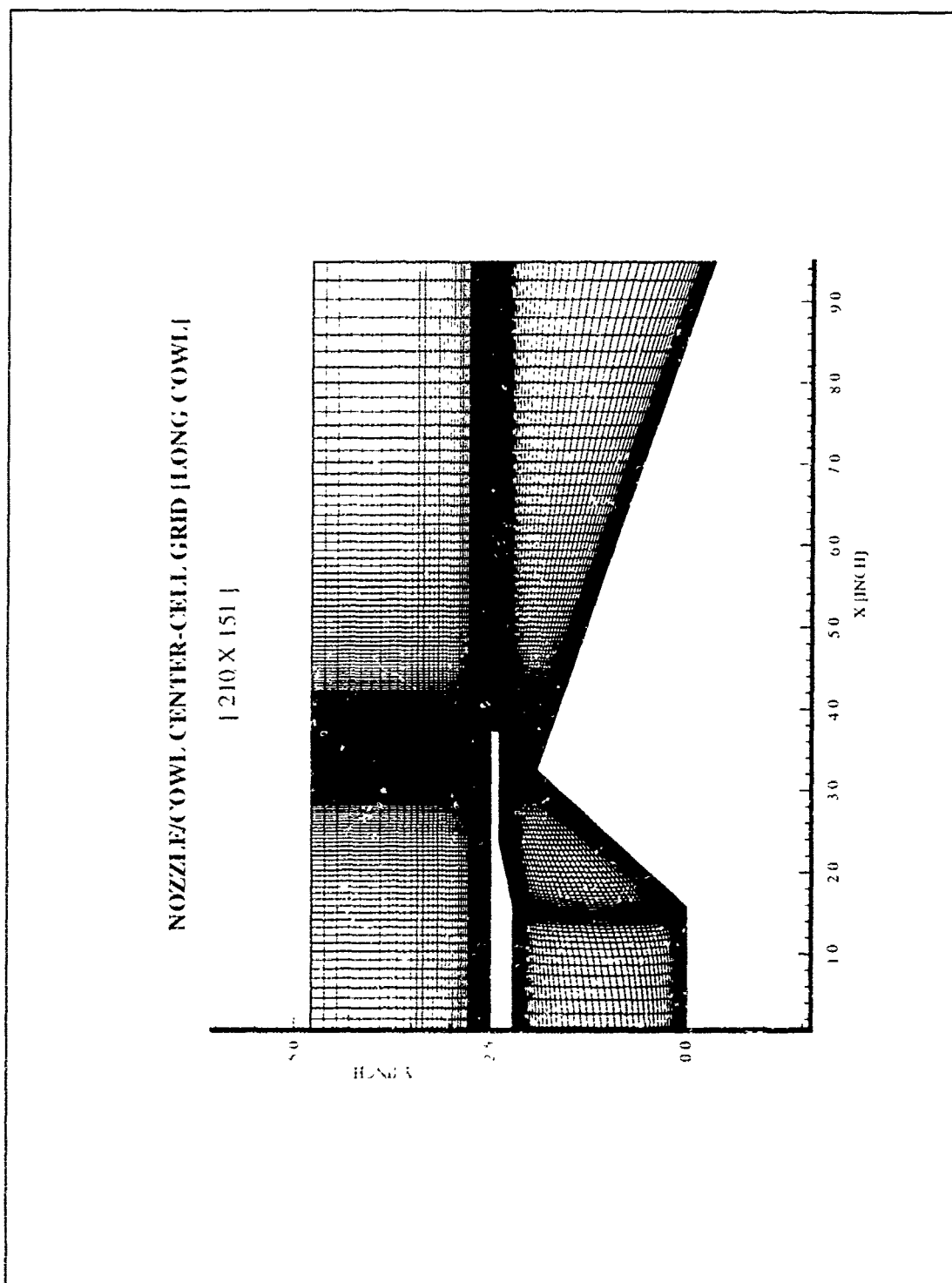


Figure 4-2 Long Cowl Center-Cell Grid (201x151)

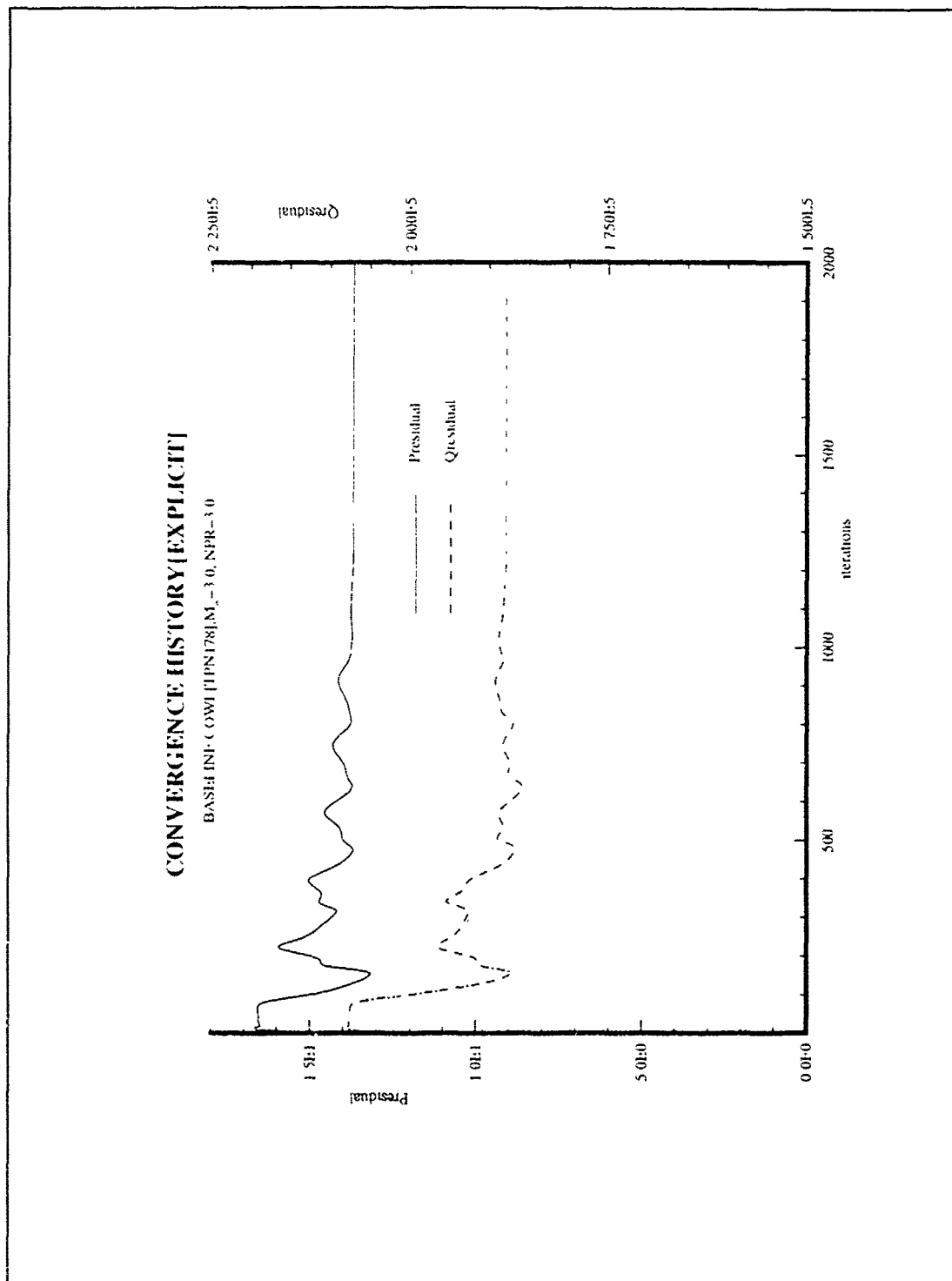


Figure 4-3 Convergence History (Explicit)

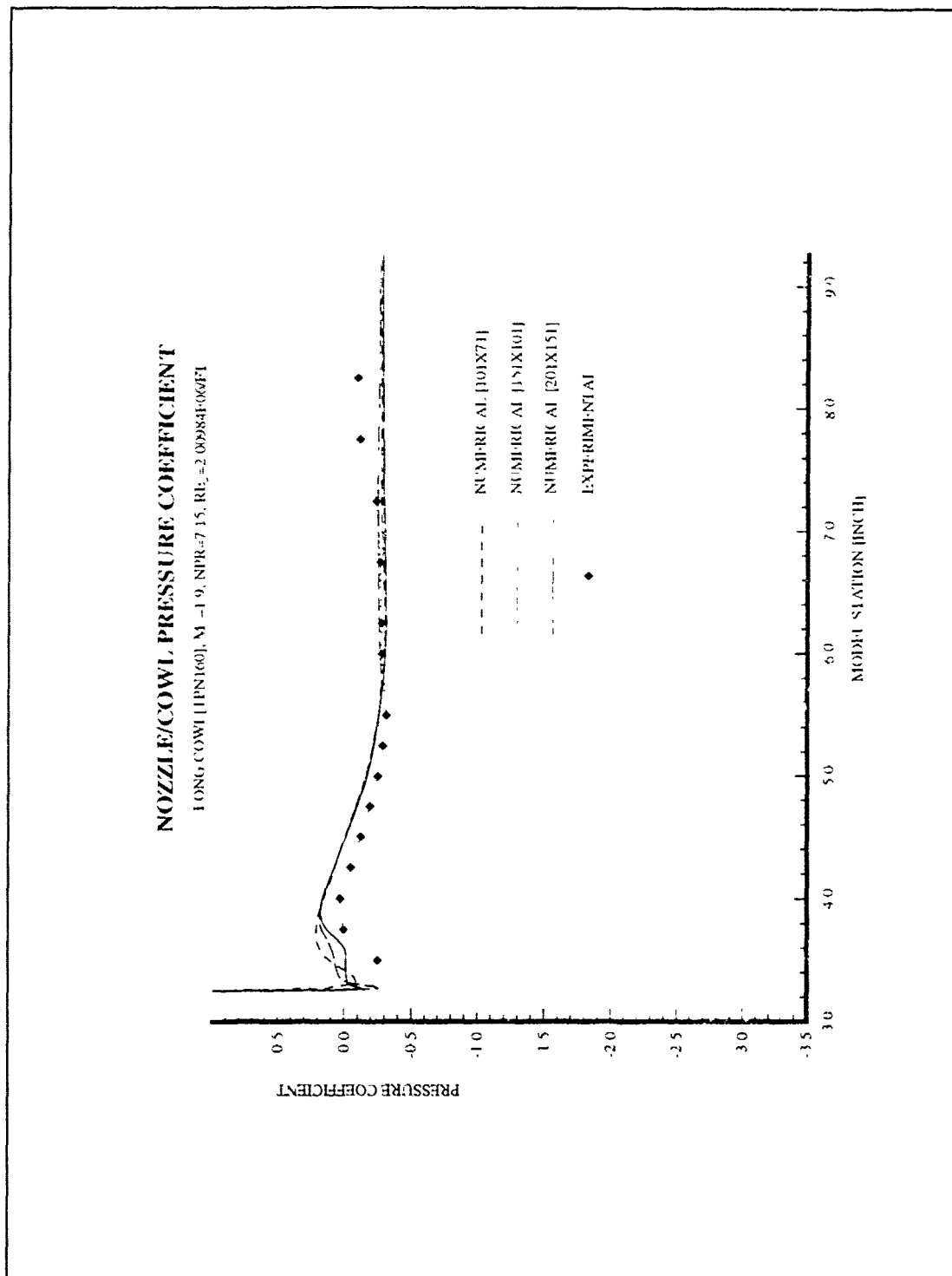


Figure 4-4 Grid Resolution Effects: Long Cowl, $M_\infty=1.9$, NPR=7.0

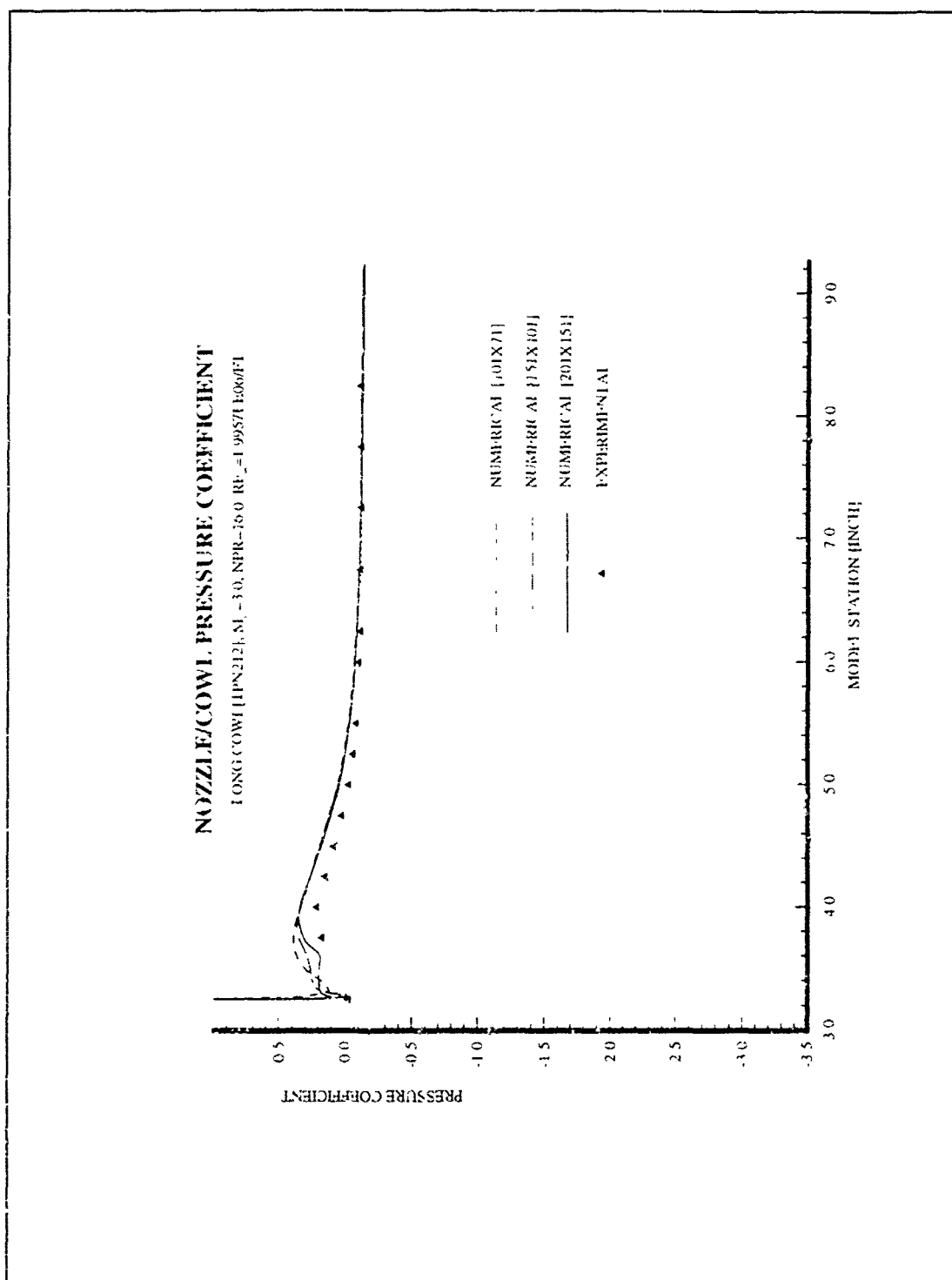


Figure 4-5 Grid Resolution Effects: Long Cowl, $M_\infty=3.0$, NPR=16.0

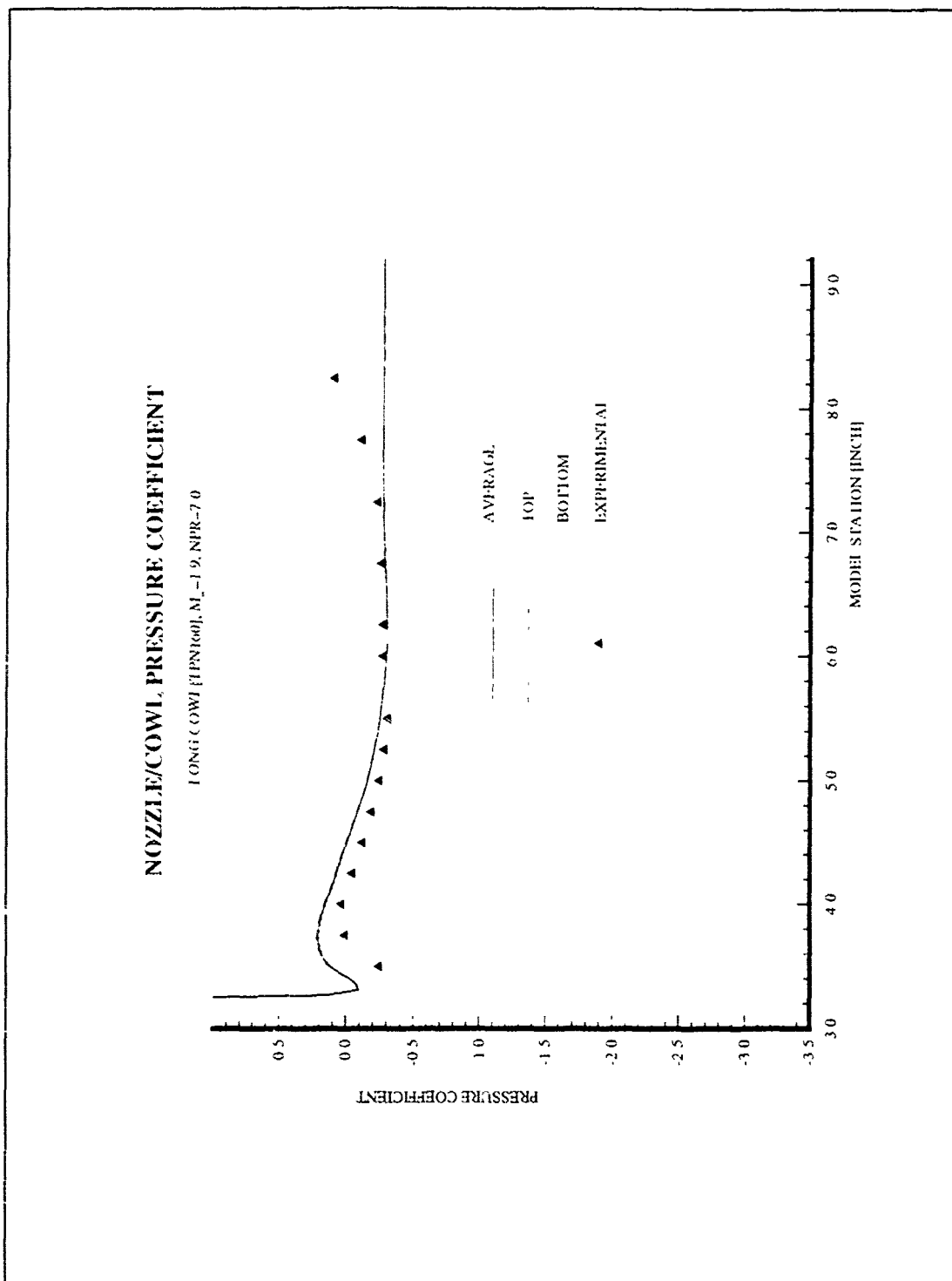


Figure 4-6 Influence of Initial Conditions: Long Cowl, $M_\infty=1.9$, NPR=7.0

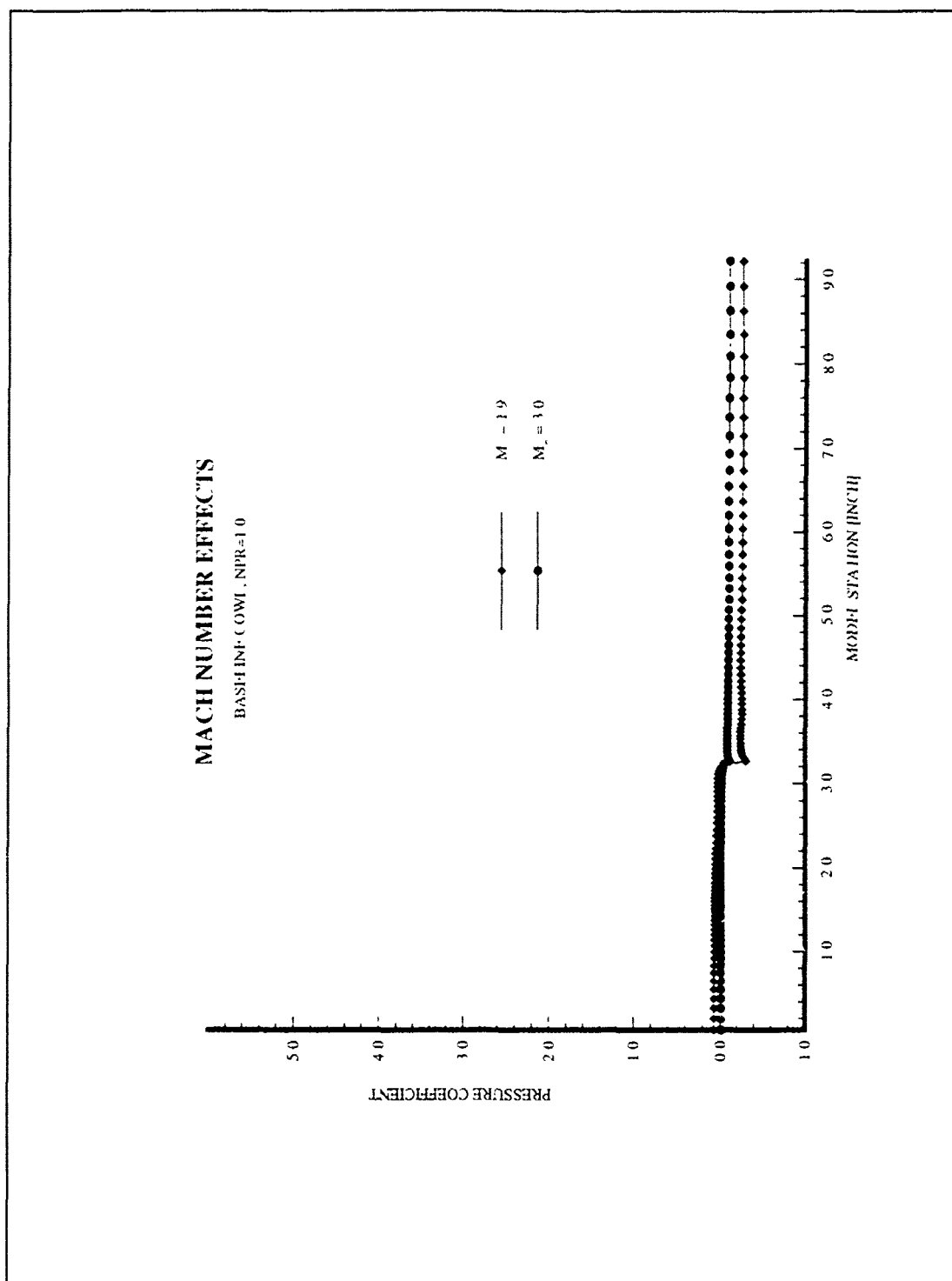


Figure 4-7 Mach Number Effects: Baseline Cowl, NPR=1.0

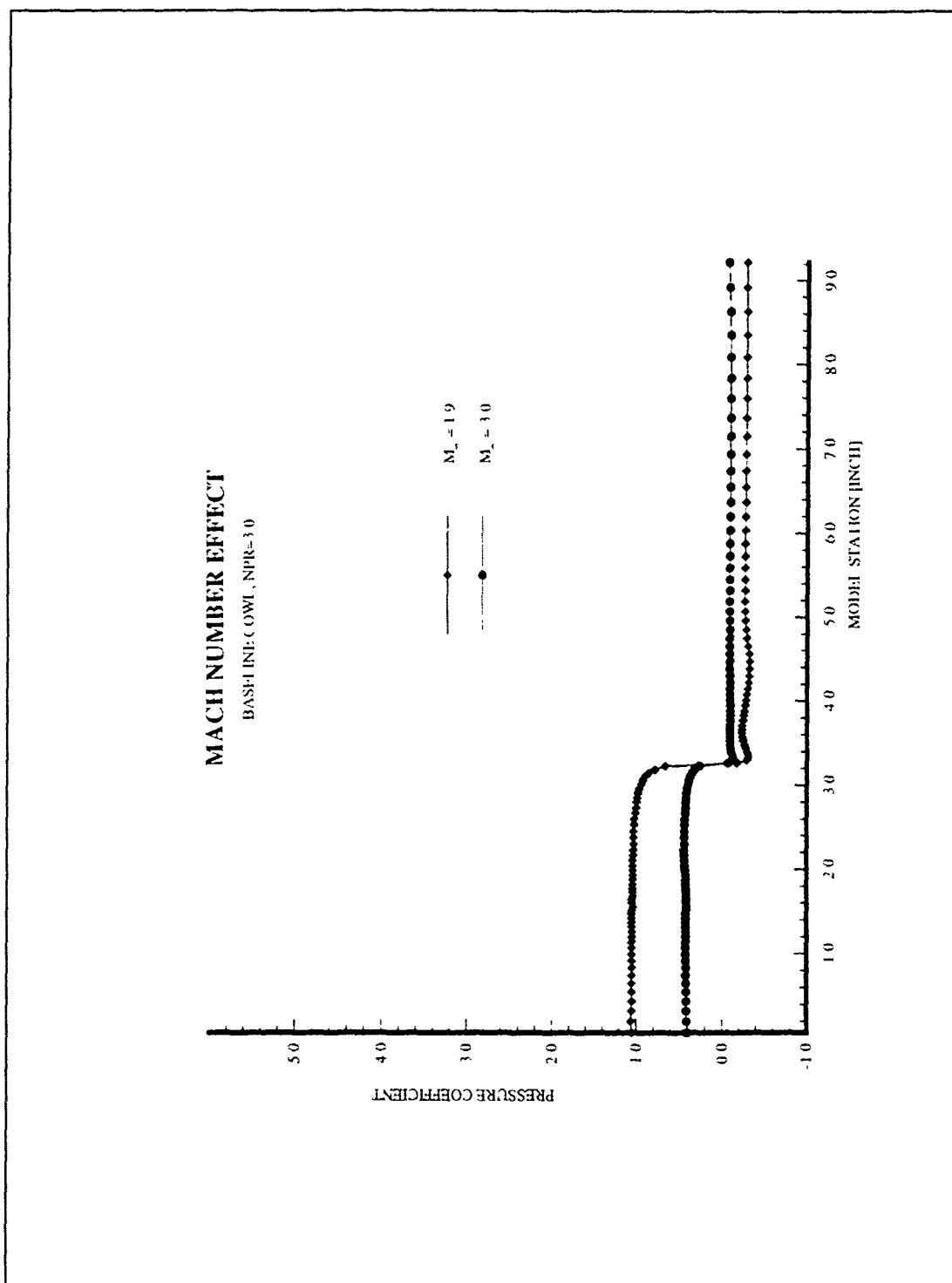


Figure 4-8 Mach Number Effects: Baseline Cowl, NPR=3.0

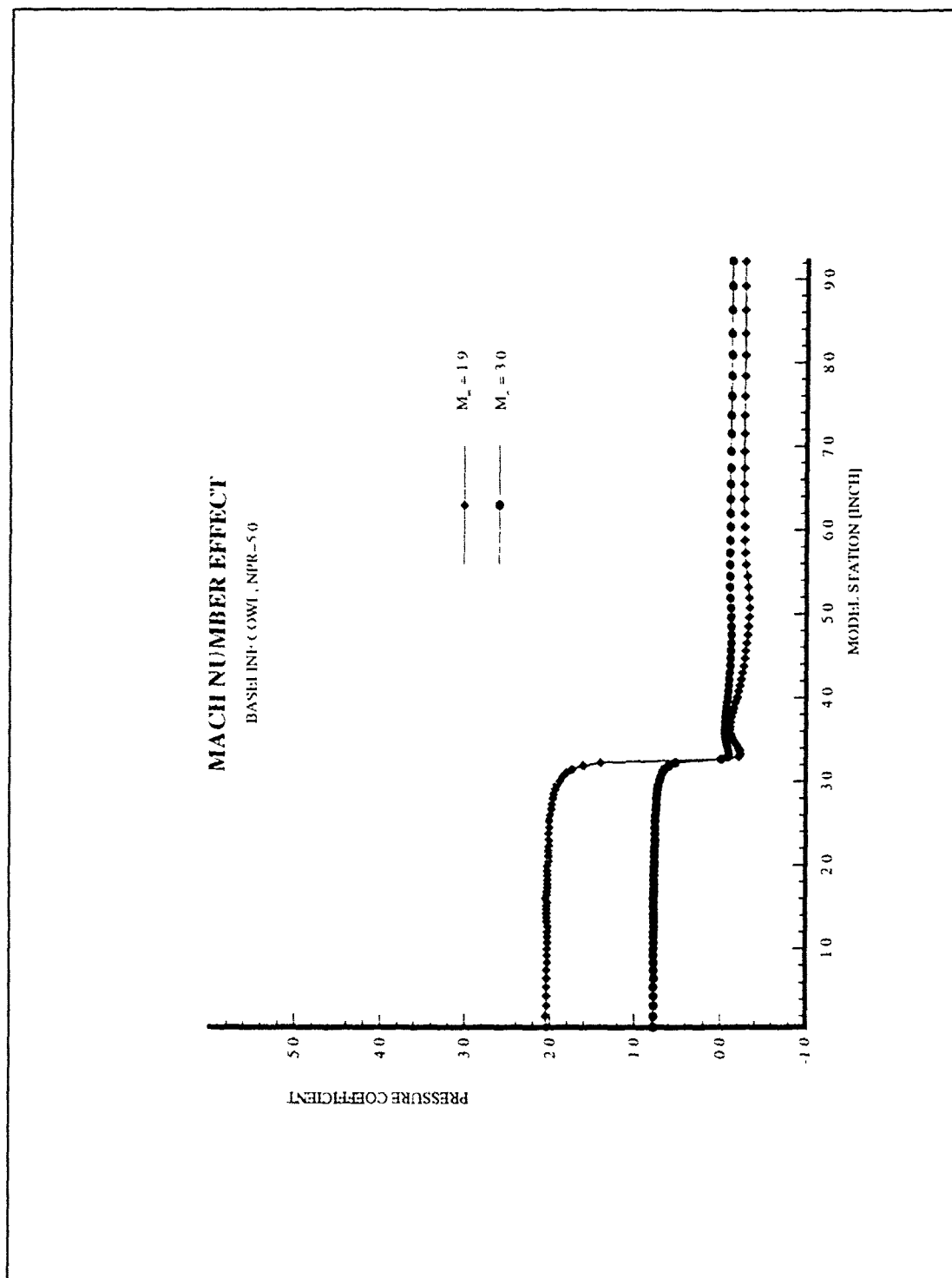


Figure 4-9 Mach Number Effects: Baseline Cowl, NPR=5.0

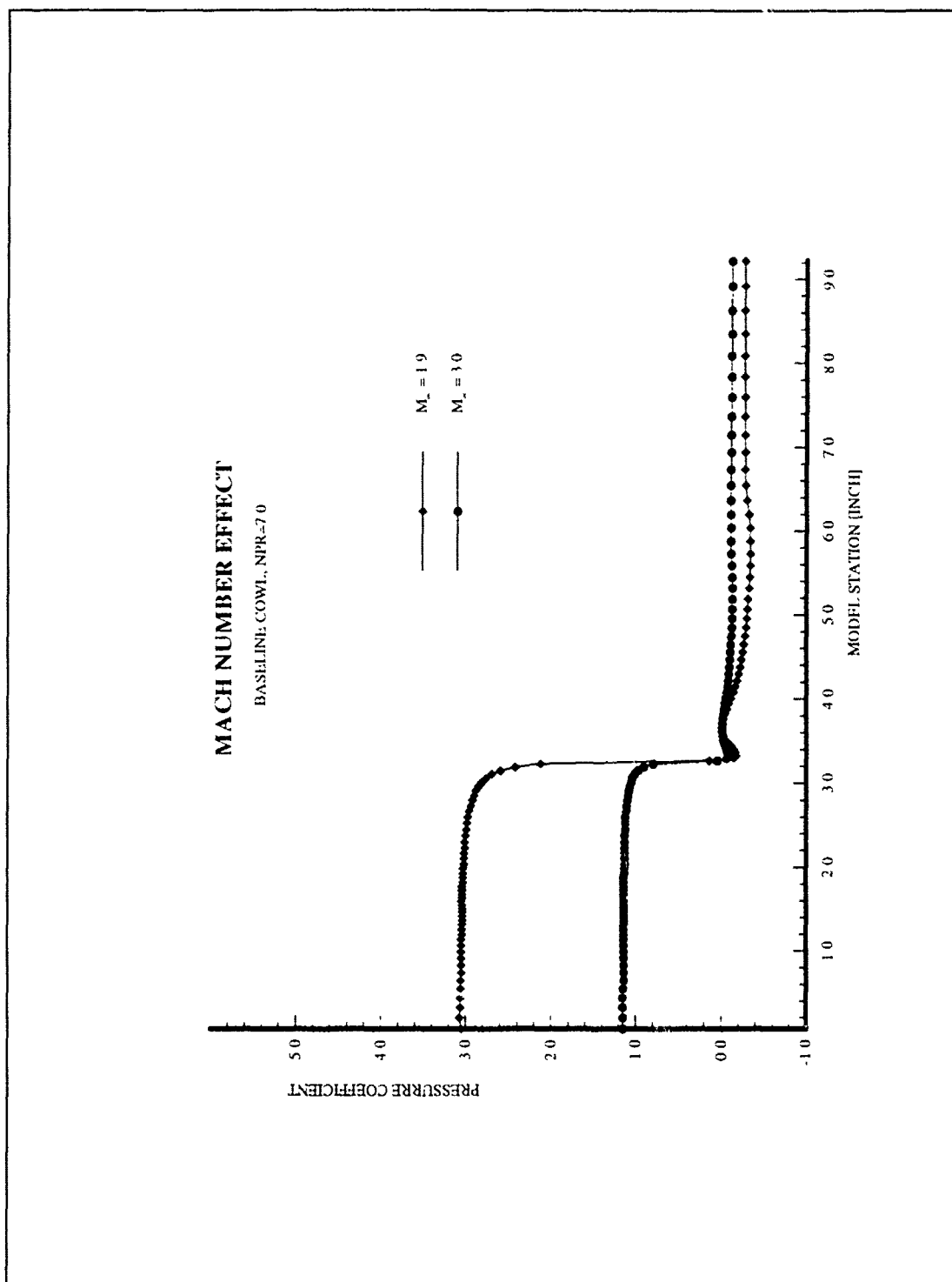


Figure 4-10 Mach Number Effects: Baseline Cowl, NPR=7.0

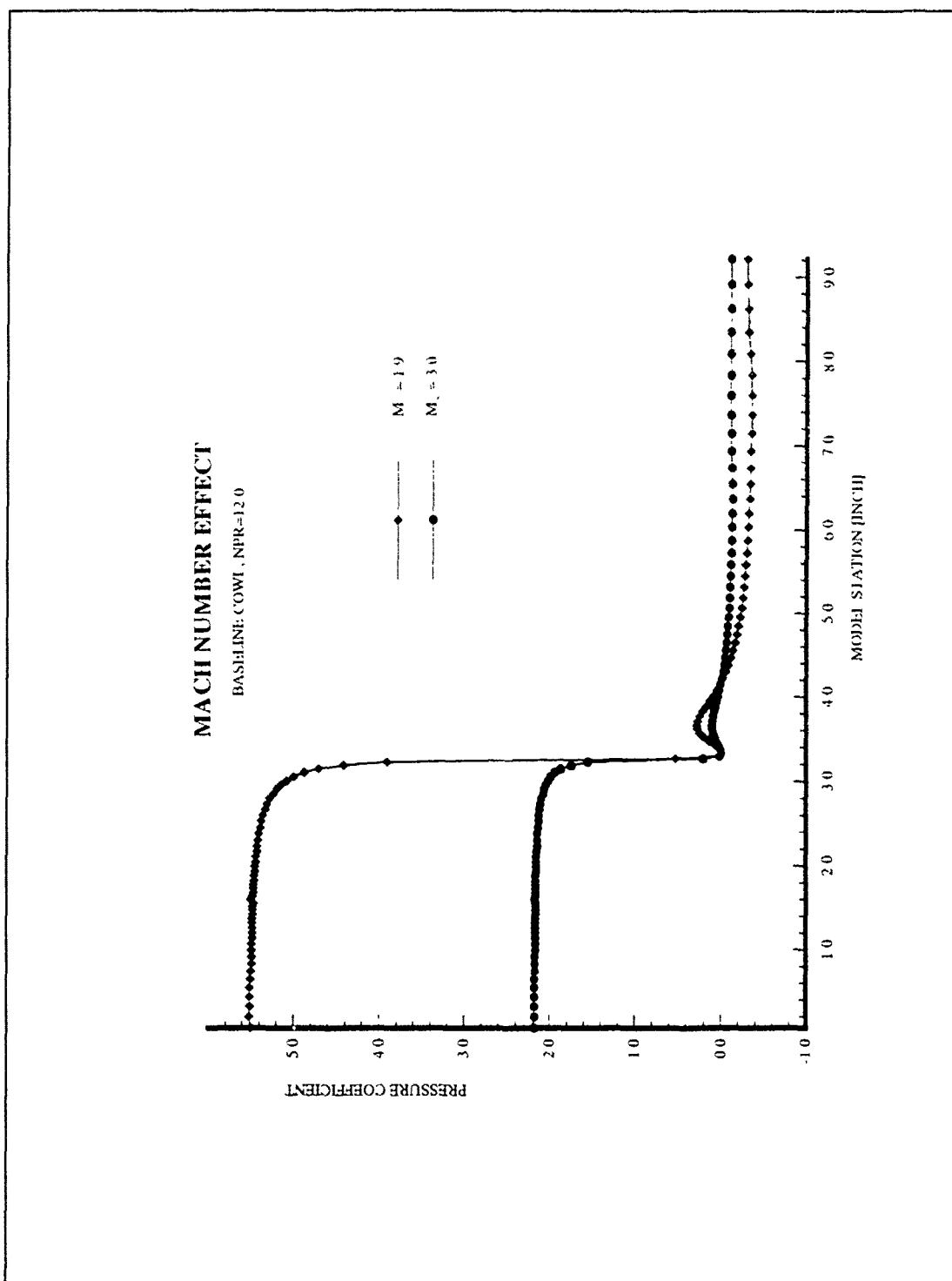


Figure 4-11 Mach Number Effects: Baseline Cowl, NPR=12.0

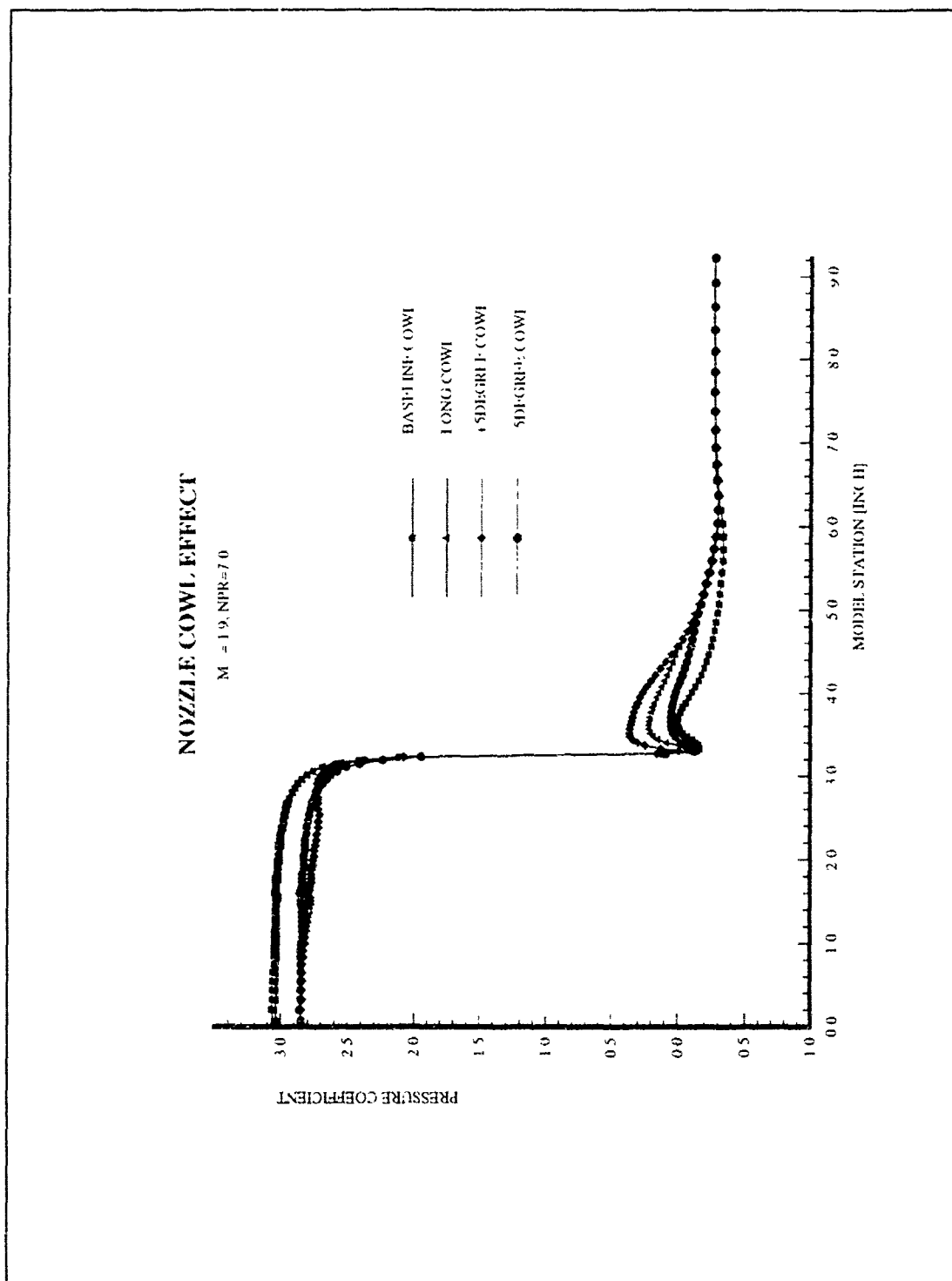


Figure 4-12 Nozzle Cowl Effects: Baseline Cowl, $M_{\infty}=1.9$, $NPR=7.0$

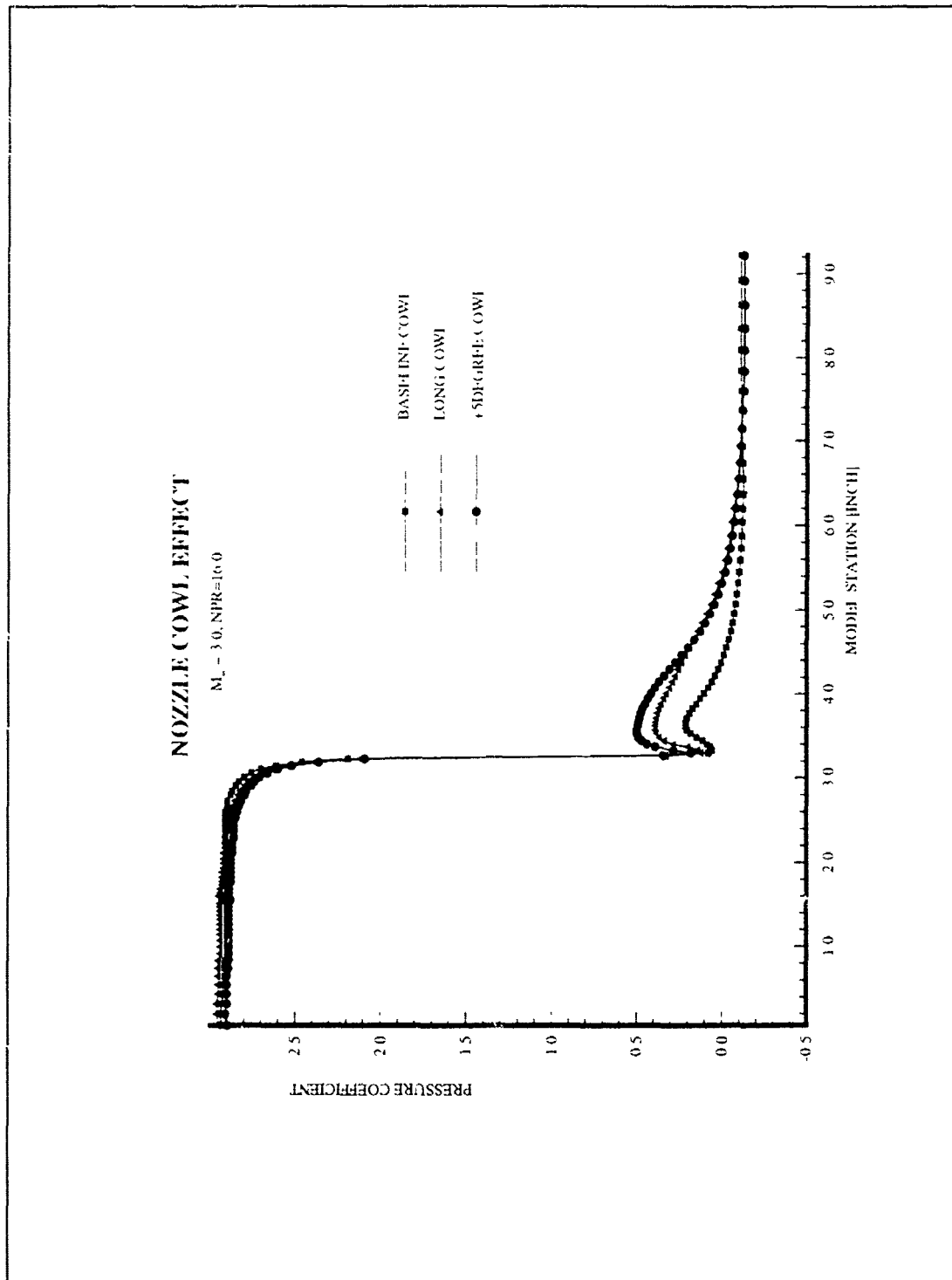


Figure 4-13 Nozzle Cowl Effects: Baseline Cowl, $M_n=3.0$, $NPR=16.0$

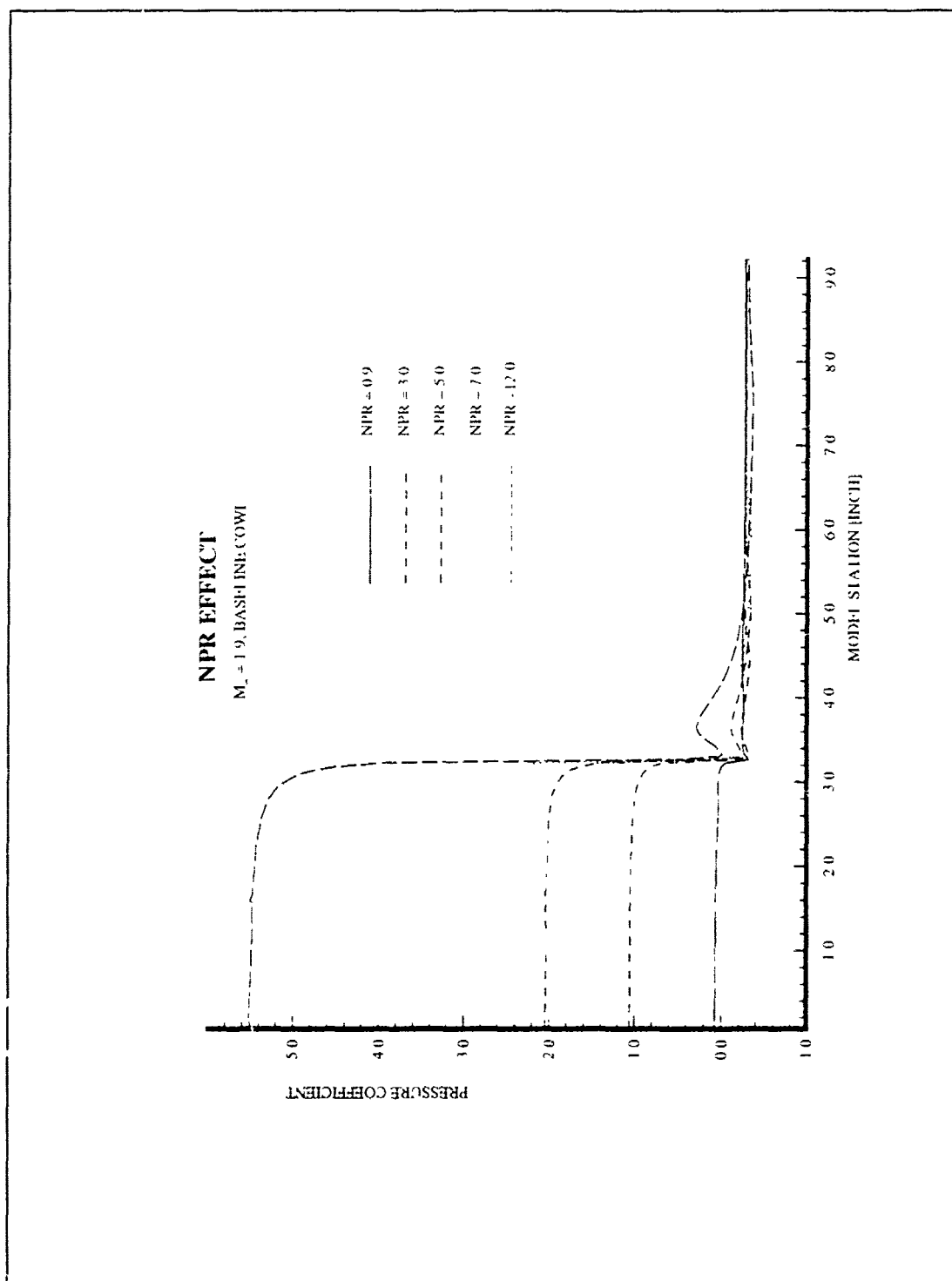


Figure 4-14 NPR Effects: Baseline Cowl, $M_\infty=1.9$

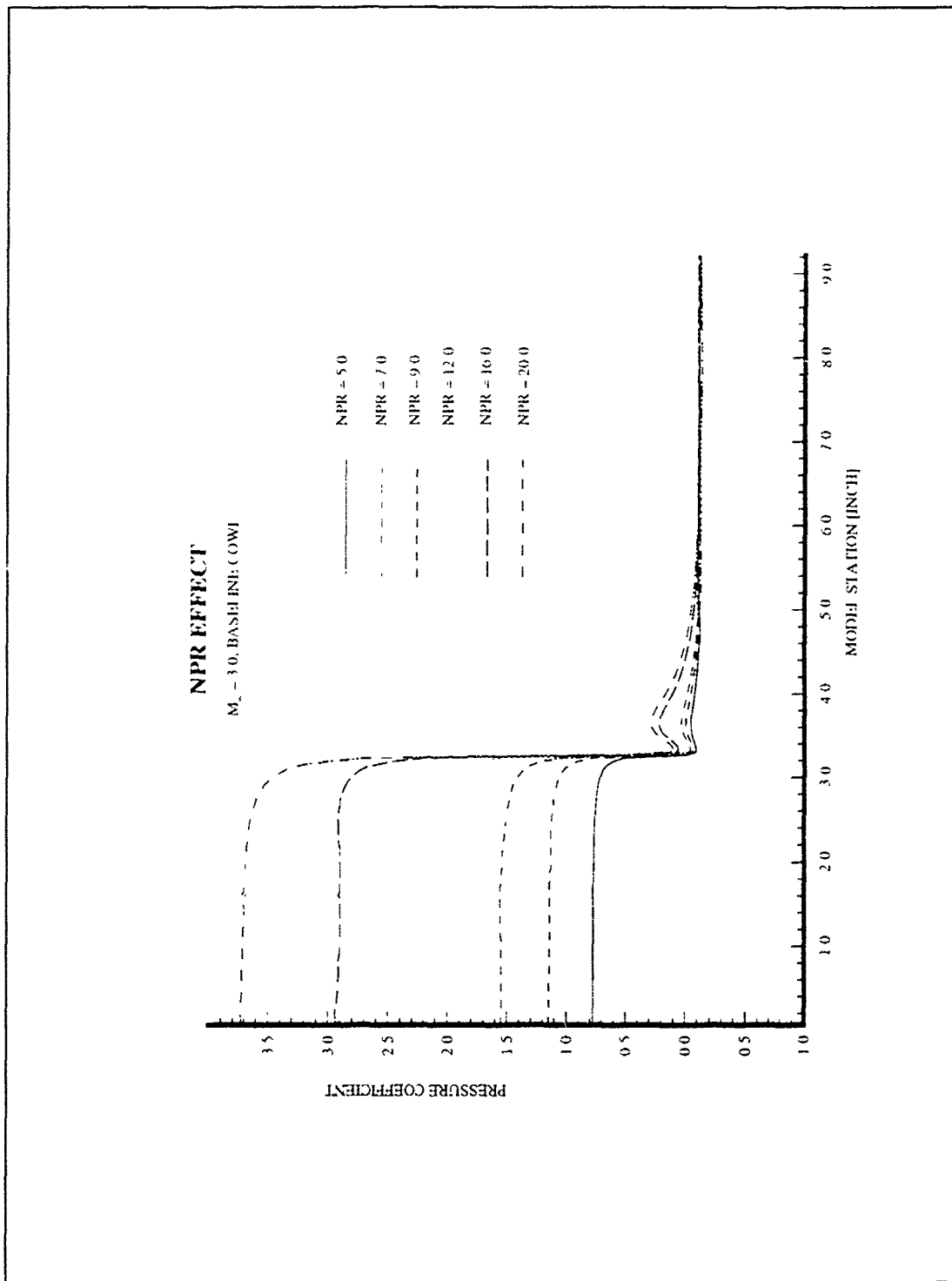


Figure 4-15 NPR Effects: Baseline Cowl, $M_\infty=3.0$

V. EXPERIMENTAL AND NUMERICAL ANALYSIS

For the nozzle/afterbody configuration tested through experimental and numerical analysis, two separation bubbles were detected. These were the key phenomena to be analyzed. One is located just downstream of the throat and is due to a sharp corner of the nozzle throat, while the other is located on the top surface, where an interaction of the cowl shock with the boundary layer of the top surface exists. Figure 5-1 is a diagram of the overexpanded nozzle exhaust flow at supersonic Mach numbers. According to the experimental tests (4), the oblique shock for Mach number 1.9 and 3.0, varies from 45 degrees to 35 degrees, respectively. For Mach number 3.0, the cowl shock has a smaller deflection angle than Mach number 1.9 so that the interaction of the cowl shock with boundary layer on the nozzle surface is moved downstream of the nozzle surface. On the assumption of the computational model, the exhaust flow for Mach number 1.9 showed the recompression phenomena at the second separation bubble. But the flow for Mach number 3.0 appeared to be nearly the same (negative) C_p and separate without recompression. This angle changes considerably with cowl configuration and NPR.

Unfortunately, there were poor agreement between the experimental data and the numerical results for the subsonic cases. These results were caused by the discrepancy between the models. In experimental implementations, Cochran obtained the nozzle surface centerline properties for the performance of the nozzle/afterbody on the assumption of the two-dimensional model, although he did the three-dimensional model. In other words, his results included the three-dimensional effects, which made worse the consistency for the subsonic cases due to interaction between the exhaust nozzle plume

and the external flow. And for the supersonic cases, especially Mach number 1.9, due to discrepancy on the assumption of models, the three-dimensional effects can't be neglected near the second separation bubble.

This angle changes considerably with cowl configuration and NPR.

5.1 Mach Number Effects

5.1.1 Supersonic Effects

The pressure coefficient, C_p , comparison between the experimental and numerical method were presented in the Figures 5-2 to 5-11 at specific NPR for the baseline cowl configuration. Generally, these figures show a favorable agreement between theory and experiment, as Mach numbers increased.

For the NPR 1.0, Figures 5-2 and 5-3 show that computational versus experimental results are a little more consistent for Mach number 3.0 than for Mach number 1.9. Namely, for the Mach number 1.9 (Figure 5-2) according to the numerical result, the pressure distributions appear nearly flat after compression, but the flow recovers (recompresses to near ambient conditions) at the last pressure tap location in the experimental results. The differences between the experiment and numerical results are a result of the size of the second separation bubble. For Mach number 3.0, the numerical results show the identical trends as above, but the experimental results have the characteristics of slight compression and reexpansion around the second separation bubble ($x=6.0$). The oblique shock angle changes considerably with Mach number so that Mach

number 1.9 has a larger reflection angle than Mach number 3.0. This reflection angle determine the location of the second separation area. Comparing Figures 5-2 and 5-3, the location of the recompression for Mach number 1.9 is ahead of that of Mach number 3.0 ($x=4.2$ for Mach 1.9 and $x=6.0$ for Mach 3.0).

For the NPRs 3.0 and 5.0, Figure 5-4 to 5-7 show similar trends as the NPR 1.0. Figure 5-4 for Mach number 1.9 (NPR 3.0), on the assumption of the laminar flow, shows some compression characteristics which were not apparent in the experimental results near the first separation bubble. But, the experimental results show a higher rate of compression around the second separation bubble which is built up, contrary to expectation, by the external flow (three-dimensional effects) as well as the interaction of nozzle surface boundary layer and cowl shock wave. For the NPR 5.0, the difference in values of the pressure coefficients near the second separation bubble as well as near the first bubble were larger than the NPR 3.0 cases. Particularly, at x values beyond the recompression, the difference between experiment and the computational solutions grow larger. The Mach number 3.0 results show a better agreement than those at Mach 1.9. Especially, the trend of reexpansion and recompression after the apex of the second separation bubble was examined at the NPR 5.0 (Figure 5-7) for the experimental results, because the external flow influenced the second separation bubble, so that the compressed up to $x=5.9$ and reexpanded slightly after the apex of the second separation bubble. This was not detected in the computational implementations which was assumed on the two-dimensional model.

For the NPR 7.0 and 12.0, Figures 5-8 to 5-11 show that the trends proceed

favorably as the Mach number increased, although the numerical investigation was based on the laminar flow assumption. In the experimental performance, the internal flow initially dominated the external flow downstream of the nozzle throat for the same NPR conditions, as Mach number increased. Therefore, there was better agreement for Mach number 3.0 (Figures 5-9 and 5-11) than for Mach number 1.9 (Figures 5-8 and 5-10) at the second separation bubble as well as the initial separation bubble. Additionally, these results mean that the difference between the turbulence and the laminar flow make worse the results between experiment and theory at the initial separation bubble as the Mach number decreases. Also, the difference between the two-dimensional model and the three-dimensional model increases near the second separation bubble, since the internal flow is effected by the external flow so that the exhaust flow - the results were extracted along the centerline of the nozzle surface at the experimental performance - continuously compressed at this region. Also, as the NPR increased, the agreement between theory and experiment proceed unfavorable locally for the same Mach number conditions at the apex of the initial separation bubble, since the flow with the higher NPR formed the larger separation bubble at this region.

To investigate the difference between the experiment and the numerical solutions in detail, the three-dimensional effects were considered for specific cases. Figures 5-12 and 5-13 show the comparison between the experimental results and the numerical results. The experimental results were extracted from the centerline and off-centerline (positive 1 inch and negative 1 inch laterally) tap location on the nozzle surface. For Mach number 1.9 and NPR 3.0, Figure 5-12, the internal flow initially dominates the external flow

downstream of the nozzle throat so that off-centerline pressure above the centerline one. But after approximately $x=4.8$, the centerline flow maintained the higher pressure than the off-center line and compressed by the influence of the external flow, But, the off-centerline flow slightly compressed and expanded after $x=4.7$, and the flow continuously compressed again due to the adverse flow on the nozzle surface at $x=6.2$. Mach number 3.0 and NPR 3.0 case, Figure 5-13, shows that there are smaller variations between the experiment and the numerical solutions, because the internal flow dominates the external flow as Mach number increases. As a result, as Mach number increased, the conversion point where the signal of the difference value between the centerline and the off-centerline is changed moves afterward (from $x=4.7$ to $x=5.5$), which explains why the internal flow dominates the external flow and there is a thin boundary layer on the nozzle surface.

5.1.2 Subsonic Effects

The subsonic cases showed poor agreement between the experiment and the computational solutions, because there is severe interaction between the nozzle exhaust plume and the external flow. To investigate the difference between the experiment and the computational results, the three-dimensional effects were considered for specific case like the supersonic ones. For Mach number 0.6 and NPR 3.0, Figure 5-14 shows the comparison between the experiment and the computational results. Clearly, the experimental results showed the complicated flow phenomena on the nozzle surface comparing to the results for the supersonic cases which showed the symmetric properties for the off-centerline values. Just downstream of the nozzle throat, the internal flow is

influenced by the external so that centerline pressure is higher than the off-centerline pressure. And then the centerline pressure is lower than the off-centerline one, which means that initially the flow turns towards the centerline and then turn outward after the impingement at the centerline. The centerline flow promptly recovered the higher pressure than the off-centerline and maintained nearly above the ambient pressure uniformly, after all. There is a large difference between the results at the initial separation bubble, which means that the assumption of turbulent versus laminar flow is more significant in the subsonic regime. To reinforce the subsonic problems, some supplementary methods were used, which are the assumption of the lower (external) fictitious boundary conditions. These methods still could not solve the subsonic problems.

5.2 Nozzle Cowl Effects

The pressure coefficient, C_p , comparison between the experimental and numerical methods are presented in the Figures 5-15 to 5-21 at specific NPRs for the different cowl configuration.

The case for the long cowl at Mach number 1.9 and NPR 7.0, Figure 5-16, shows that the differences in pressure coefficient between theory and experiment around the apex of the compression are larger than the baseline cowl, Figure 5-15. This is because the expansion waves caused by the sharp throat impinge on the upper surface of the cowl and the resulting exhaust flow is much more complicated. Therefore, the numerical results show larger separation bubble than the experimental test. Since a turbulent boundary layer allows higher adverse flow gradient, there is smaller separation bubble on the downstream

side of the nozzle surface. Also, the identical results were obtained for the +5 degree cowl in the Figure 5-17. For the -5 degree cowl, Figure 5-18, the exhaust flow is expanded at the hinge point of the cowl upper surface, so that there will be smaller separation bubble than the long and +5 degree cowl. Therefore, the results for -5 degree cowl case show a better agreement than the long and +5 degree cowl.

The case for Mach number 3.0 and NPR 16.0 shows similar trends as above until the flow encounters compression, and it again shows good agreement after reexpansion. In contrast, for Mach number 1.9 and NPR 7.0 case, the numerical results appear flat after compression, while the experimental results show the recompression. As the Mach number increased, the internal flow dominated the external flow so that the internal flow was not influenced by the external flow and kept the uniform flow.

5.3 NPR Effects

The pressure coefficient, C_p , comparison between the experimental and numerical method were already presented in the Figures 5-3 to 5-15, Figures 5-19, 5-22, 5-23, and 5-24 for various NPR for the baseline cowl configuration. Generally, it showed a good agreement between the numerical solutions and experiment as Mach number and NPR increased.

For Mach number 1.9, the Figures 5-2, 5-4, 5-6, and 5-10 show that the trends are less consistent than for Mach 3.0, Figures 5-7, 5-9, 5-22, 5-11, 5-19, 5-23, and 5-24. However, there are some discrepancies between theory and experiment around the peak of the compression and the second separation bubble exist, because the boundary layer,

most likely turbulent in the experiment, allow a higher adverse flow gradient. In addition, it should be necessary to consider the other factors that effect the phenomenon, i.e., the disagreement at x values beyond the recompression. The detailed explanation to synthesize the whole results will be covered below. Figures 5-7, 5-9, 5-22, 5-11, 5-19, 5-23, and 5-24, for the Mach number 3.0, show that the agreement between numerical solutions and experiment proceed quite favorably, as the NPR increases, although the numerical investigation was performed on the basis of a laminar flow assumption.

In the experimental testing, Cochran designed the three-dimensional model and conducted the test. However, he assumed a two-dimensional hypersonic nozzle /afterbody for the performance parameters of the test, and reduced data according to the parametric cases. Even though he fully performed the three-dimensional model, he calculated the centerline of integrated external ramp pressure coefficient, C_p , on the assumption of two-dimensional model, since the higher density of pressure taps characterized the nozzle exhaust flow and the afterbody ramp pressure more accurately. Additionally, he obtained the off-centerline pressure to determine the lateral variation of the flow, which will be valuable data for the further research. Therefore, the three-dimensional effects were performed to validate the consistency between the experimental data and the numerical solutions. Generally, as Mach number increased, the difference between the experiment and the numerical results decreased favorably. For the subsonic case, there was severe interaction between the nozzle plume flow, the external flow, and the afterbody flow. This interaction made comparison of the CFD data and experimental data very difficult, so that

the comparison for just one case was conducted. But, for the supersonic cases, the results show good agreement near the initial separation bubble as Mach number increased, because the exhaust flow overexpansion dominates and is uninfluenced by other effects. Near the second separation bubble, however, the results are not as consistent, because the recompression characteristics are influenced by the interaction among the external flow all around, the afterbody plume, as well as the separation bubble.

For the Mach number effects, as Mach number increased, there is better agreement between the experimental and the numerical results at the initial separation bubble than at the second separation bubble, since the internal properties are initially uninfluenced by the external flow. Additionally, the assumption of the laminar flow slightly caused the differences between the data. Also, for Mach number 1.9 cases, the discrepancy between the two-dimensional computational model and the three-dimensional experimental model caused the difference. For the nozzle/cowl configuration, the -5 degree cowl showed the best agreement among the cowl configurations, because the downward cowl (5 degrees) produced a more dominant exhaust flow downstream of the nozzle throat and more effectively isolated the nozzle from its surroundings. As for the Mach number effects, the laminar flow assumption in the CFD model had its largest influence at low Mach numbers, with decreasing influence as Mach number increased. But for the NPR effects, the flow with higher NPR formed the thicker initial separation bubble.

If it is assumed that the research was performed on the same two-dimensional model, we may analyze and compare the results more accurately. As stated in reference (18), the laminar boundary layer on the top surface separates because of the interaction

of the cowl shock with the boundary layer on the top surface. But separation completely disappeared for the turbulent flow under the experimental test. The turbulent boundary layer is able to accept a higher adverse flow gradient without separating for the two-dimensional assumption model. Therefore, the numerical investigation for the three-dimensional model can solve the obscure problems encountered near the secondary separation bubble.

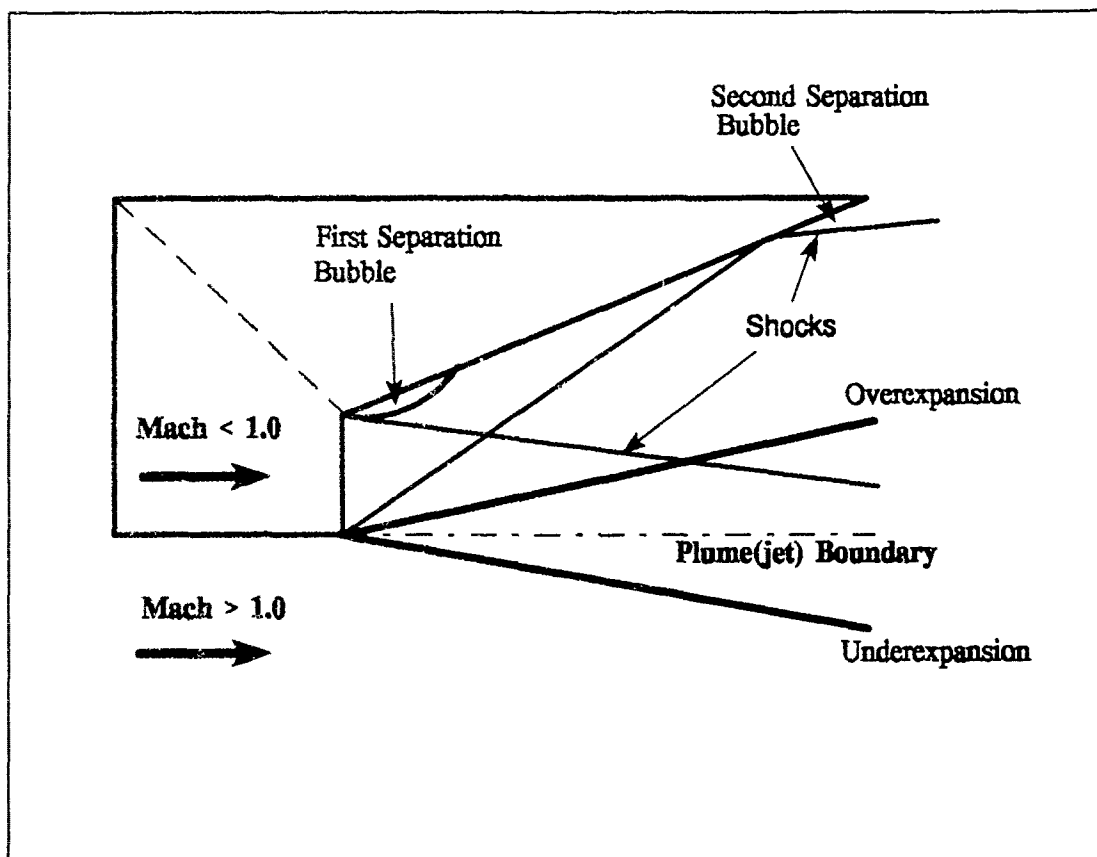


Figure 5-1 Schematic of Over and Underexpanded Exhaust at Supersonic Freestream Mach Number

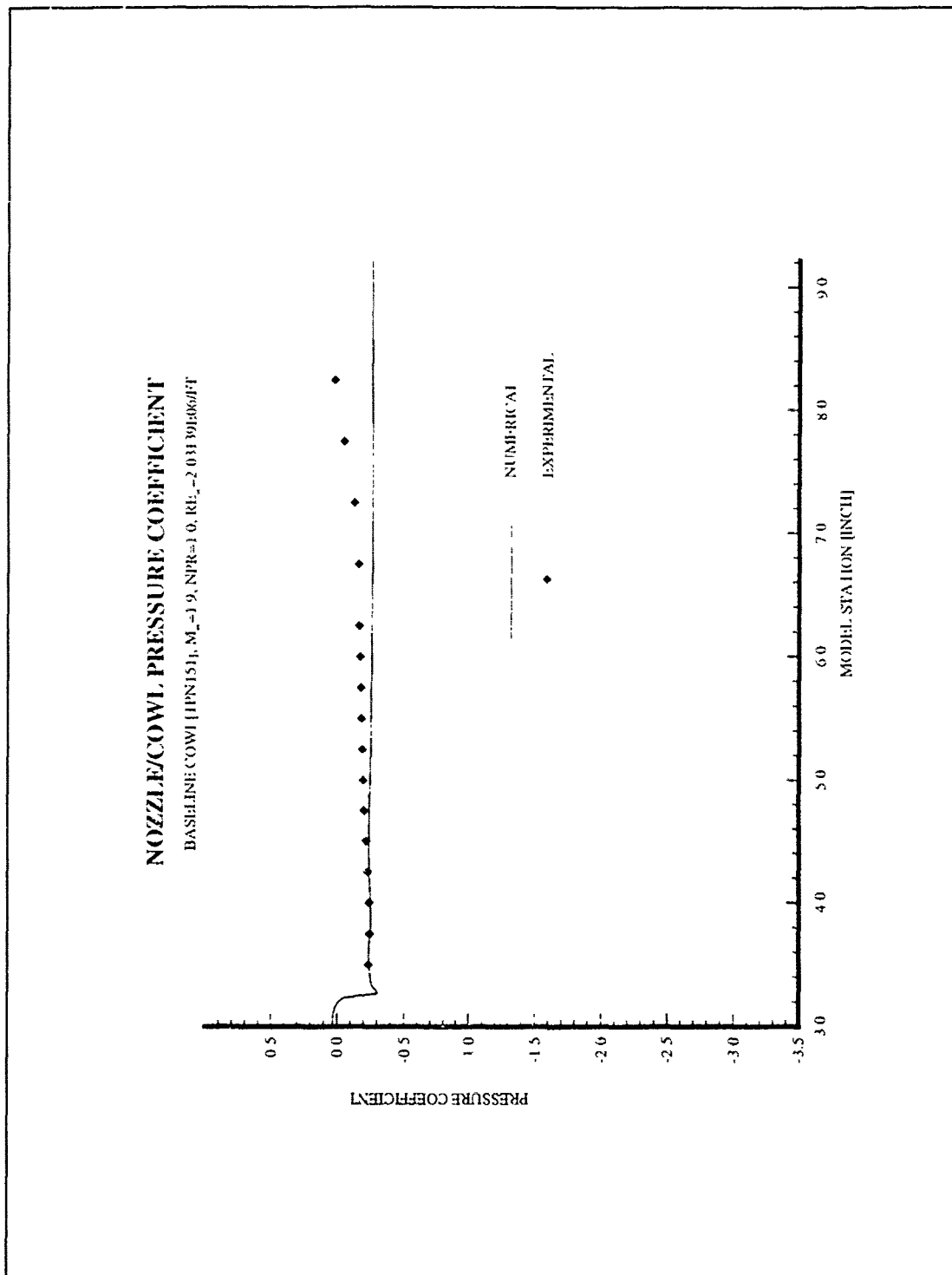


Figure 5-2 Comparison of an Experimental and Numerical Pressure Coefficients (Mach Effects): Baseline Cowl, $M_\infty=1.9$, NPR=1.0

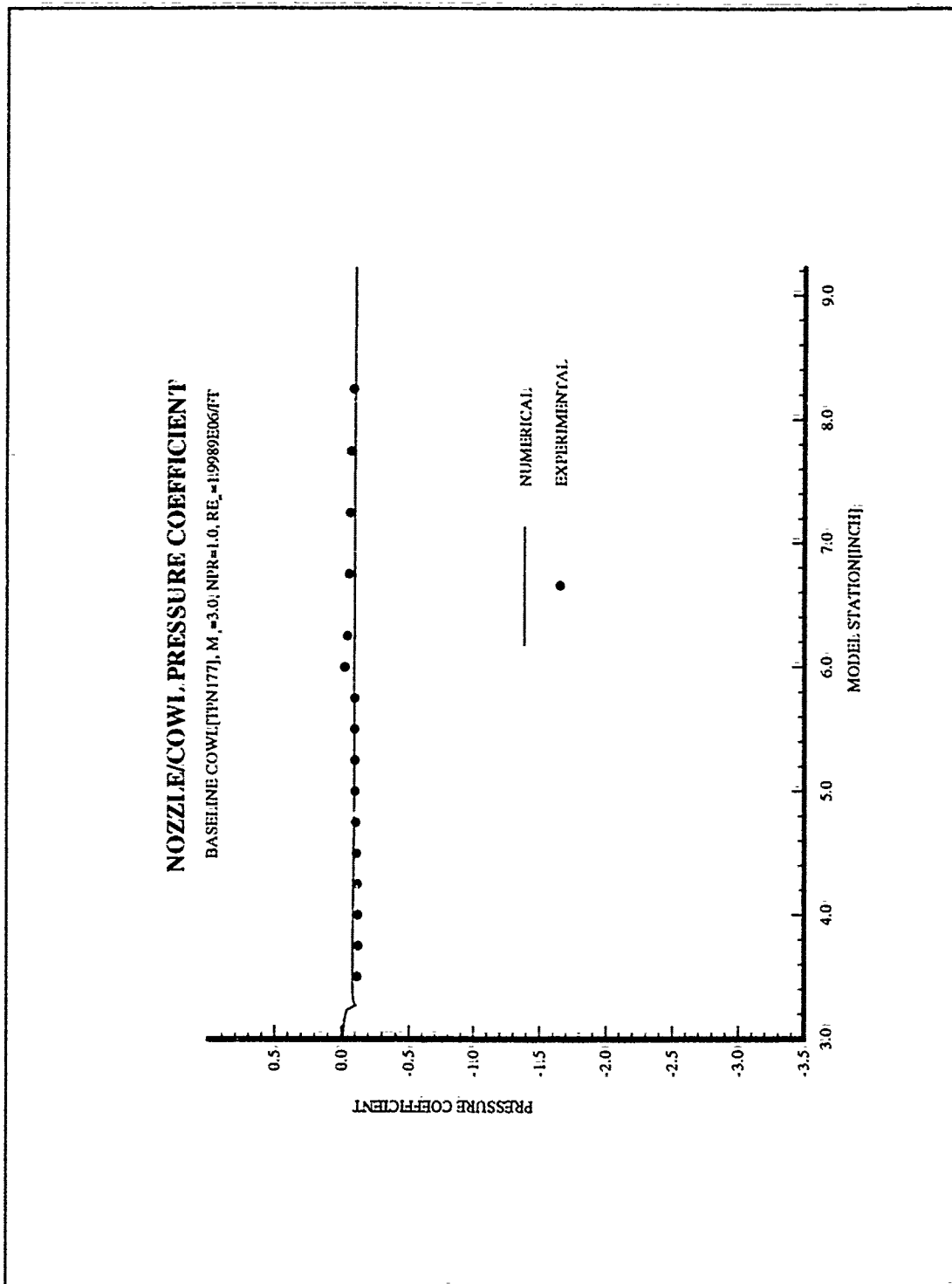


Figure 5-3 Comparison of an Experimental and Numerical Pressure Coefficients (Mach Effects): Baseline Cowl, $M_\infty=3.0$, NPR=1.0

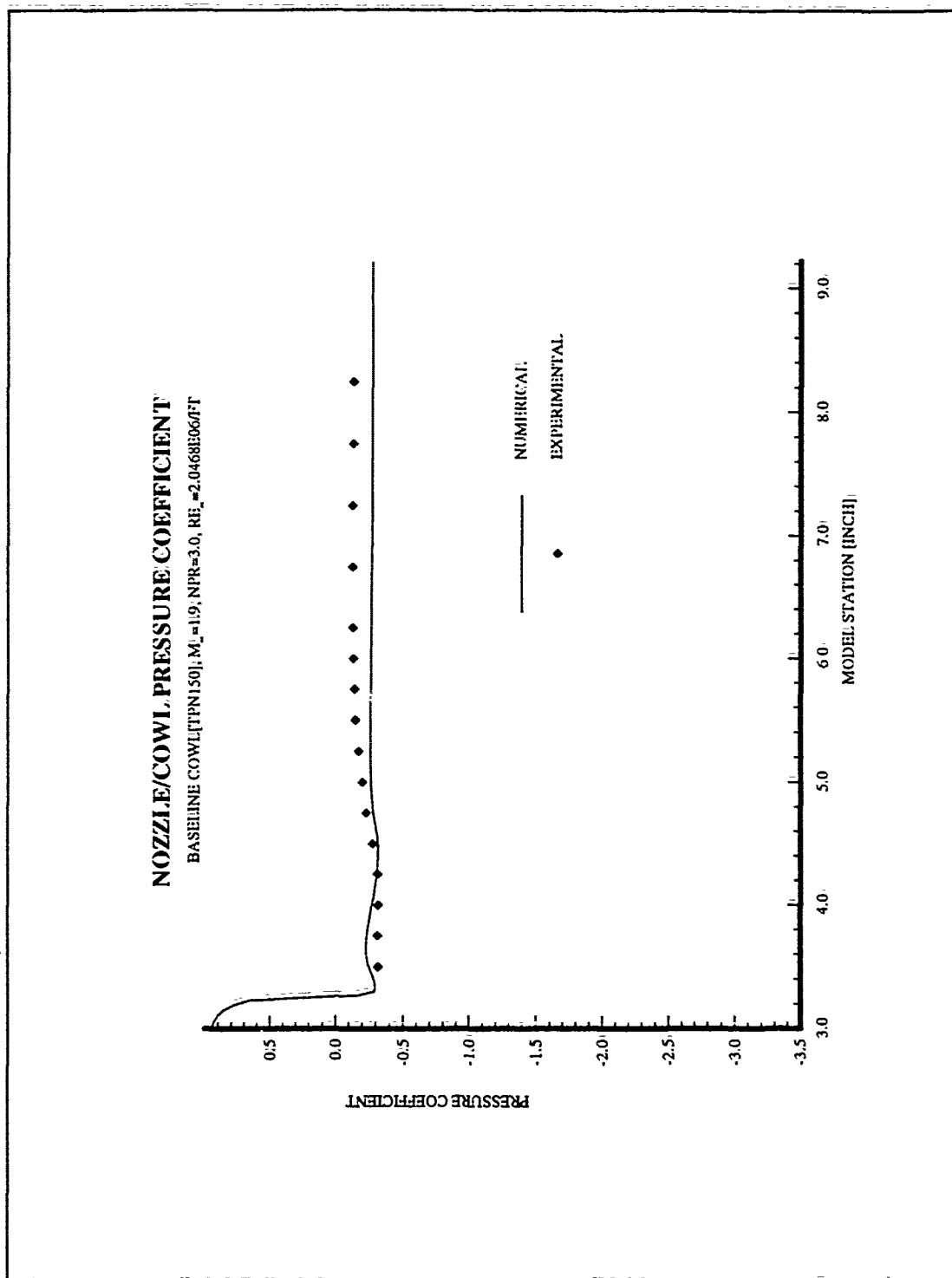


Figure 5-4 Comparison of an Experimental and Numerical Pressure Coefficients (Mach Effects): Baseline Cowl, $M_\infty=1.9$, NPR=3.0

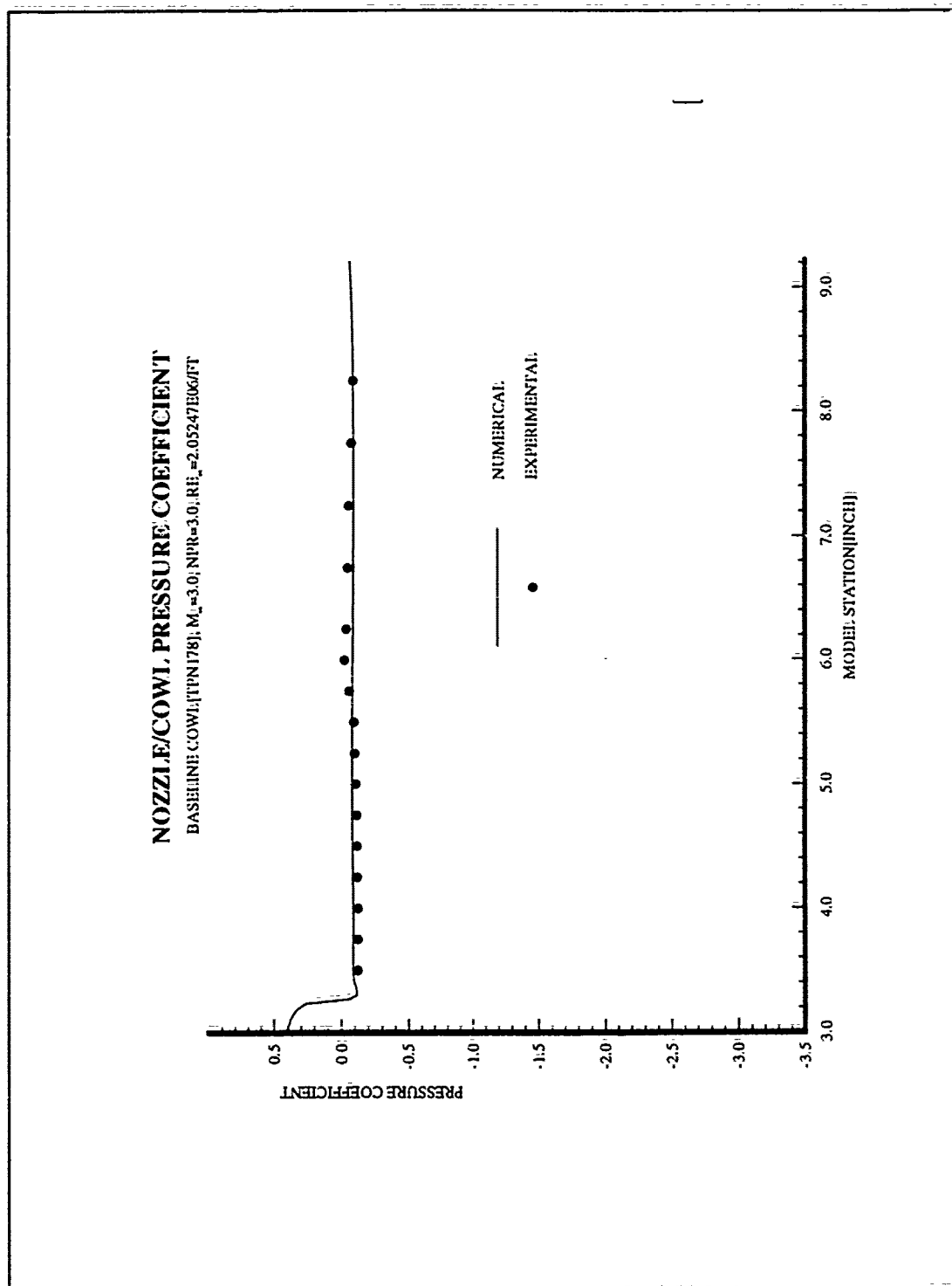


Figure 5-5 Comparison of an Experimental and Numerical Pressure Coefficients (Mach Effects): Baseline Cowl, $M_\infty=3.0$, NPR=3.0

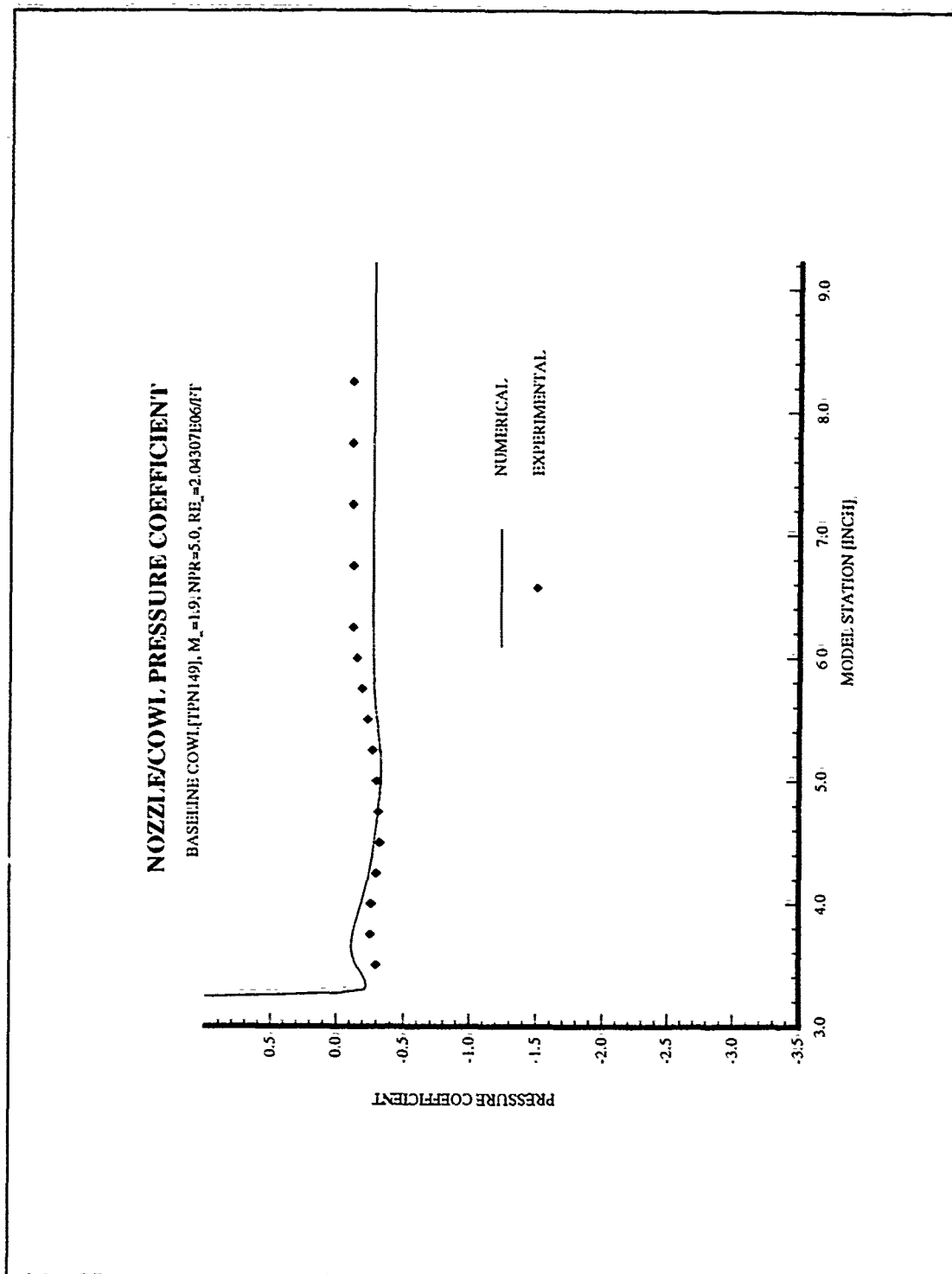


Figure 5-6 Comparison of an Experimental and Numerical Pressure Coefficients (Mach Effects): Baseline Cowl, $M_\infty=1.9$, NPR=5.0

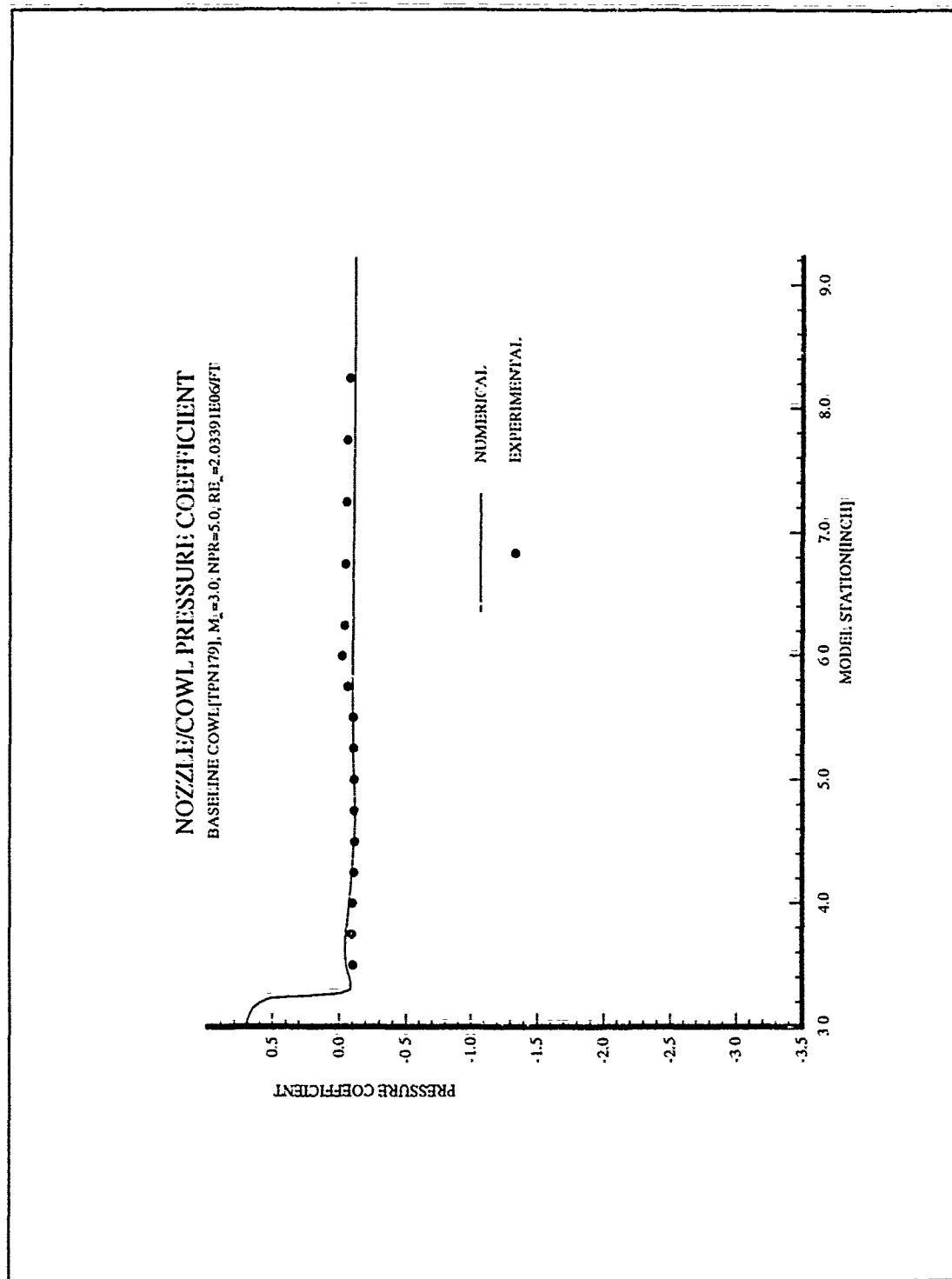


Figure 5-7 Comparison of an Experimental and Numerical Pressure Coefficients (Mach Effects): Baseline Cowl, $M_\infty=3.0$, NPR=5.0

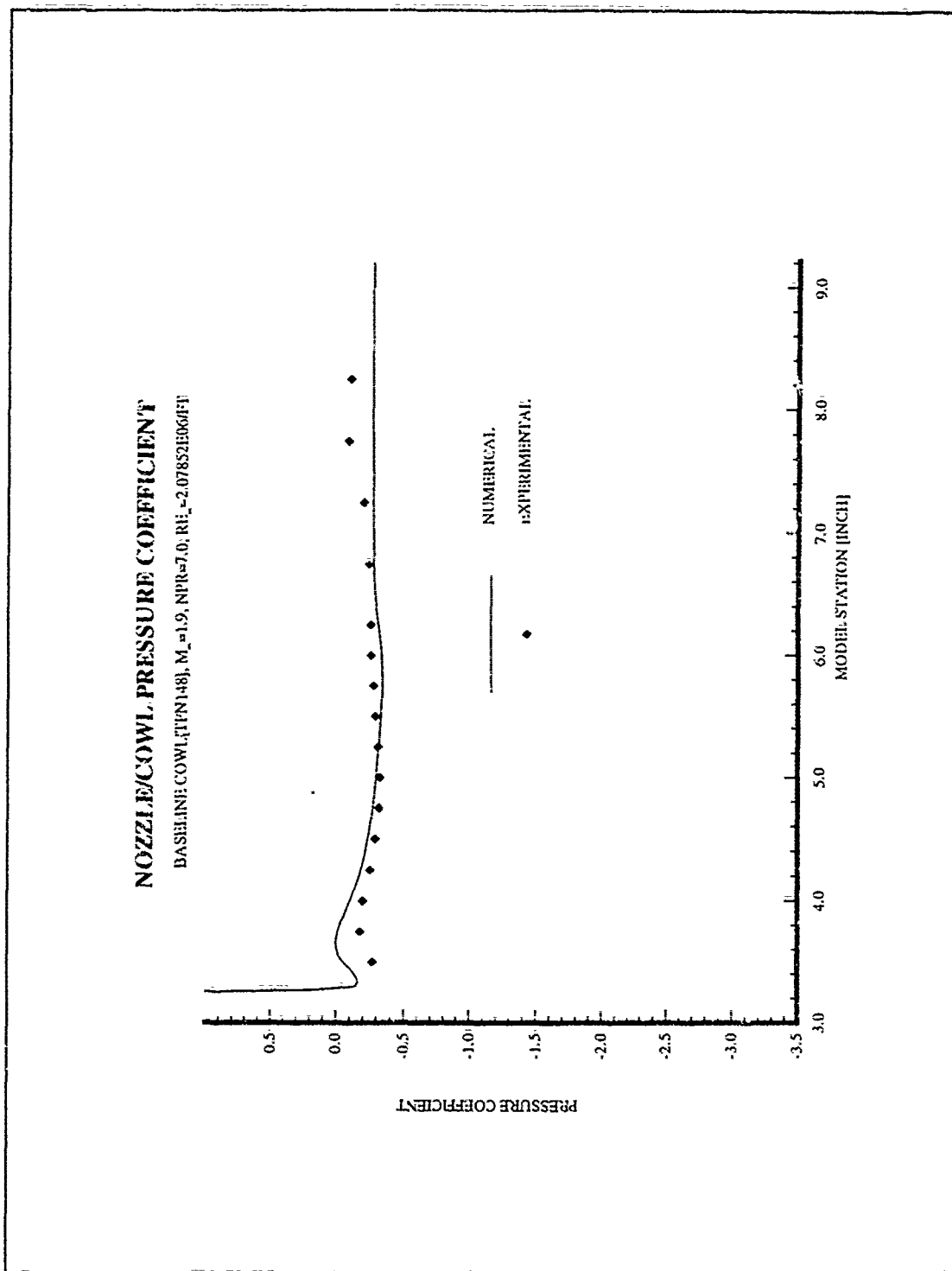


Figure 5-8 Comparison of an Experimental and Numerical Pressure Coefficients (Mach Effects): Baseline Cowl, $M_\infty=1.9$, NPR=7.0

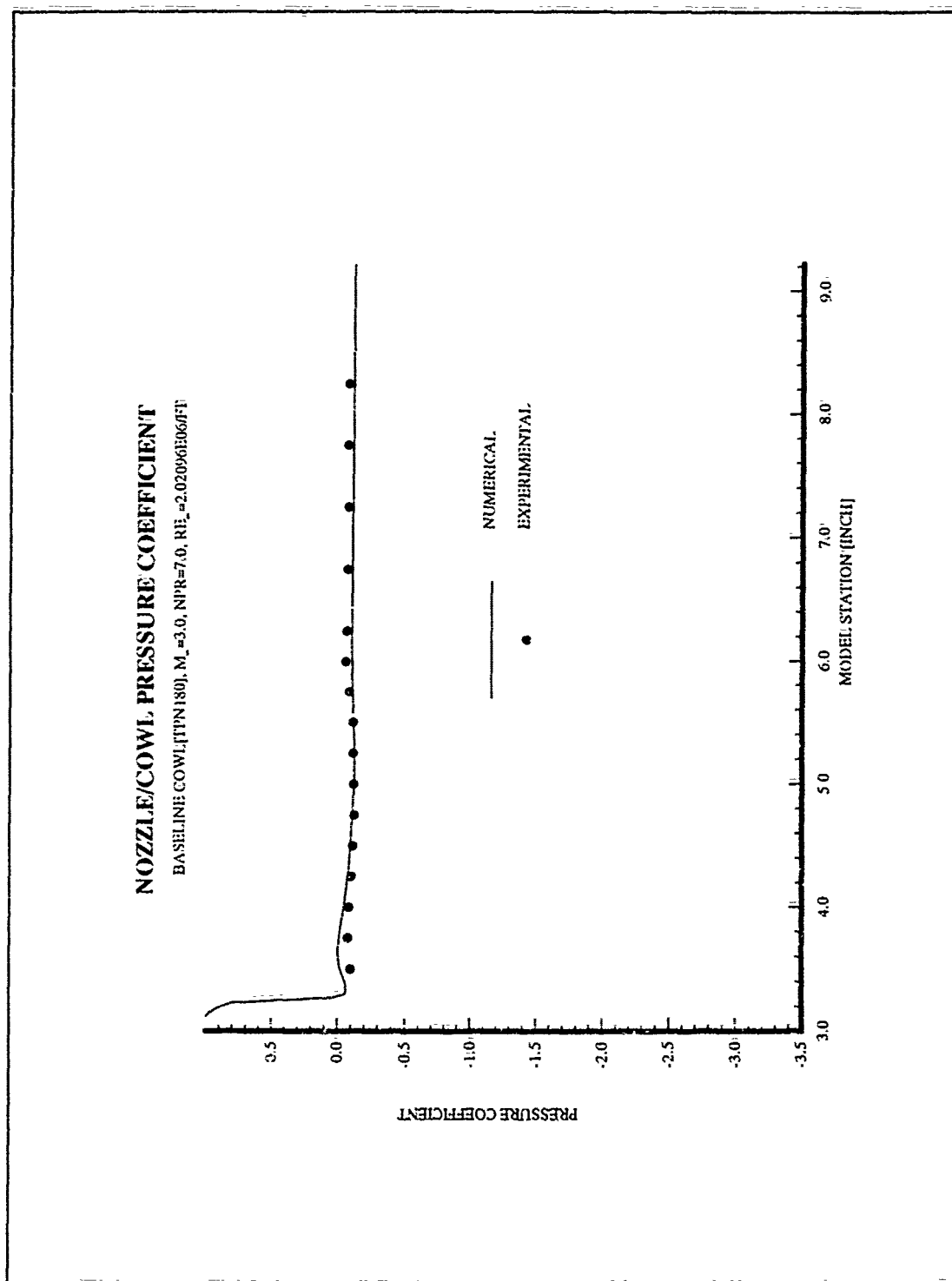


Figure 5-9 Comparison of an Experimental and Numerical Pressure Coefficients (Mach Effects): Baseline Cowl, $M_\infty=3.0$, NPR=7.0

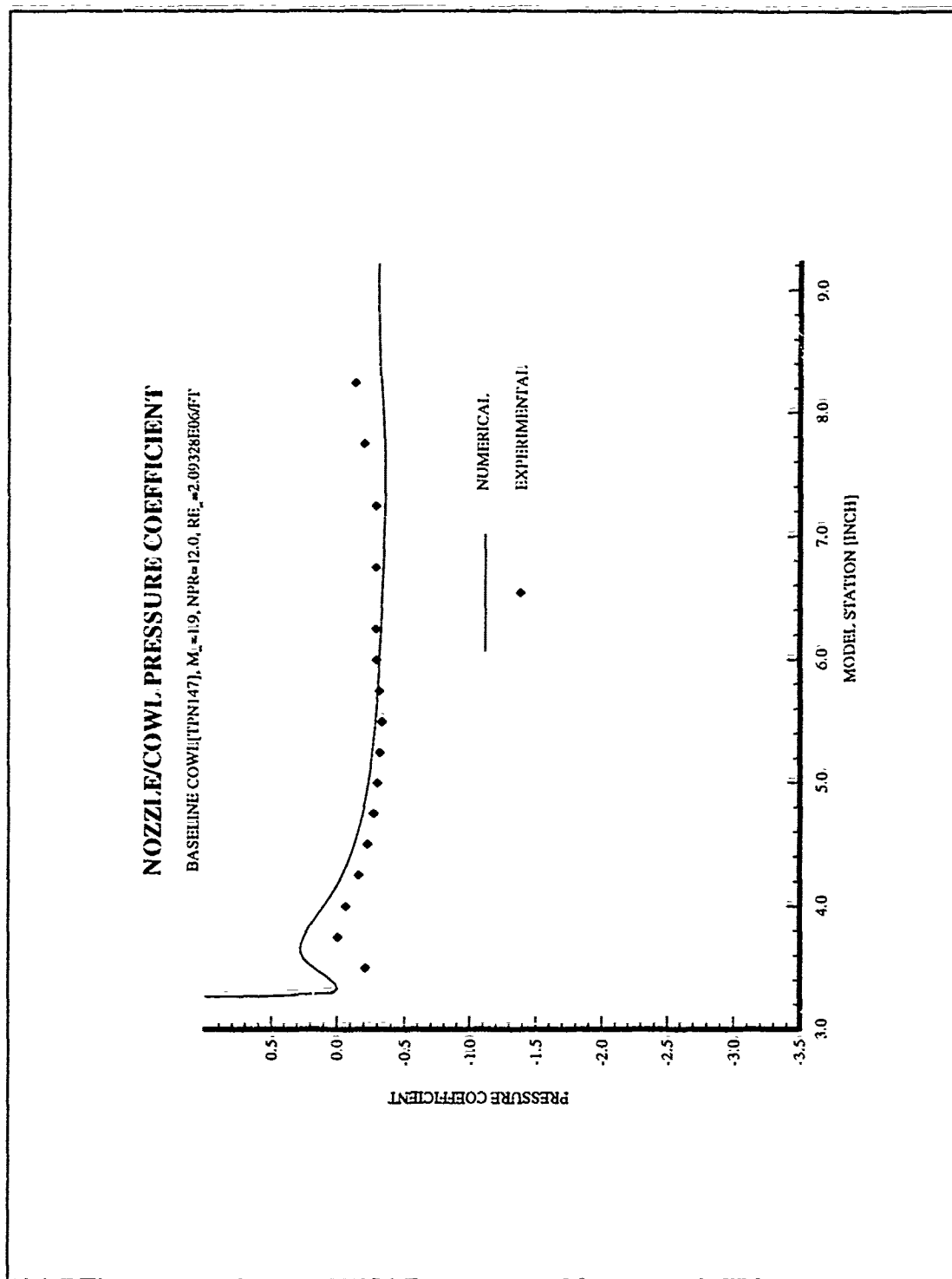


Figure 5-10 Comparison of an Experimental and Numerical Pressure Coefficients (Mach Effects): Baseline Cowl, $M_\infty=1.9$, NPR=12.0

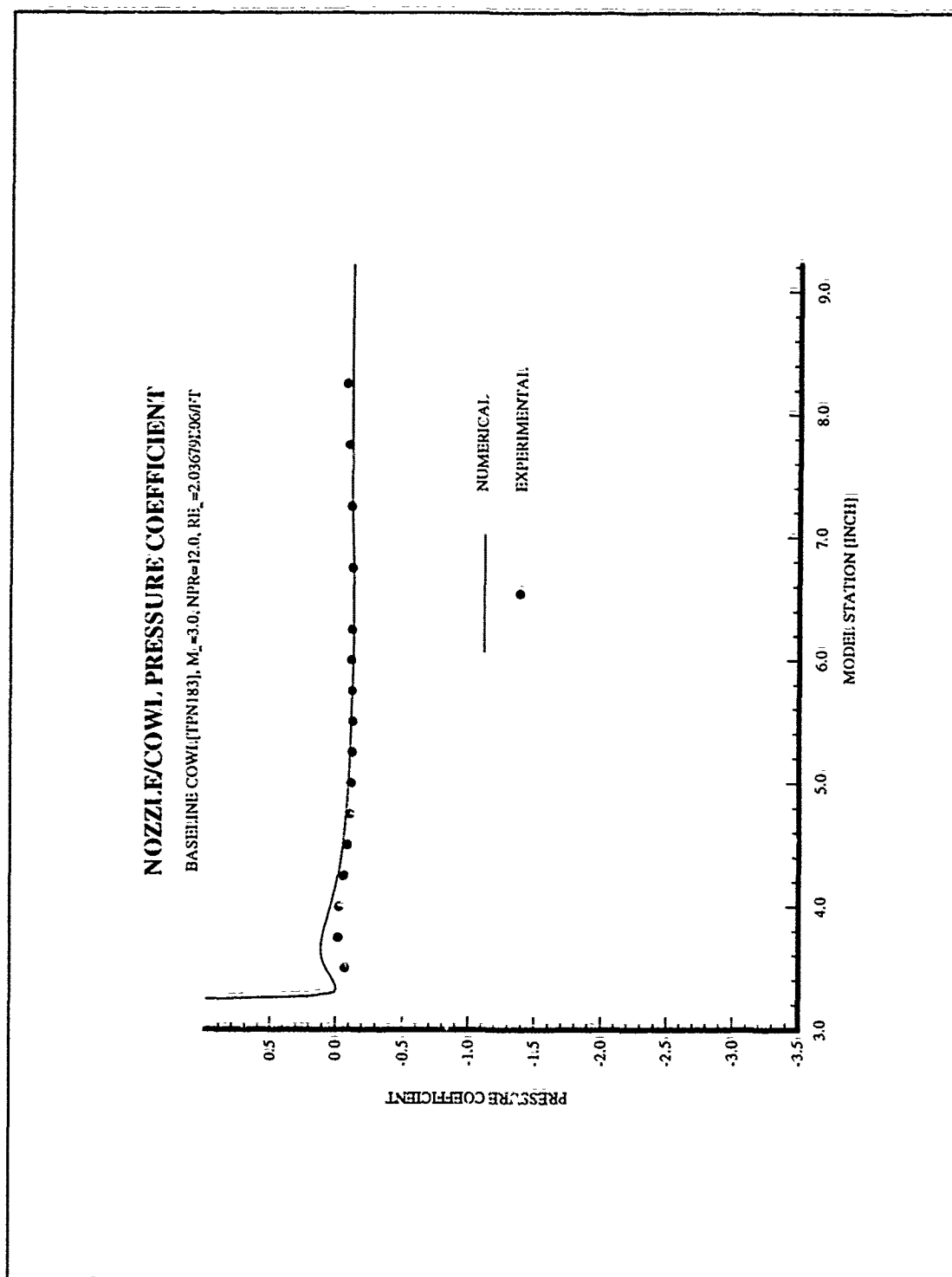


Figure 5-11 Comparison of an Experimental and Numerical Pressure Coefficients (Mach Effects): Baseline Cowl, $M_\infty=3.0$, NPR=12.0

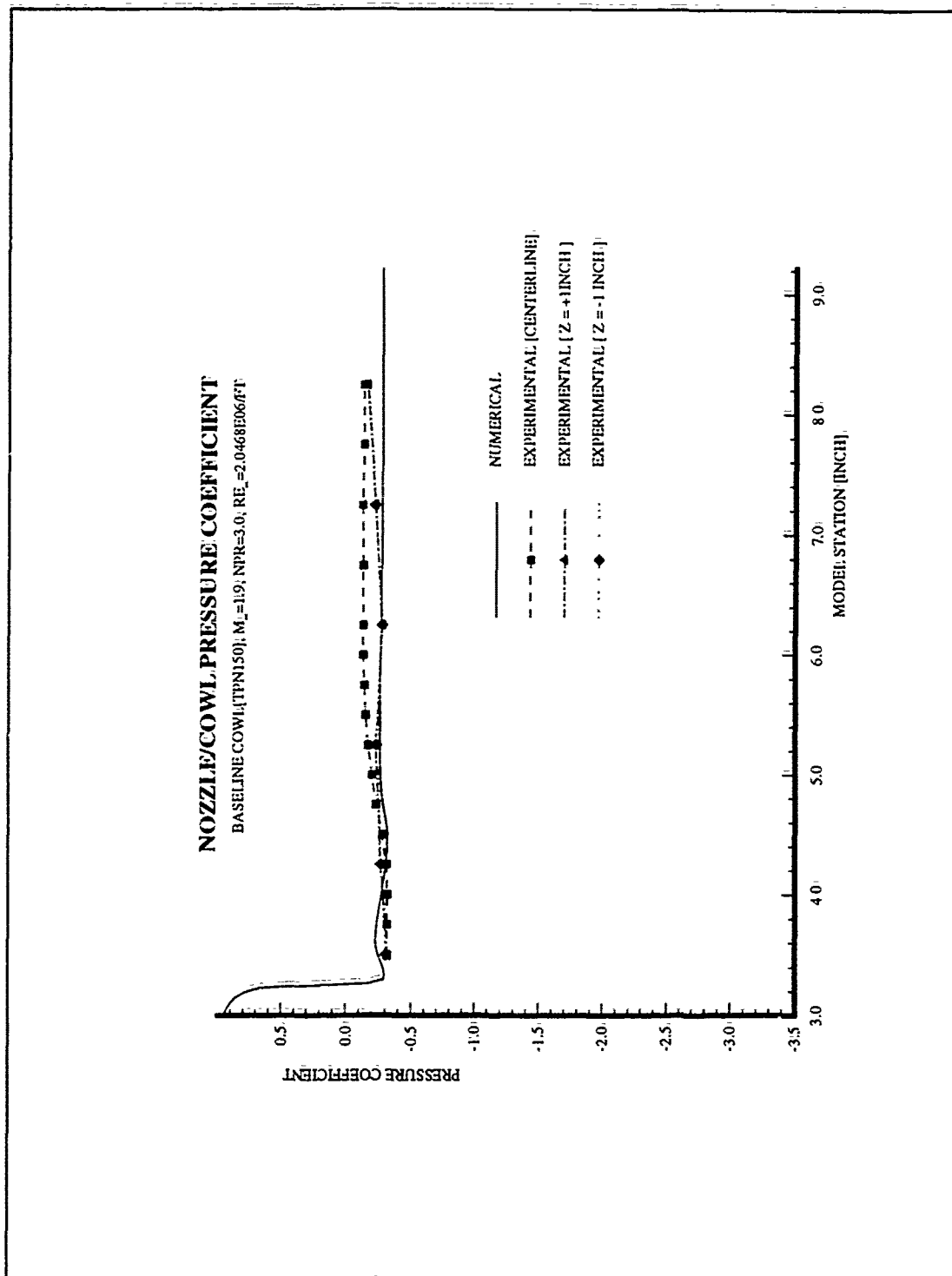


Figure 5-12 Three-Dimensional Effects for the Supersonic Cases: Baseline Cowl, $M_\infty=1.9$, NPR=3.0

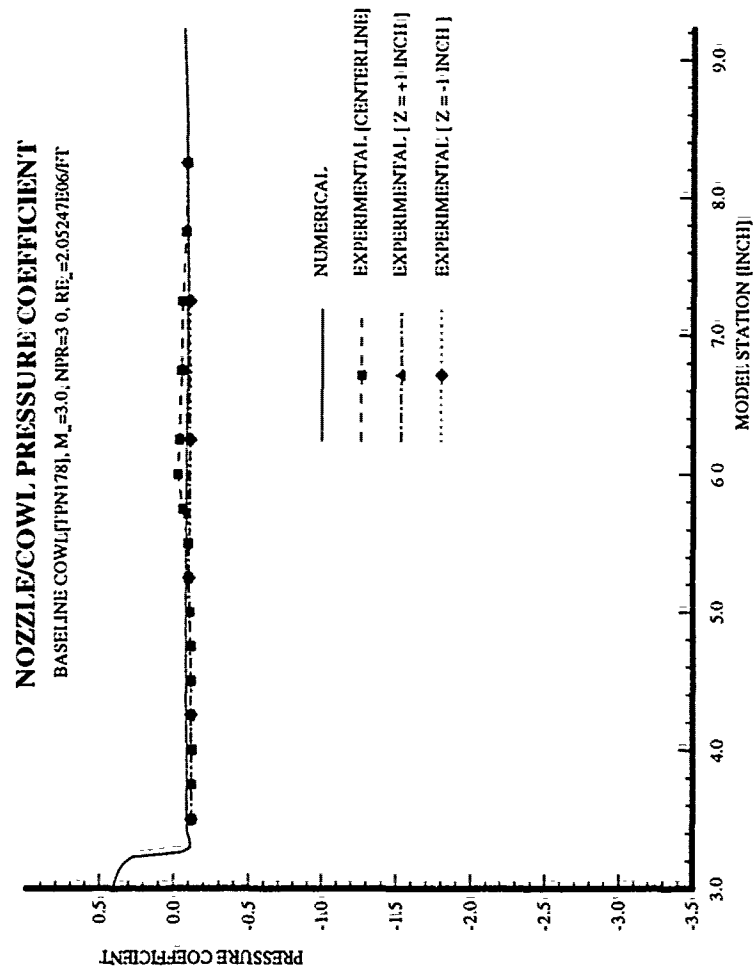


Figure 5-13 Three-Dimensional Effects for the Supersonic Cases: Baseline Cowl, $M_\infty=3.0$, NPR=3.0

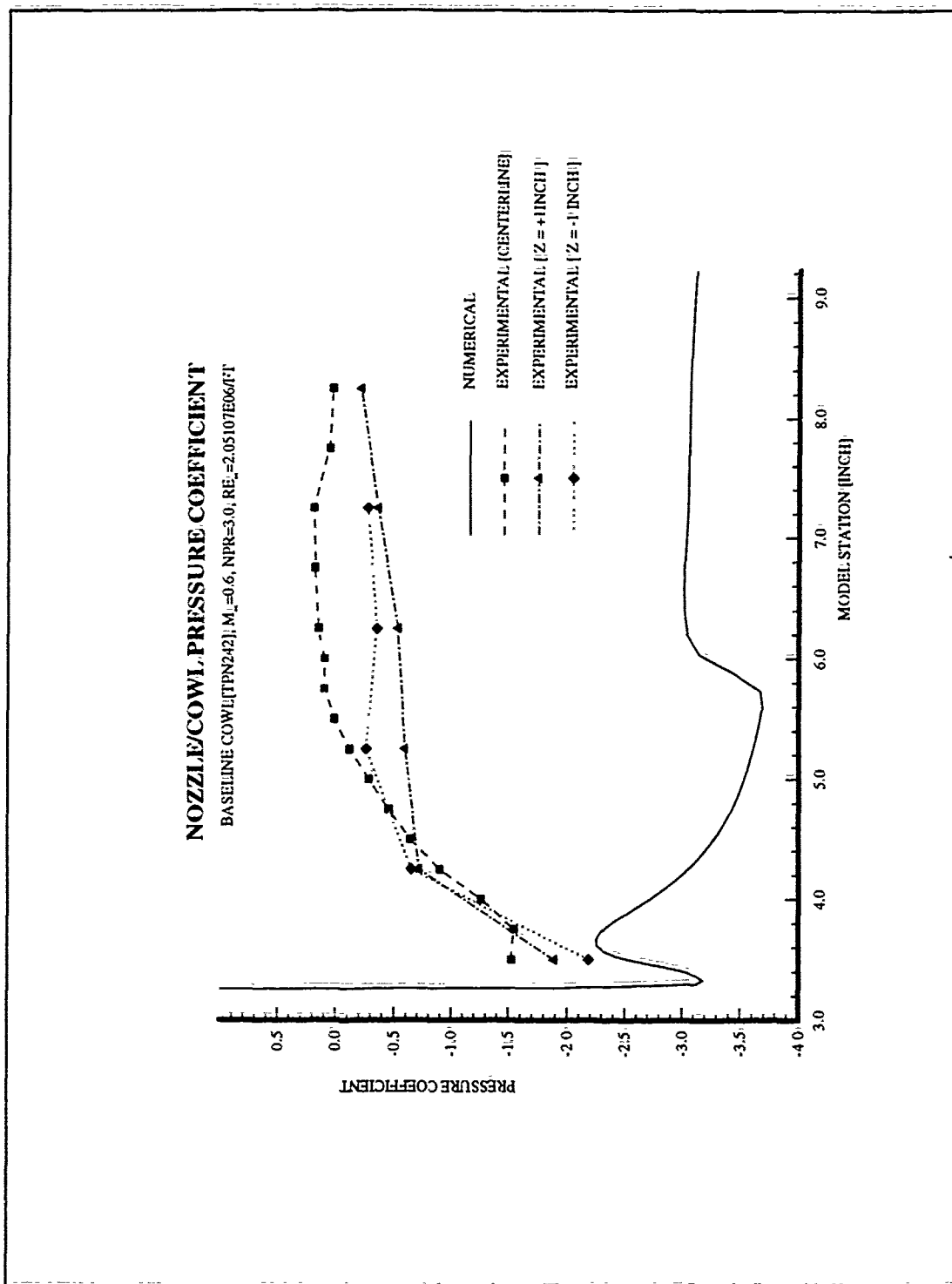


Figure 5-14 Three-Dimensional Effects for the Subsonic Cases: Baseline Cowl, $M_\infty=0.6$, $NPR=3.0$

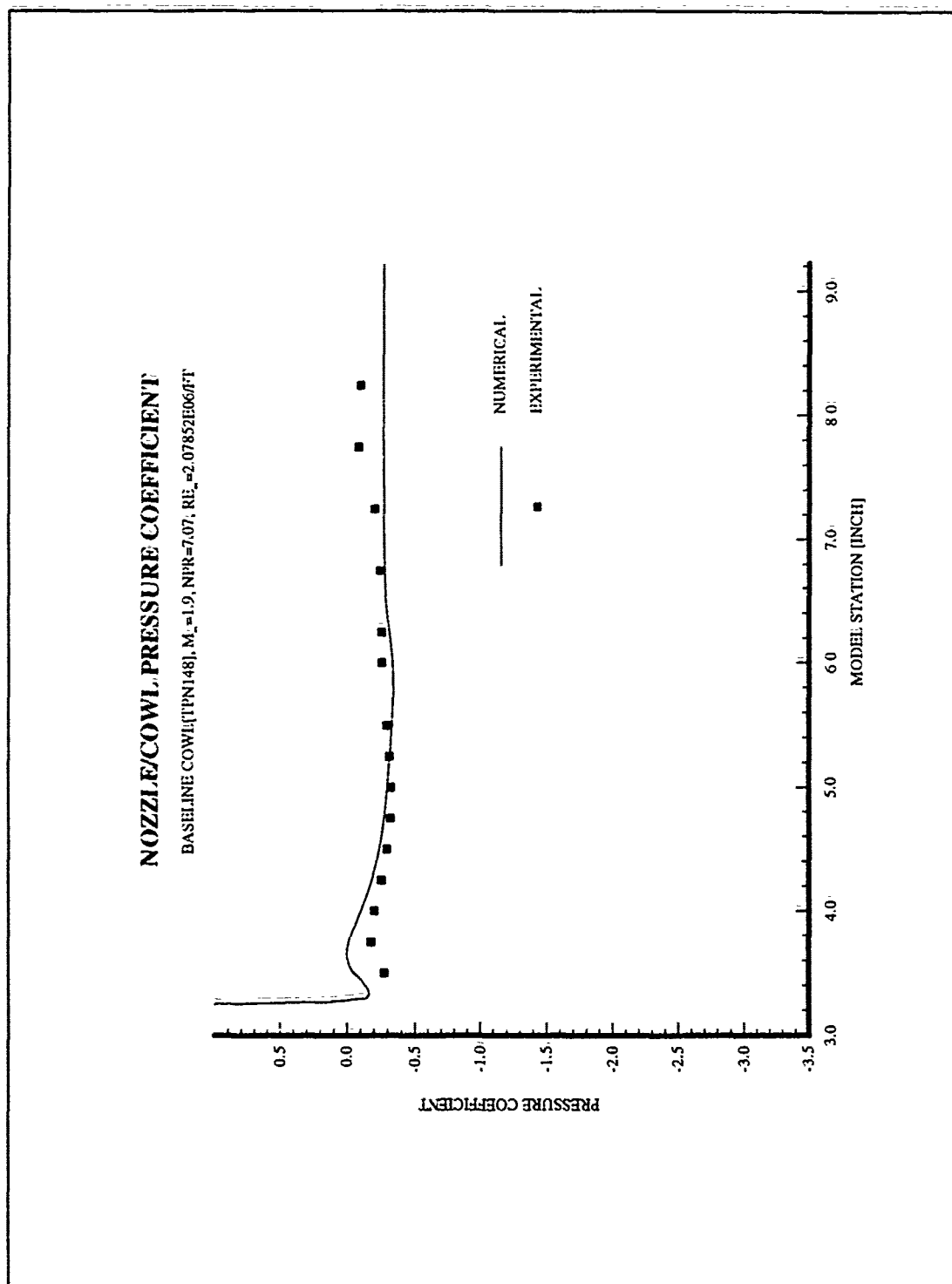


Figure 5-15 Comparison of an Experimental and Numerical Pressure Coefficients (Nozzle Cowl Effects): Baseline Cowl, $M_\infty=1.9$, NPR=7.0

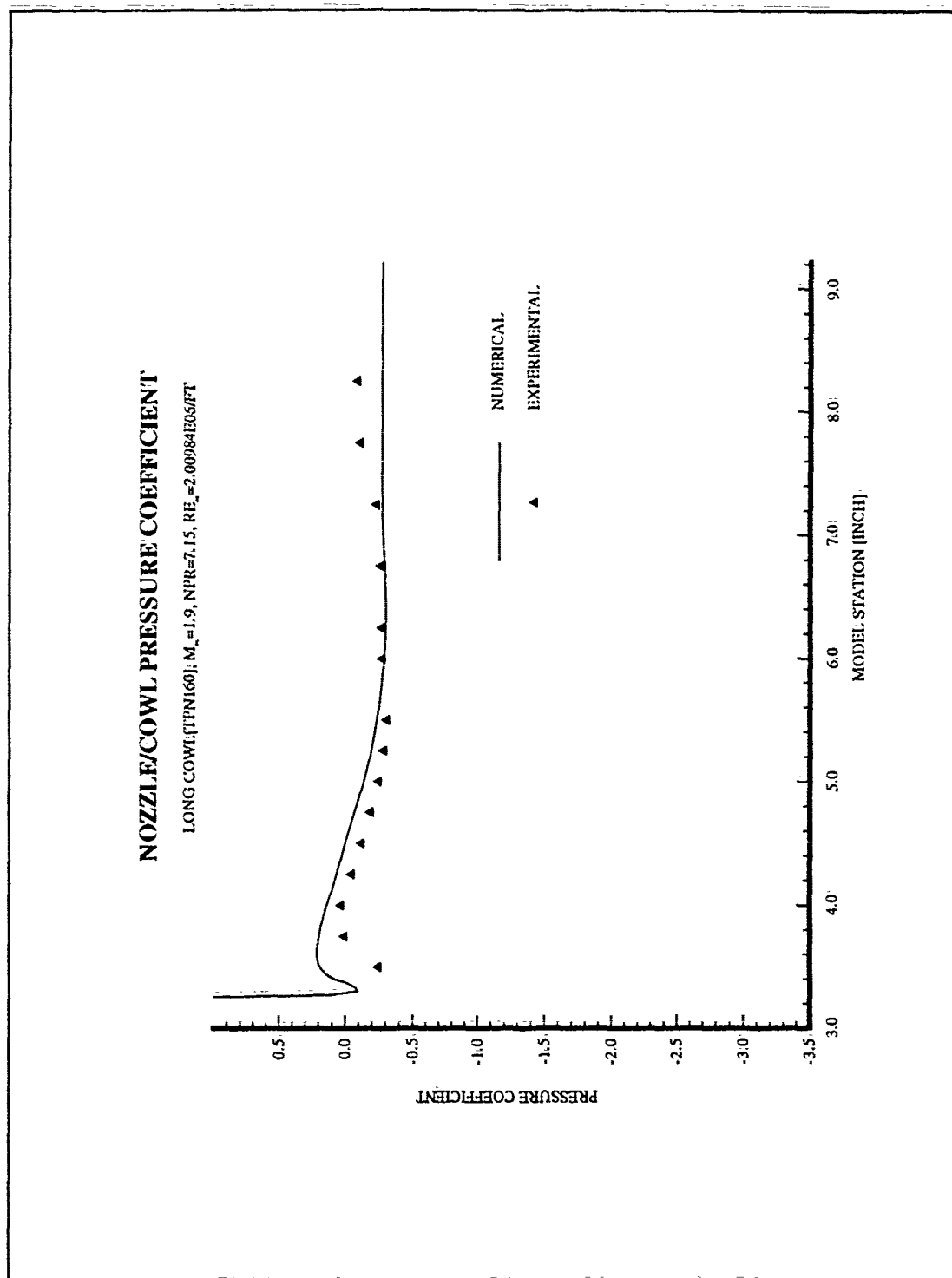


Figure 5-16 Comparison of an Experimental and Numerical Pressure Coefficients (Nozzle Cowl Effects): Long Cowl, $M_\infty=1.9$, NPR=7.0

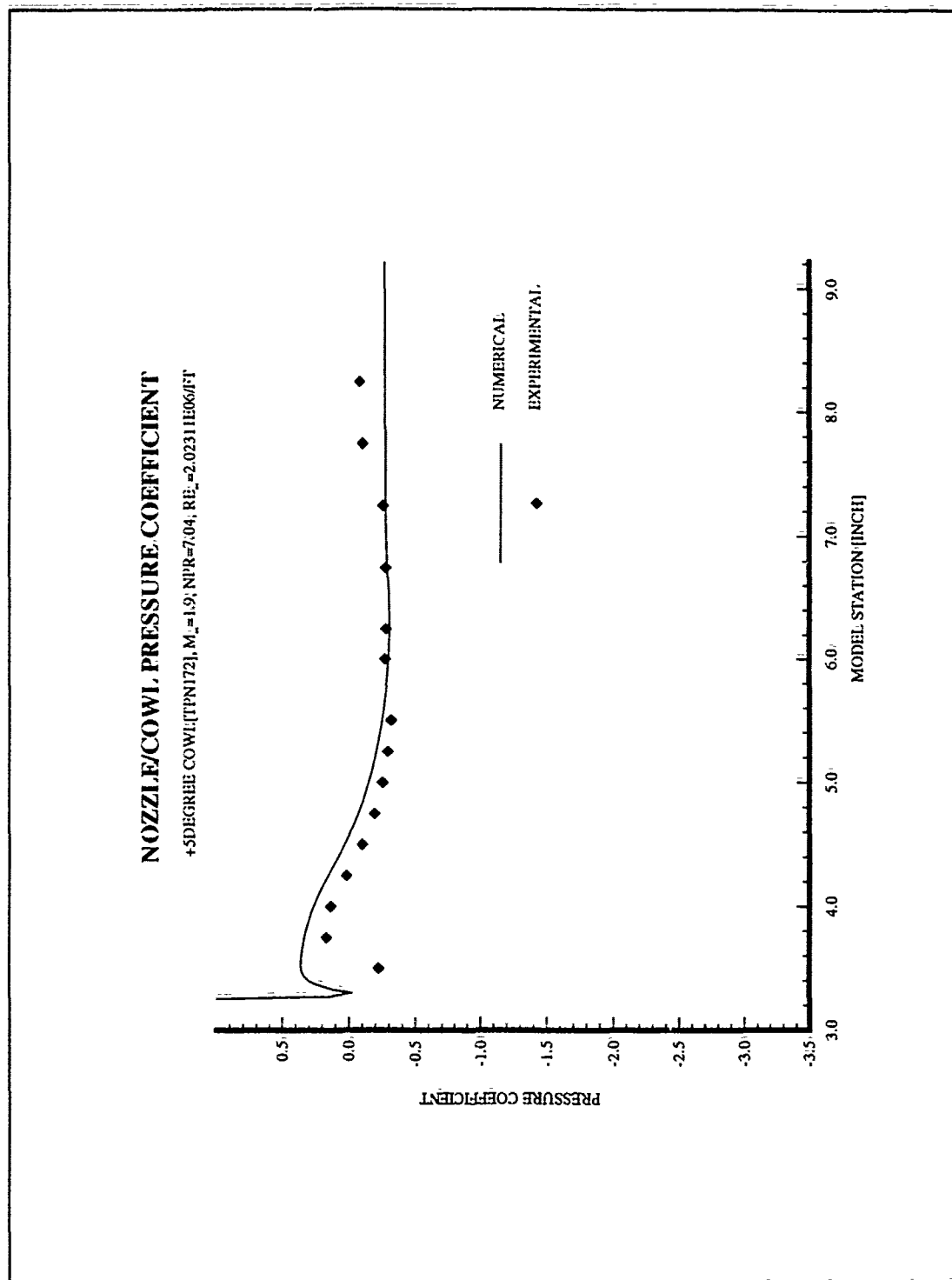


Figure 5-17 Comparison of an Experimental and Numerical Pressure Coefficients (Nozzle Cowl Effects): +5 Degree Cowl, $M_\infty=1.9$, NPR=7.0

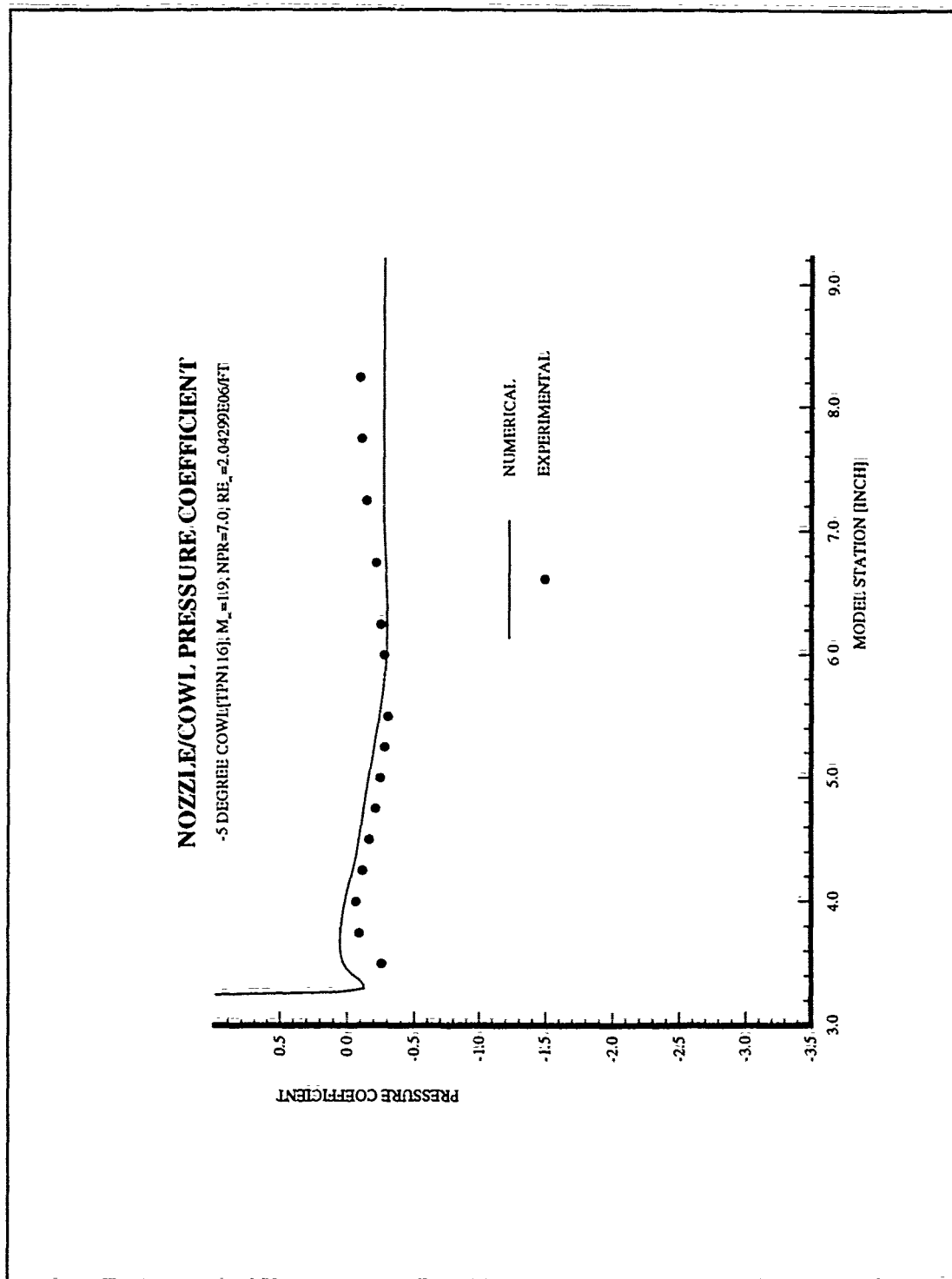


Figure 5-18 Comparison of an Experimental and Numerical Pressure Coefficients (Nozzle Cowl Effects): -5 Degree Cowl, $M_\infty=1.9$, NPR=7.0

NOZZLE/COWL PRESSURE COEFFICIENT
BASELINE COWL [TPN184]; $M_\infty=3.0$; NPR=16.0; $Re_\infty=2.03757 \times 10^6$ ft

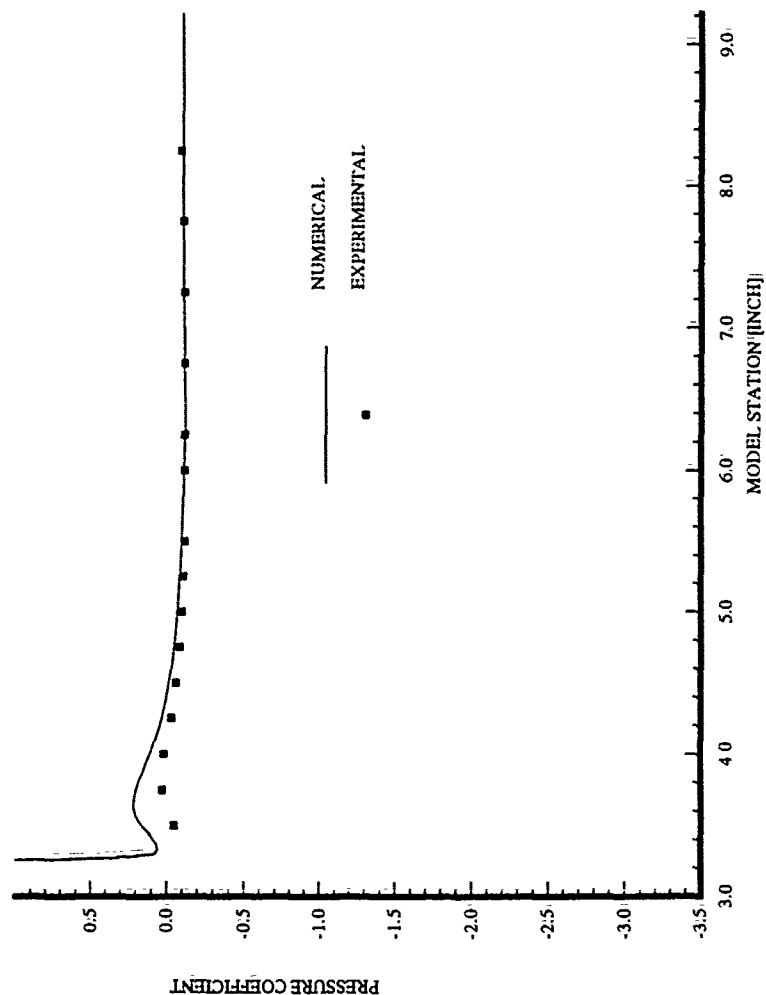


Figure 5-19 Comparison of an Experimental and Numerical Pressure Coefficients (Nozzle Cowl Effects): Baseline Cowl, $M_\infty=3.0$, NPR=16.0

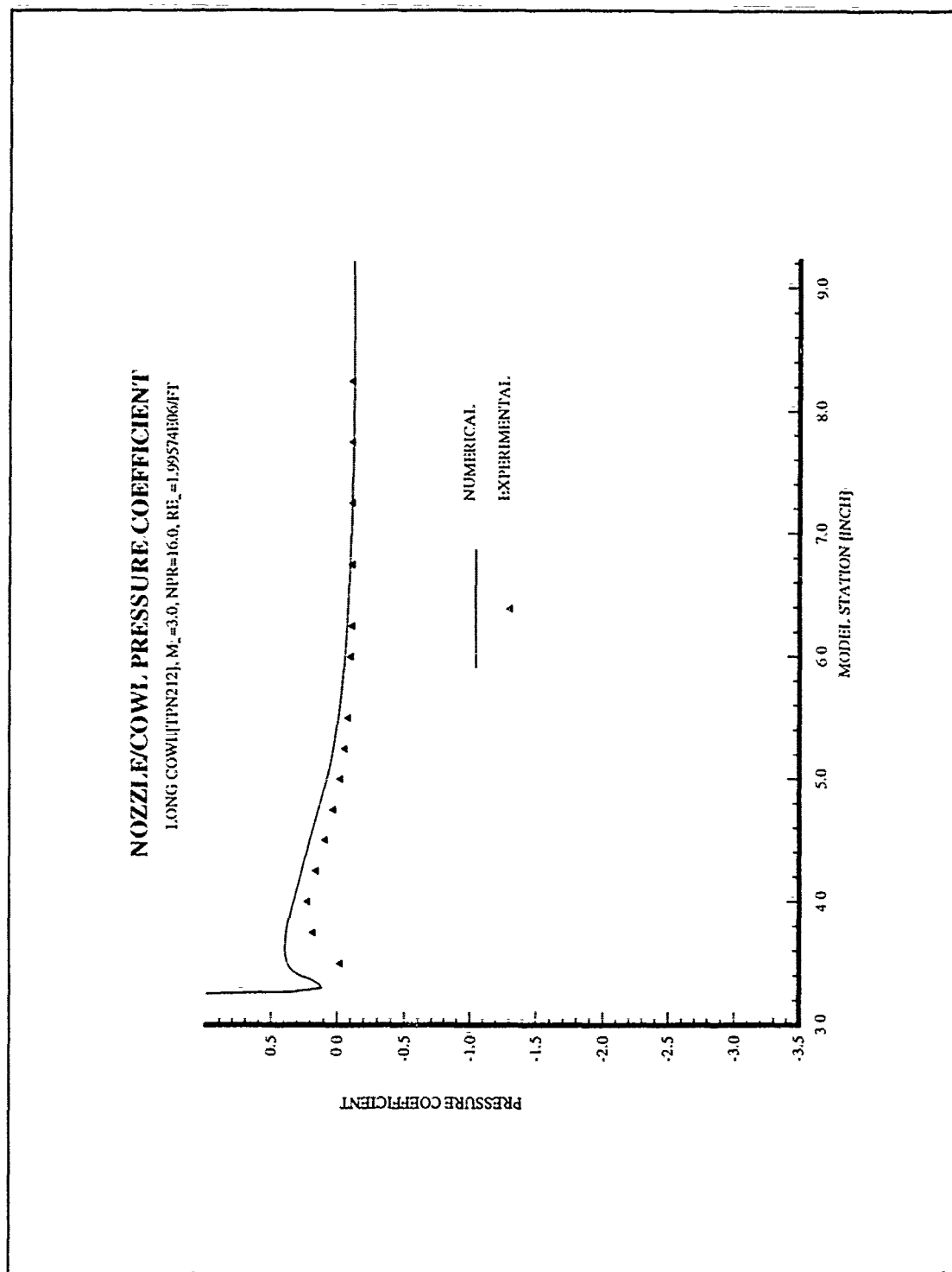


Figure 5-20 Comparison of an Experimental and Numerical Pressure Coefficients (Nozzle Cowl Effects): Long Cowl, $M_\infty=3.0$, NPR=16.0

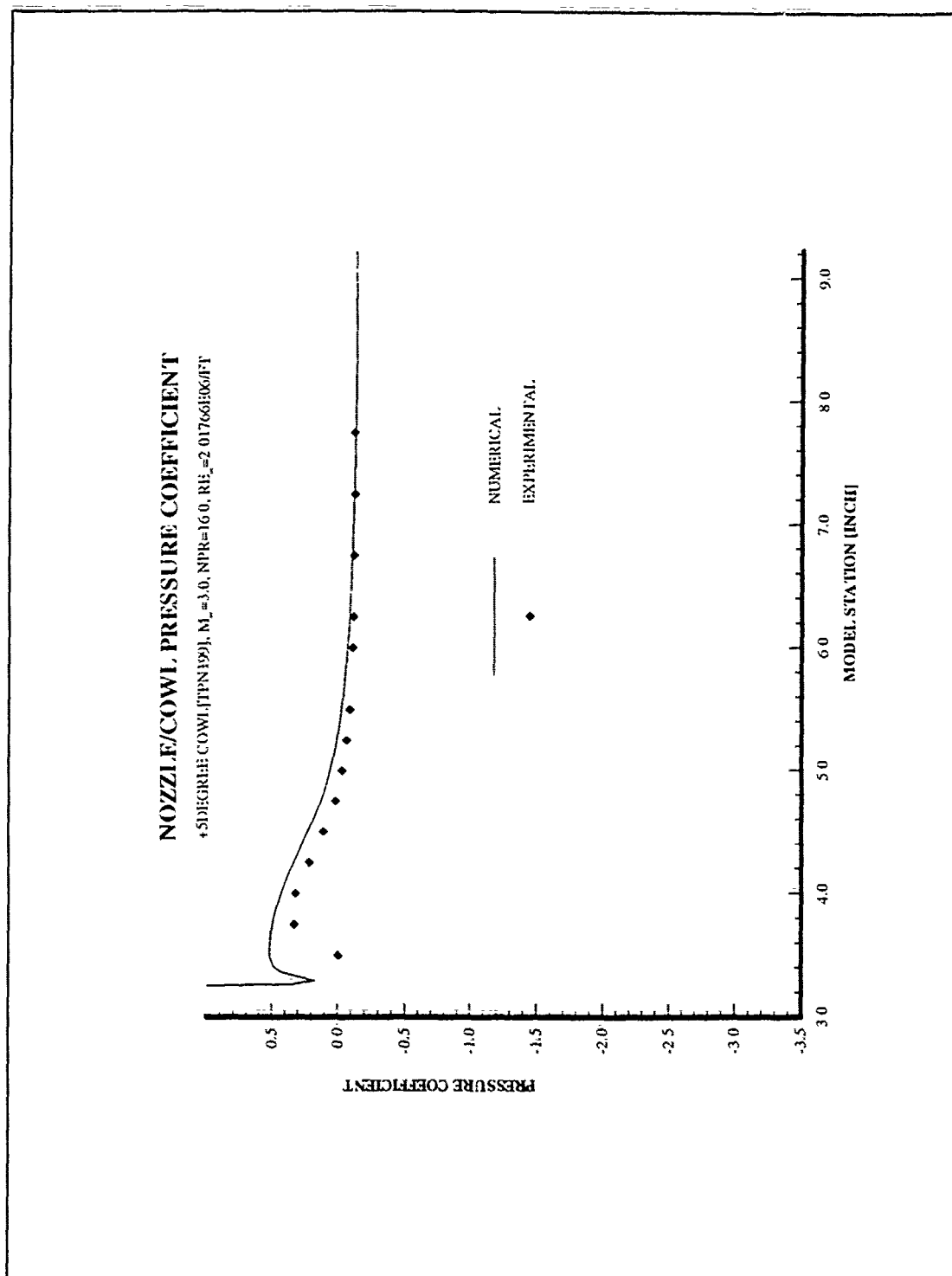


Figure 5-21 Comparison of an Experimental and Numerical Pressure Coefficients (Nozzle Cowl Effects): +5 Degree Cowl, $M_\infty=3.0$, NPR=16.0

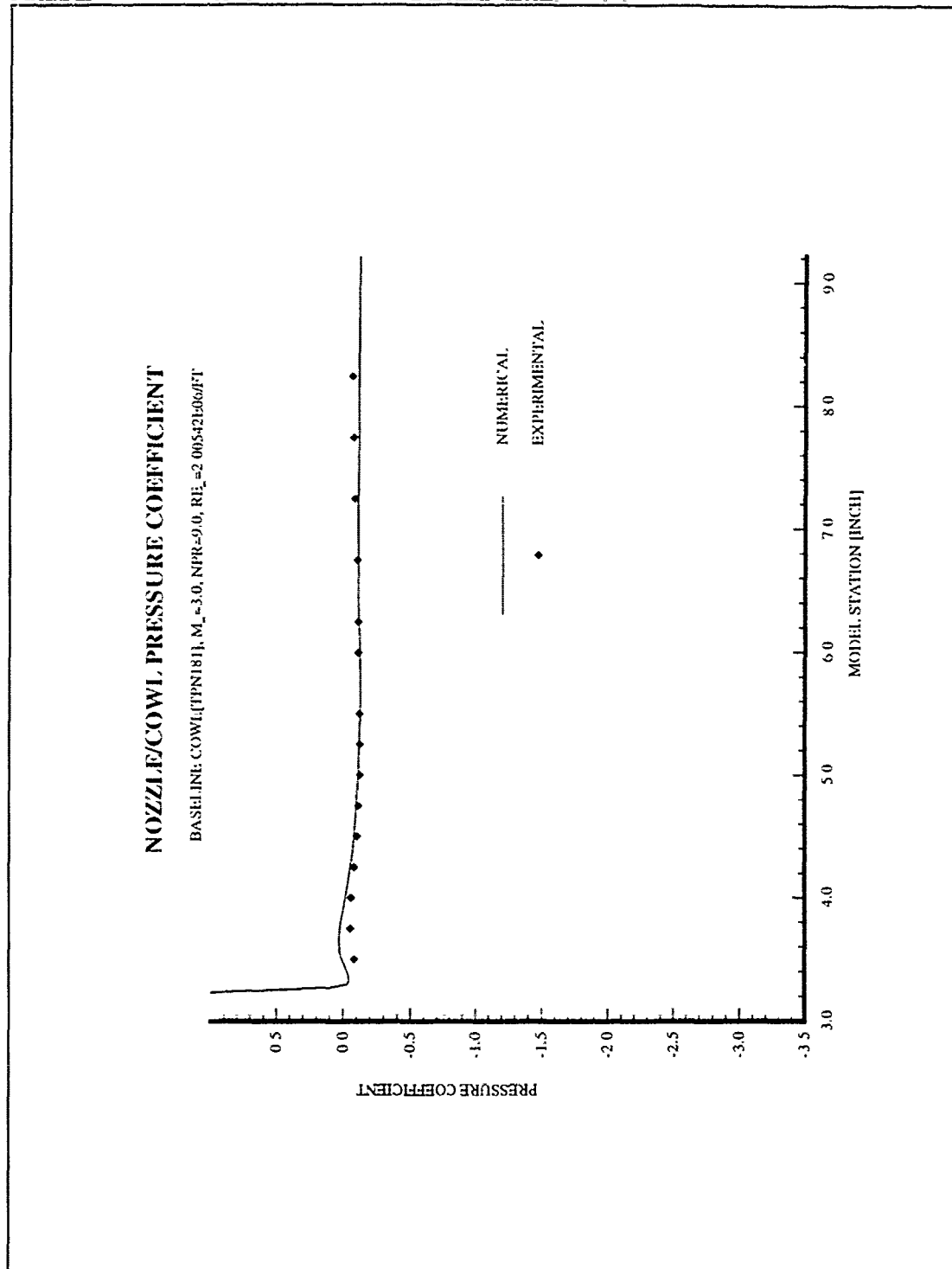


Figure 5-22 Comparison of an Experimental and Numerical Pressure Coefficients (NPR Effects): Baseline Cowl, $M_\infty=3.0$, NPR=9.0

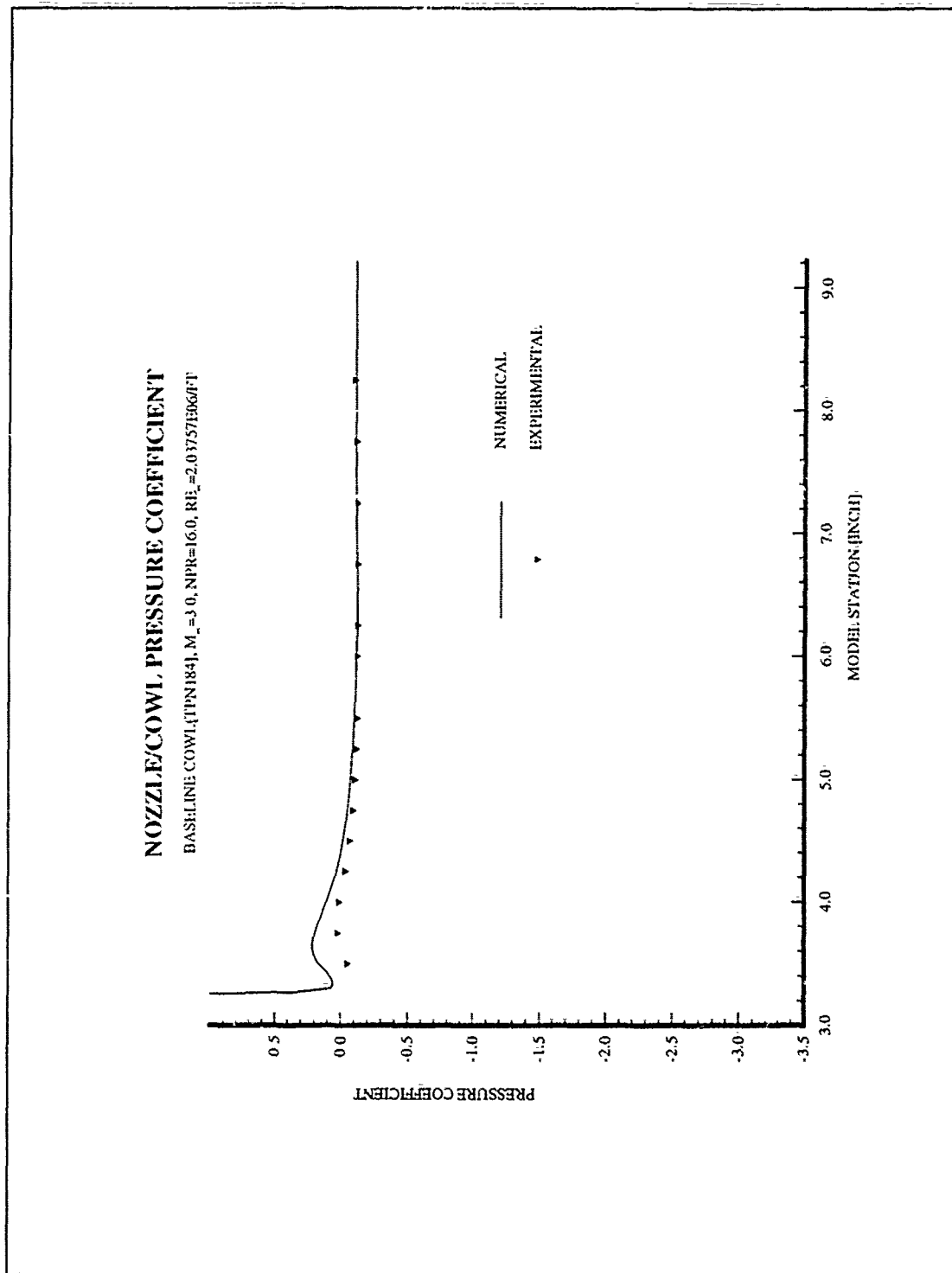


Figure 5-23 Comparison of an Experimental and Numerical Pressure Coefficients (Nozzle Cowl Effects): Baseline Cowl, $M_\infty=3.0$, NPR=16.0

NOZZLE/COWL PRESSURE COEFFICIENT
 BASELINE COWL (TPN186), $M_\infty=3.0$, NPR=20.0, $Re_\infty=2.04416E6/ft$

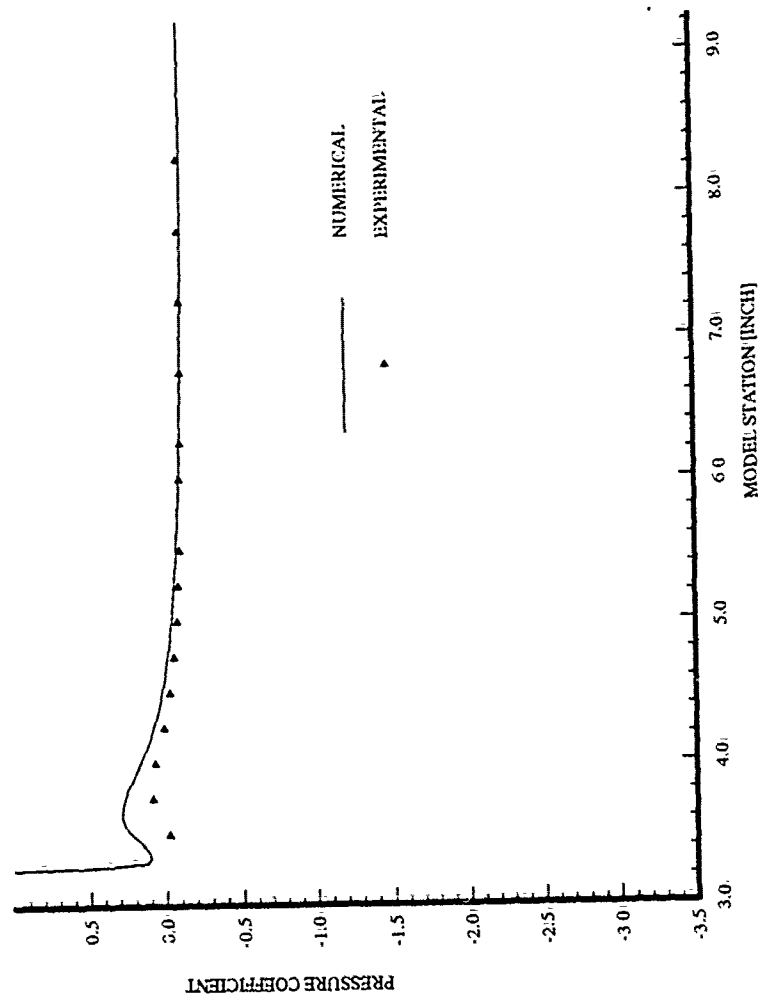


Figure 5-24 Comparison of an Experimental and Numerical Pressure Coefficients (Nozzle Cowl Effects): Baseline Cowl, $M_\infty=3.0$, NPR=1620.0

VI. CONCLUSIONS AND RECOMMENDATIONS

6.1 Conclusions

Off-design flow over a quasi two-dimensional hypersonic nozzle /afterbody model was computationally solved assuming laminar, planar flow to validate the consistency of the experimental data by Cochran (4). Two flux-split algorithms, flux-vector splitting of Van Leer and flux-difference splitting of Roe, were explicitly investigated for this research. The code developed by WL/FIMC performed quite well, its finite volume formulation enhancing the practical stability with skewed cell geometries.

Generation of the two-dimensional grid was a major effort, made simpler by using the GRIDGEN package. The elliptic solver was used to maintain smooth grid contours for the finite volume scheme. In order to provide accurate resolution of the shock region and the boundary layer, the grid points were geometrically clustered.

The two-dimensional explicit flux splitting algorithms performed very well. The finite volume implementation, which the code used for an extremely robust algorithm, handled cells with very small volumes as well as regions with highly skewed cells. The code generally overpredicted the experimental data, with deviations attributable to numerical error in either the afterbody model or in the numerical solution procedure. In particular, the laminar assumption used for the computational model did not accurately capture the initial separation bubble which was most likely turbulent in the experimental tests. Also, the two-dimensional model used in the computational solutions showed inconsistency at the secondary separation bubble due to the interaction between the nozzle plume and the external flow, i.e., the three-dimensional effects.

As expected, the nozzle/afterbody exhaust flow was overexpanded and a separation bubble occurred just downstream of the throat due to the sudden increase of the area in the divergent ramp and the sharp corner at the throat. In addition, the second separation bubble was caused by the interaction of the cowl shock and the boundary layer of the top surface.

The flow recompression and reexpansion properties over all of the nozzle /afterbody depended on the parametric cases and the grid refinement. Generally, as the Mach number and NPR (Nozzle Pressure Ratio) increased, there was increasing agreement between the experimental and the computational results, even though the computational investigation was performed on the basis of the laminar flow assumption. For the +5 degrees and long cowl configurations, the agreement worsened, because of the complicated flow structure and separation region near the sharp throat and the upper surface of the cowl. A refined grid showed that it is possible to analyze the phenomena of the flow in detail and capture the scale of the separation bubble more accurately near the downstream of the throat. The discrepancy of methodology and assumption between the experiment and the theory explains the observed variation in the results.

6.2 Recommendations

This thesis will provide a basis for the solution of a specified nozzle/afterbody problems in further research. The following recommendations are the result of careful consideration of the research and conclusions reached in the course of this thesis.

In Cochran's experimental testing, a three-dimensional hypersonic nozzle /afterbody

model was investigated, but the pressure coefficients for the performance parameter were calculated on the assumption of a two-dimensional model. Also, this numerical research was computationally conducted assuming a two-dimensional model. Some discrepancies between Cochran's three-dimensional and the current two-dimensional models brought about some inconsistency and require further research. Therefore, it is desirable to investigate the three-dimensional computational model and validate the experimental results. Furthermore, future plans should include turbulence modeling and validation of the revised code with nozzle/afterbody experimental data.

Bibliography

1. Stephen M. Ruffin, E. Venkatapathy, E. R. Keener, and N. Nagaraj, Computational Design Aspects of a NASP Nozzle/Afterbody Experiment, AIAA 89-0446, January 1989.
2. Lawrence D. Huebner and Kenneth E. Tatum, "Computational and Experimental Aftbody Flow Fields for Hypersonic, Airbreathing Configurations with Scramjet Exhaust Flow Simulation," AIAA 91-1709.
3. Anderson, John D. Jr., *Hypersonic and High Temperature Gas Dynamics*, New York: McGraw-Hill Book Company, 1989.
4. Cochran R. Bruce, *Hypersonic Nozzle/Afterbody Performance at Low Mach Numbers*, MS Thesis, AFIT/GAE/ENY/89J-2, School of Engineering, Air Force Institute of Technology (AU), Wright-Patterson AFB, OH, December 1989.
5. W. K. Anderson, J. L. Thomas, and B. van Leer, "Comparison of Finite Volume Flux Vector Splitting for the Euler Equation," AIAA Journal Vol. 24, No. 9, September 1986.
6. Gaitonde, Datta, *Computation of Viscous Shock/Shock Hypersonic Interactions with an Implicit Flux Split Scheme*. Final Report for Period September 1989-September 1990. Wright-Patterson AFB Ohio: Universal Energy Systems, December 1990, (WRDC-TR-90-3076).
7. Gaitonde, Datta, *The Performance of Flux-Split Algorithms in High-Speed Flows*. AIAA 92-0186, 30th Aerospace Sciences Meeting and Exhibit. Reno, Nevada, January 1992.
8. Gaitonde, Datta, *Hypersonic Flow Simulation with Upwind Methods*, Computational Fluid Dynamics Short Course, Wright-Patterson AFB, Ohio, 21-24 September 1992.
9. Gaitonde, Datta, Personal Interviews. WL/FIMC, Wright-Patterson AFB, Ohio, 1 March through 30 April 1993.
10. Robert W. MacCormack, "The Effect of Viscosity in Hypervelocity Impact Cratering," AIAA Paper No. 69-354
11. Klaus A. Hoffmann, *Computational Fluid Dynamics for Engineers*. Austin, Texas, A Publication of Engineering Education System, 1989.

12. James A. Mundy V, *The Effect of Viscosity On A Conically Derived Waverider*, MS Thesis, AFIT/GAE/ENY/92D-2, School of Engineering, Air Force Institute of Technology (AU), Wright-Patterson AFB, OH, December 1992.
13. Jameson, Antony, "Computational Algorithm for Aerodynamic Analysis and Design," Contribution to the INRIA 25th Anniversary Conference on Computer Science and Control, Paris. December 1992.
14. Beran, P. Class handout distributed in Aero 752, Computational Fluid Dynamics. School of Engineering, Air Force Institute of Technology (AU), Wright-Patterson AFB Ohio, March 1992.
15. H. C. Yee, *A Class of High-Resolution Explicit and Implicit Shock-Capturing Methods*, NASA TM 101088, February 1989.
16. Steinbrenner, John P. et al. *The GRIDGEN 3D Multiple Block Grid Generation System: Interim Report*, 1 October 1987-1 October 1990, Contract F33615-87-C-3003, Fort Worth Texas: General Dynamics Corporation, April 1991 (WRDC-TR90-3022).
17. Edwards, A. Thomas, *The Effects of Exhaust Plume/Afterbody Interaction on Installed Scramjet Performance*, NASA TM 101033, 1981.
18. Kumar, Ajay, *Numerical Analysis of the Scramjet-inlet Flow Fields by Using Two-Dimensional Navier-Stokes Equations*. NASA TP-1940, 1981.
19. Anderson, Dale A. et al. *Computational Fluid Mechanics and Heat Transfer*. New York, Hemisphere Publishing, 1984.

12. James A. Mundy V, *The Effect of Viscosity On A Conically Derived Waverider*, MS Thesis, AFIT/GAE/ENY/92D-2, School of Engineering, Air Force Institute of Technology (AU), Wright-Patterson AFB, OH, December 1992.
13. Jameson, Antony, "Computational Algorithm for Aerodynamic Analysis and Design," Contribution to the INRIA 25th Anniversary Conference on Computer Science and Control, Paris, December 1992.
14. Beran, P. Class handout distributed in Aero 752, Computational Fluid Dynamics. School of Engineering, Air Force Institute of Technology (AU), Wright-Patterson AFB Ohio, March 1992.
15. H. C. Yee, *A Class of High-Resolution Explicit and Implicit Shock-Capturing Methods*, NASA TM 101088, February 1989.
16. Steinbrenner, John P. et al. *The GRIDGEN 3D Multiple Block Grid Generation System: Interim Report*, 1 October 1987-1 October 1990, Contract F33615-87-C-3003, Fort Worth Texas: General Dynamics Corporation, April 1991 (WRDC-TR90-3022).
17. Edwards, A. Thomas, *The Effects of Exhaust Plume/Afterbody Interaction on Installed Scramjet Performance*, NASA TM 101033, 1981.
18. Kumar, Ajay, *Numerical Analysis of the Scramjet-inlet Flow Fields by Using Two-Dimensional Navier-Stokes Equations*, NASA TP-1940, 1981.
19. Courant, R., Friedrichs, K. O., and Lewy, H. (1928). Über die Partiellen Differenzengleichungen der Mathematischen Physik, *Mathematische Annalen*, vol. 100, pp. 32-74. (Translated to: On the Partial Difference Equations of Mathematical Physics, *IBM J. Res. Dev.*, vol. 11, pp. 215-234, 1967.)

APPENDIX A: CN1DAT CONTROL FILE

IL, JL, IMETRC

102 72 0

NEND

1000

ICFL, CFLEXP, CFLMAX, CFL

5 1 0.9 0.01

IREST, CFCRHO, CFCEI, CFLPEN, CEXPPEN, INOFRZ

1 5.00 5.00 1 1 1

IMPLT, ILCTST, ISWVL, ILMTR, OMEGA, DELTEP, DELTIL, IENTH, INS, NSWPS

0 1 4 2 1 1.E-10 0.5 2 1 2

IADBWL, ICASE, TWALL, ALPHA, RM, REL, RL, TINF, IGRID

0 2 400.6 0. 1.9026 2.00984E6 1.0 105.192 2

IREAD, IP3DOP, IDGBUG, MODPR, NRST, IFMRTI, IFMRTO, IINT1

1 2 0 5 0 1 1 1

INS1, INS2, JNS1, JNS2

1 52 37 46

TINWALL, AINLPHA, RINM, RINEL, RINL, TININF IGRID

400.6 0. 0.29892 1.25155E+6 1.0 481.56 2

APPENDIX B: NOZZLE/AFTERBODY DATA

Table B-1 Mach Number Effects

TPN	PN	M _∞	NPR	RE _∞ /RT(10 ⁶)	P _∞	T _∞	M _n	RE _n	P _n	T _n
240	11	0.60196	0.90310	2.05019	1001.8	513.31	0.31000	0.89962	846.370	509.91
253	11	0.80673	0.82424	2.03254	699.65	490.81	0.29000	0.55799	543.968	497.69
151	11	1.89870	0.96161	2.03139	170.60	323.73	0.26701	0.15287	156.120	483.92
177	11	3.00480	0.82552	1.99890	52.772	199.29	0.20000	0.03188	42.3660	474.43
242	11	0.60313	3.08510	2.05107	1004.9	515.16	0.31037	3.30618	2899.80	483.29
255	11	0.80167	3.09050	2.02502	702.99	491.64	0.29427	2.26345	2045.80	474.69
150	11	1.89880	2.98720	2.04680	170.31	321.58	0.31067	0.54214	475.840	483.92
178	11	3.00470	3.10340	2.05247	52.786	195.84	0.22789	0.13337	158.000	480.20
244	11	0.60090	4.89080	2.02823	1002.1	517.06	0.31070	5.83063	4583.80	444.63
257	11	0.80367	5.07300	2.03180	702.72	491.17	0.29865	3.96144	3351.00	456.25
149	11	1.89900	4.99910	2.04307	169.61	321.07	0.31782	0.91714	790.550	485.67
179	11	3.00200	5.05230	2.03391	53.060	197.59	0.25863	0.24678	255.890	477.72
148	11	1.89930	7.07140	2.07852	169.67	317.22	0.31849	1.30696	1118.40	483.73
180	11	2.99900	6.95610	2.02096	53.345	199.01	0.27252	0.35733	352.410	478.54
147	11	1.89920	12.1210	2.09328	169.78	315.74	0.31526	2.24468	1920.90	479.94
183	11	2.99040	12.1850	2.03679	54.129	199.53	0.29093	0.67467	621.930	477.74

* TPN : Test Point Number, PN : Part Number

* Subscript ∞ = External Freestream Condition, n = Internal(Nozzle) Freestream Condition

Table B-2 Nozzle Cowl Effects

TPN	PN	M _∞	NPR	RE _∞ /A ^{1/2} T(10 ⁶)	P _∞	T _∞	M _n	RE _n	P _n	T _n
241	11	0.60283	2 01670	2 04746	1004.8	515.63	0.31411	2.12034	1892.50	494.46
268	12	0.60607	2.10690	2.17633	997.49	490.93	0.30863	2.31423	1967.38	469.71
319	13	0.60742	2.03140	2.05016	995.08	514.24	0.30306	2.14217	1896.60	477.92
346	14	0.60453	2.00650	2.04937	1000.4	514.62	0.31010	2.10387	1877.90	489.57
255	11	0.80167	3.09050	2.02502	702.99	491.64	0.29427	2.26345	2045.80	474.69
288	12	0.80072	3.02780	2.03200	701.96	489.32	0.31179	2.21525	1986.90	493.49
314	13	0.80325	3.07630	2.07852	701.87	489.23	0.30585	2.24770	2023.50	487.58
148	11	1.89930	7.07140	2.00984	169.67	317.22	0.31849	1.30696	1118.40	483.73
160	12	1.90260	7.15970	2.02311	168.58	323.92	0.29892	1.25155	1134.50	481.56
172	13	1.90490	7.03620	2.04299	169.07	323.34	0.30376	1.25028	1115.80	481.73
116	14	1.88940	7.05150	2.03757	172.83	324.29	0.24849	1.08873	1167.40	475.34
184	11	2.98640	15.9730	1.99574	54.430	200.04	0.29333	0.89706	819.010	477.22
212	12	3.01690	15.9950	2.01766	51.760	197.47	0.32293	0.93704	770.190	473.94
199	13	3.00910	15.9590	2.09328	52.512	197.59	0.29833	0.88606	787.850	473.71

Table B-3 NPR Effects

TPN	PN	M _u	NPR	RE _u /T(10 ⁶)	P _u	T _u	M _n	RE _n	P _n	T _n
240	11	0.60196	0.90310	2.05019	1001.8	513.31	0.31000	0.89962	846.370	509.91
241	11	0.60283	2.01670	2.04746	1004.8	515.63	0.31411	2.12034	1892.50	494.46
242	11	0.60313	3.08510	2.05107	1004.9	515.16	0.31037	3.30618	2899.80	483.29
243	11	0.60024	4.02490	2.02547	1005.3	518.46	0.30980	4.55896	3785.9	462.67
244	11	0.60090	4.89080	2.02823	1002.1	517.06	0.31070	5.83063	4583.80	444.63
254	11	0.80365	2.09010	2.02789	701.46	491.21	0.29022	1.46689	1382.9	485.19
255	11	0.80167	3.09050	2.02502	702.99	491.64	0.29427	2.26345	2045.80	474.69
256	11	0.80158	4.03600	2.02792	703.43	491.29	0.29701	3.04909	2670.5	466.63
257	11	0.80367	5.07300	2.03180	702.72	491.17	0.29865	3.96144	3351.00	456.25
258	11	0.80571	6.05900	2.02965	699.63	490.86	0.29895	4.80465	3984.20	449.69
151	11	1.89870	0.96161	2.03139	170.60	323.73	0.26701	0.15287	156.120	483.92
150	11	1.89880	2.98720	2.04680	170.31	321.58	0.31067	0.54214	475.840	483.92
149	11	1.89900	4.99910	2.04307	169.61	321.07	0.31782	0.91714	790.550	485.67
148	11	1.89930	7.07140	2.07852	169.67	317.22	0.31849	1.30696	1118.40	483.73
147	11	1.89920	12.1210	2.09328	169.78	315.74	0.31526	2.24468	1920.90	479.94
179	11	3.00200	5.05230	2.03391	53.060	197.59	0.25863	0.24678	255.890	477.72
180	11	2.99900	6.95610	2.02096	53.345	199.01	0.27252	0.35733	352.410	478.54
181	11	2.99480	8.99580	2.00542	53.717	200.78	0.28331	0.47941	457.030	480.35

APPENDIX C: PRESSURE CONTOUR

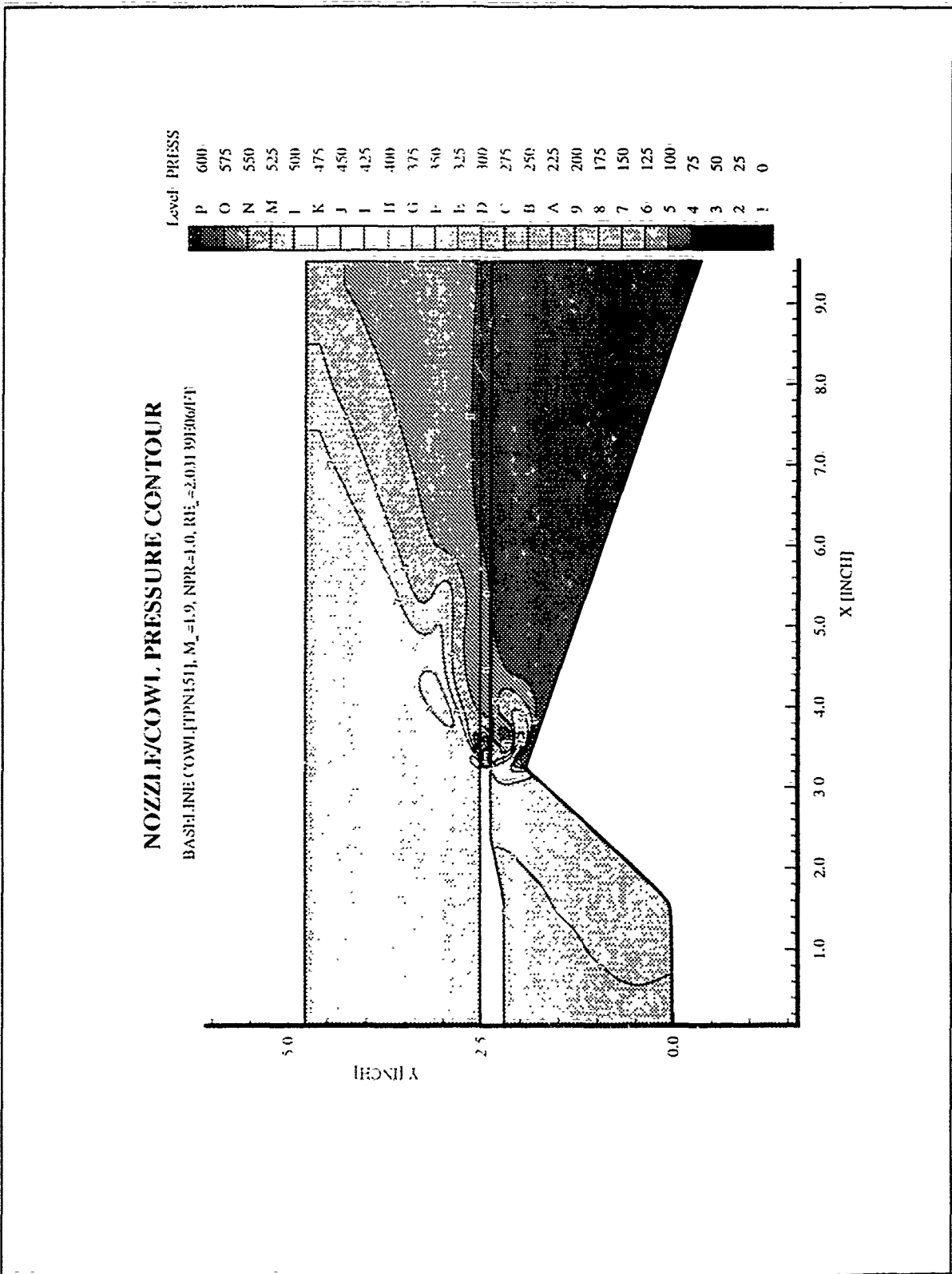


Figure C-1 Nozzle/Afterbody Pressure Contour: Baseline Cowl, $M_\infty=1.9$, NPR=1.0

NOZZLE/COWL PRESSURE CONTOUR

BASELINE COWL (TPN177), $M_\infty=3.0$, NPR=1.0; $RE_\infty=1.9989E6/FT$

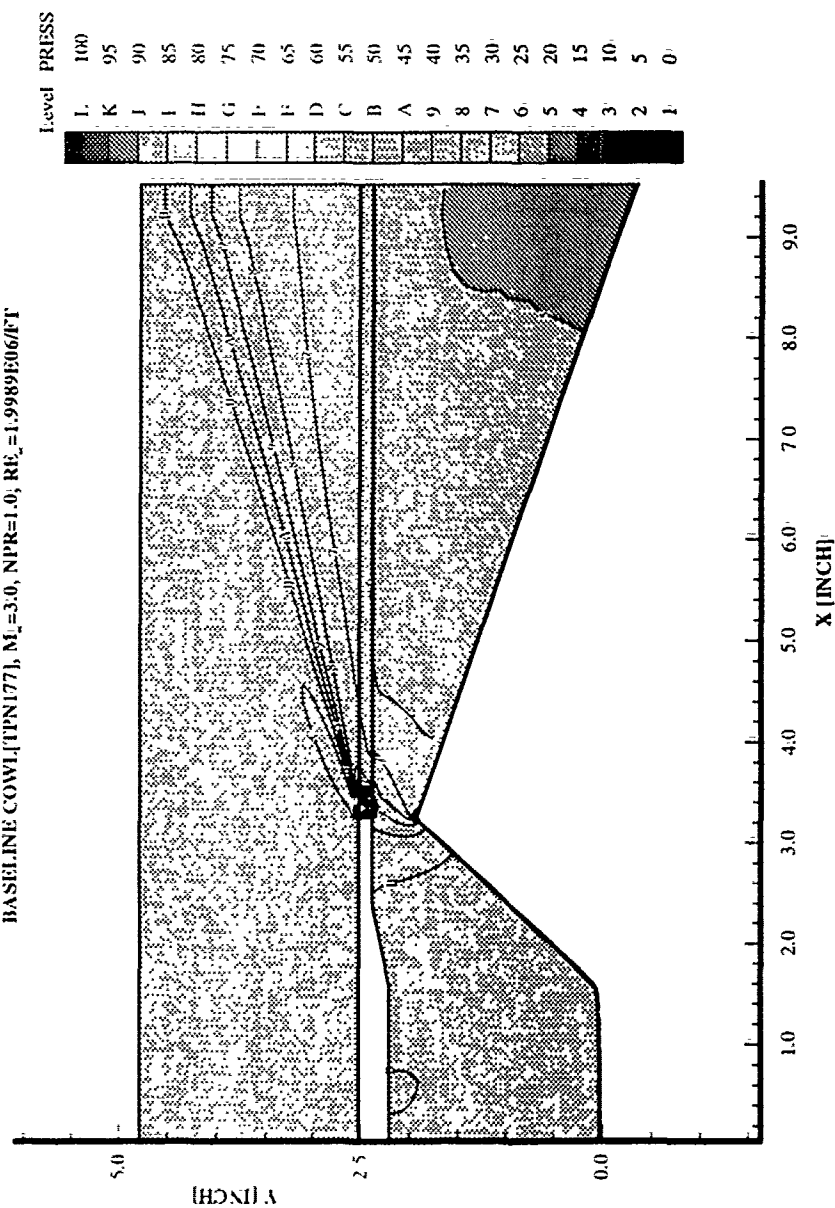


Figure C-2 Nozzle/Afterbody Pressure Contour: Baseline Cowl, $M_\infty=3.0$, NPR=1.0

NOZZLE/COWL PRESSURE CONTOUR

BASIS LINE COWL, [TPN150], $M_\infty=1.9$, NPR=3.0, $Re_\infty=2.04681 \times 10^6$

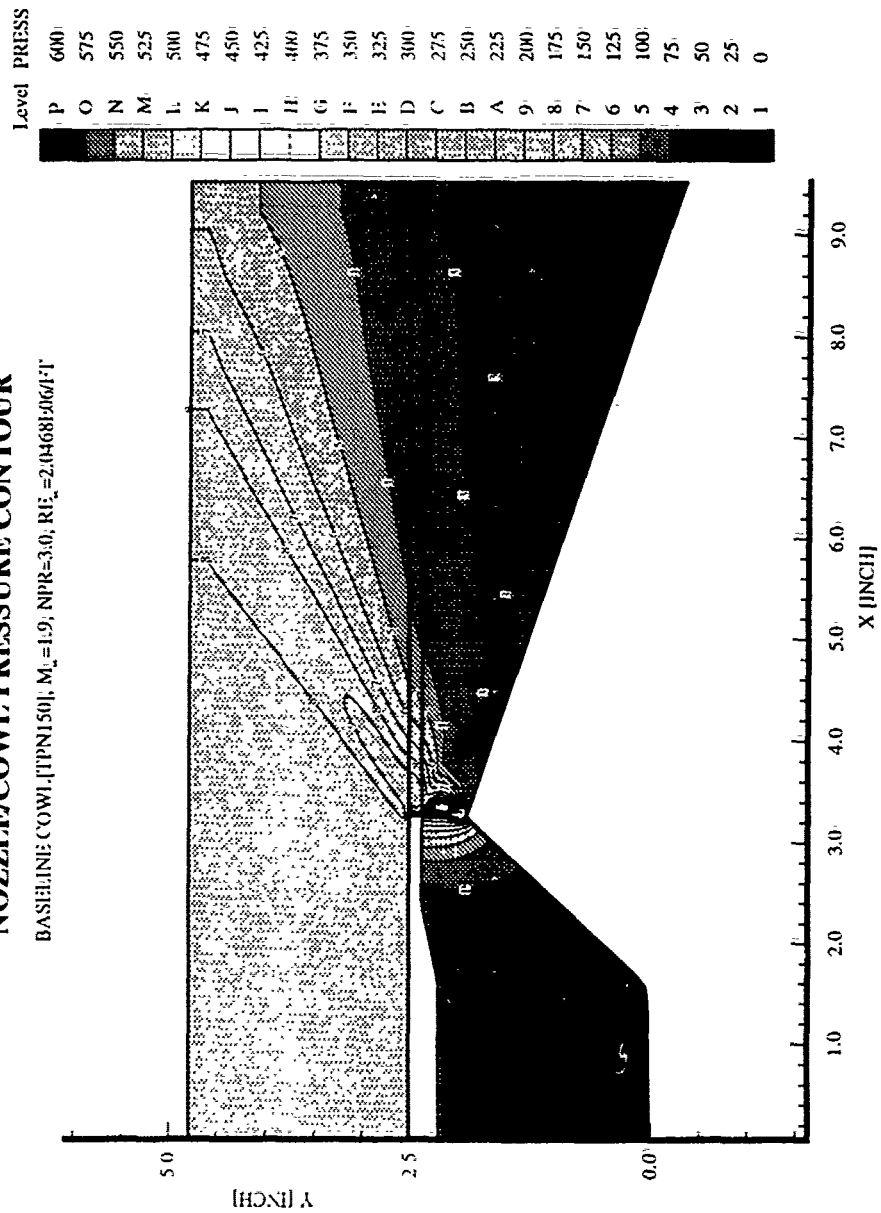


Figure C-3 Nozzle/Afterbody Pressure Contour: Baseline Cowl, $M_\infty=1.9$, NPR=3.0

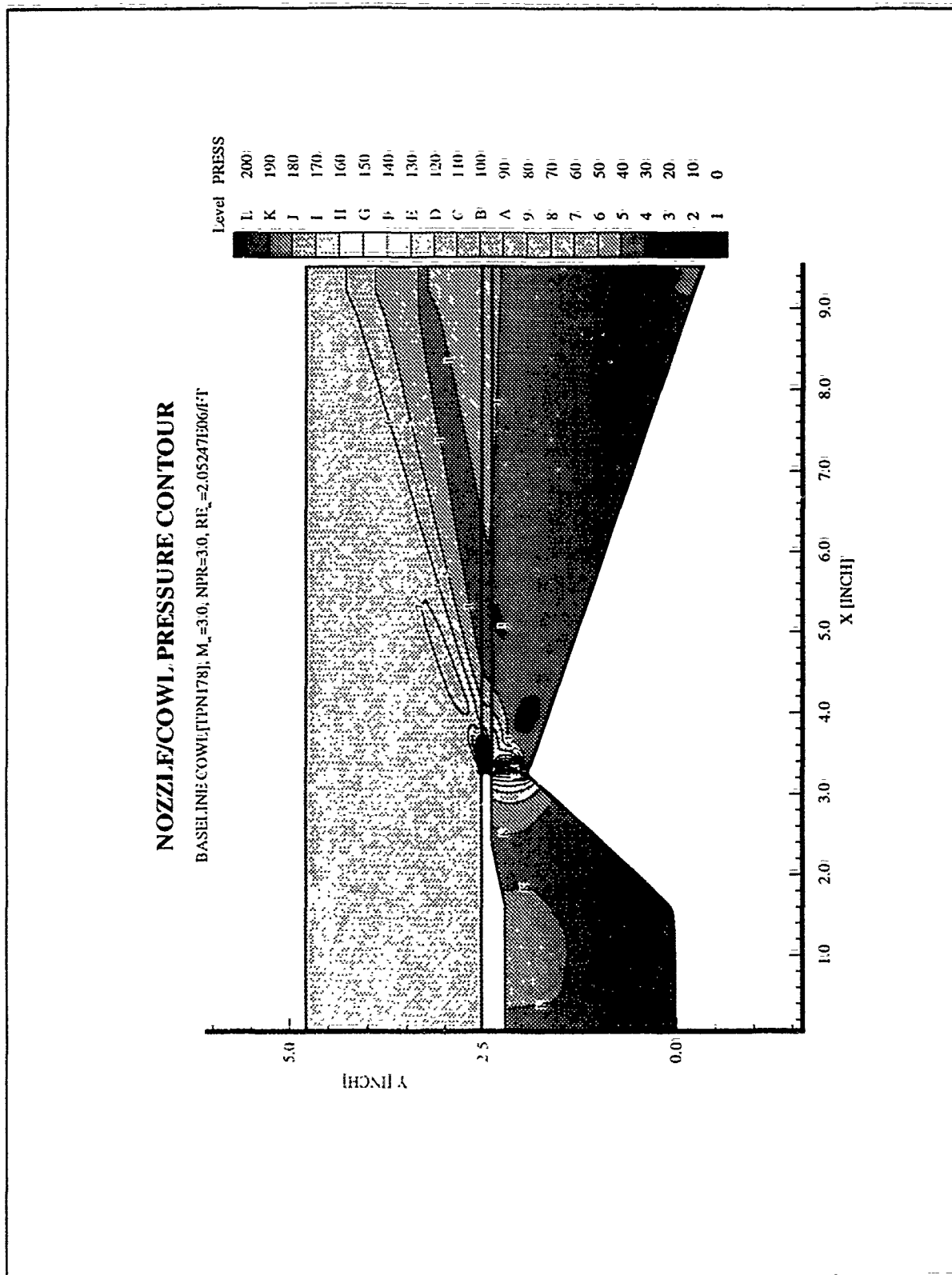


Figure C-4 Nozzle/Afterbody Pressure Contour: Baseline Cowl, $M_\infty=3.0$, NPR=3.0

NOZZLE/COWL PRESSURE CONTOUR

BASILINE COWL, [TPN149], $M_\infty=1.9$, NPR=5.0, $Re_\infty=2.04307E06/l-ft$

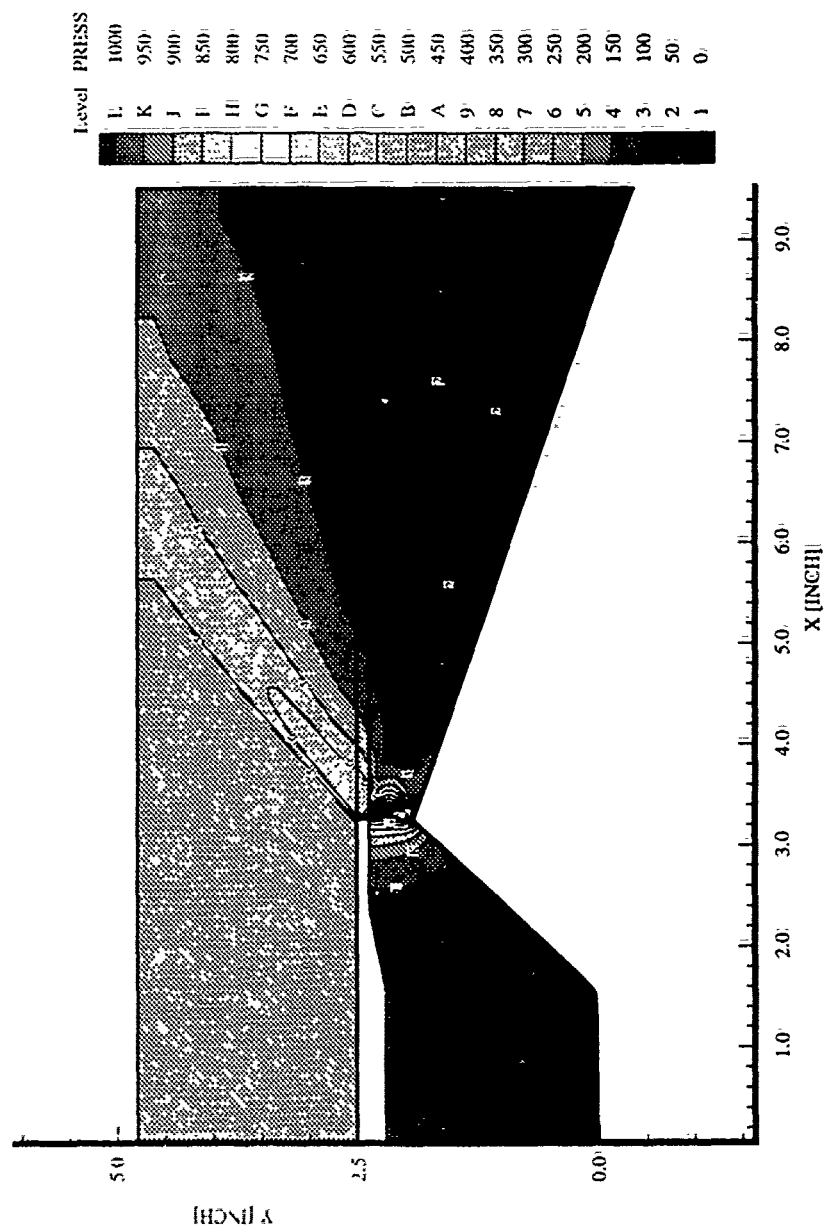


Figure C-5 Nozzle/Afterbody Pressure Contour: Baseline Cowl, $M_\infty=1.9$, NPR=5.0

NOZZLE/COWL PRESSURE CONTOUR

BASIS LINE COWL [TPN170], $M_\infty = 3.0$, NPR=5.0, $Re_\infty = 2.03191 \times 10^6$

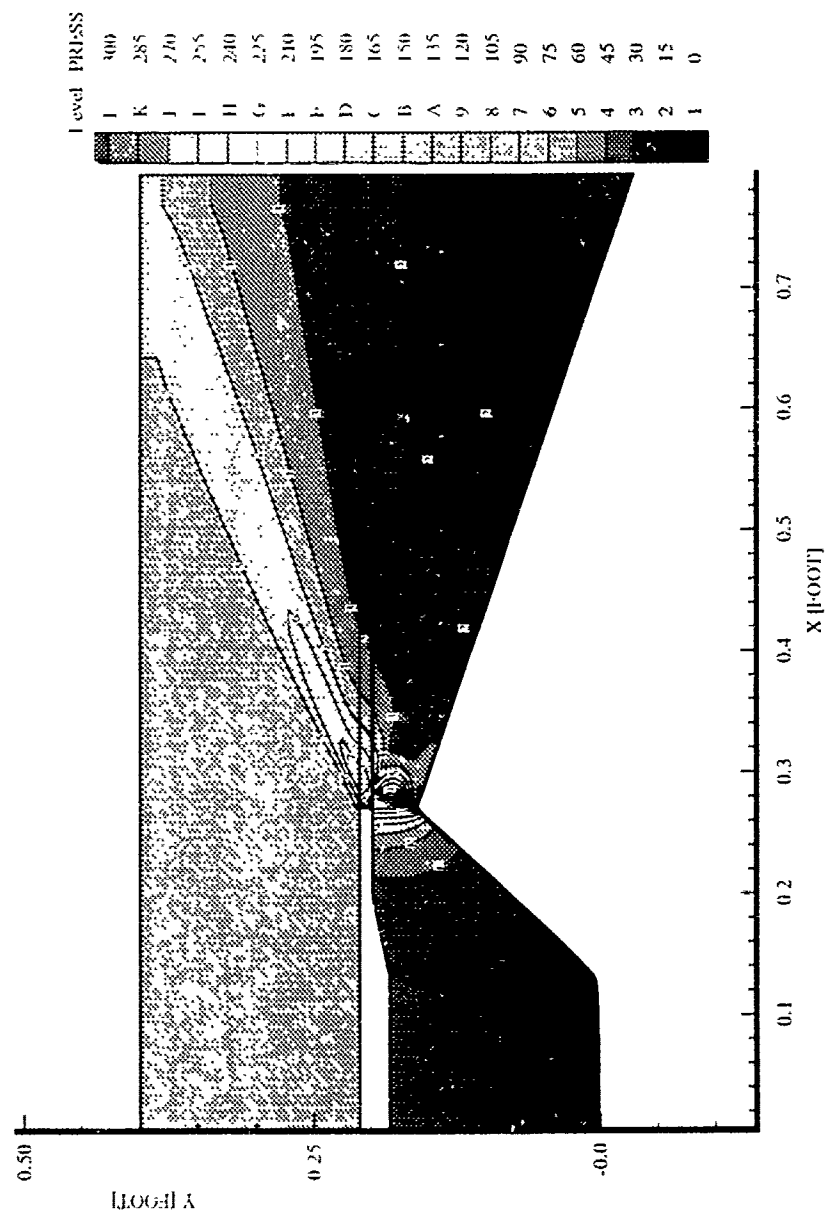


Figure C-6 Nozzle/Afterbody Pressure Contour. Baseline Cowl, $M_\infty=3.0$, NPR=5.0

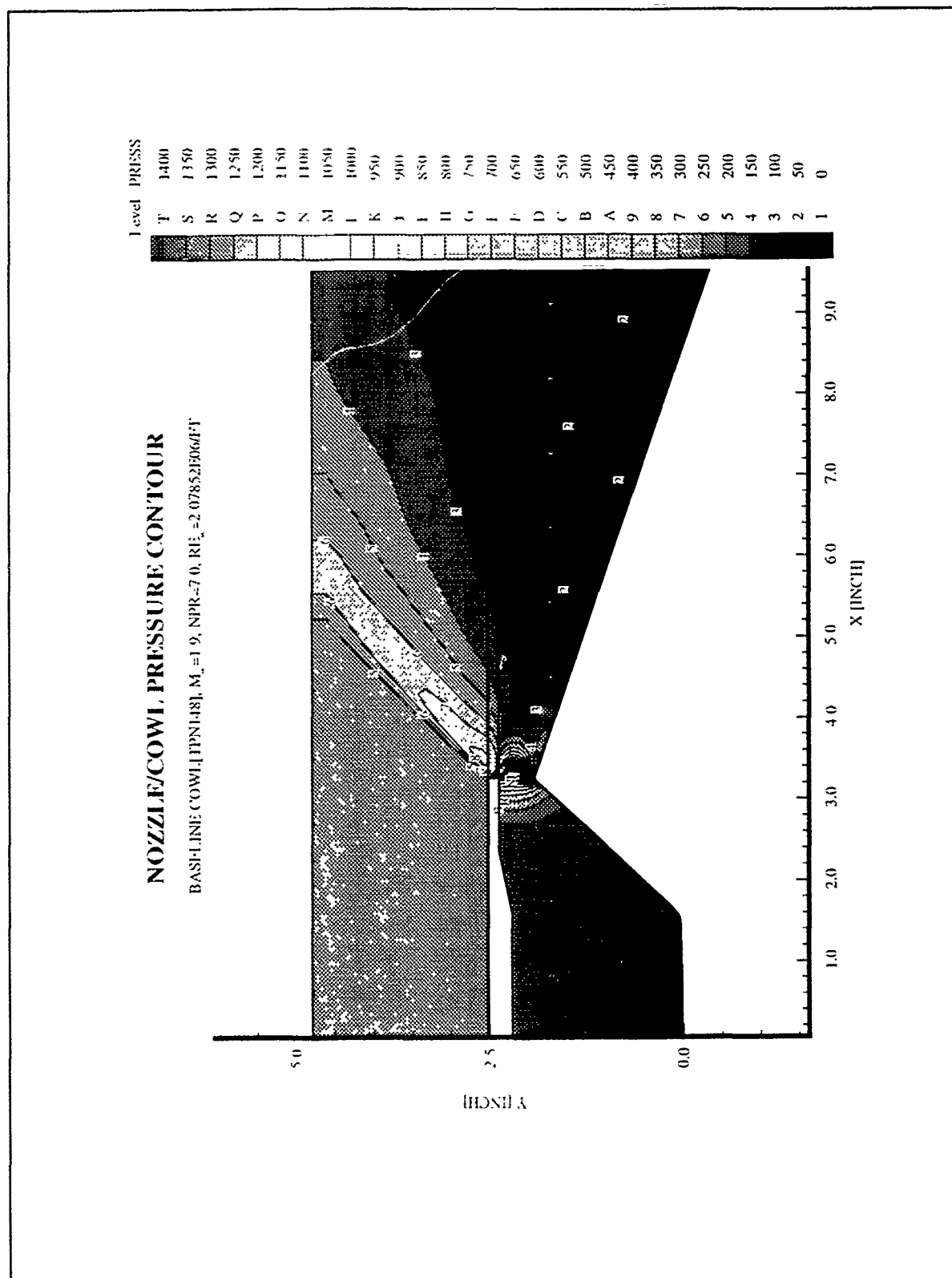


Figure C-7 Nozzle/Afterbody Pressure Contour Baseline Cowl, $M_\infty=1.9$, $NPR=7.0$

NOZZLE/COWL PRESSURE CONTOUR

BASILINE COWL, $M_\infty=3.0$, NPR=7.0, $Re_\infty=2.02096106 \times 10^6$

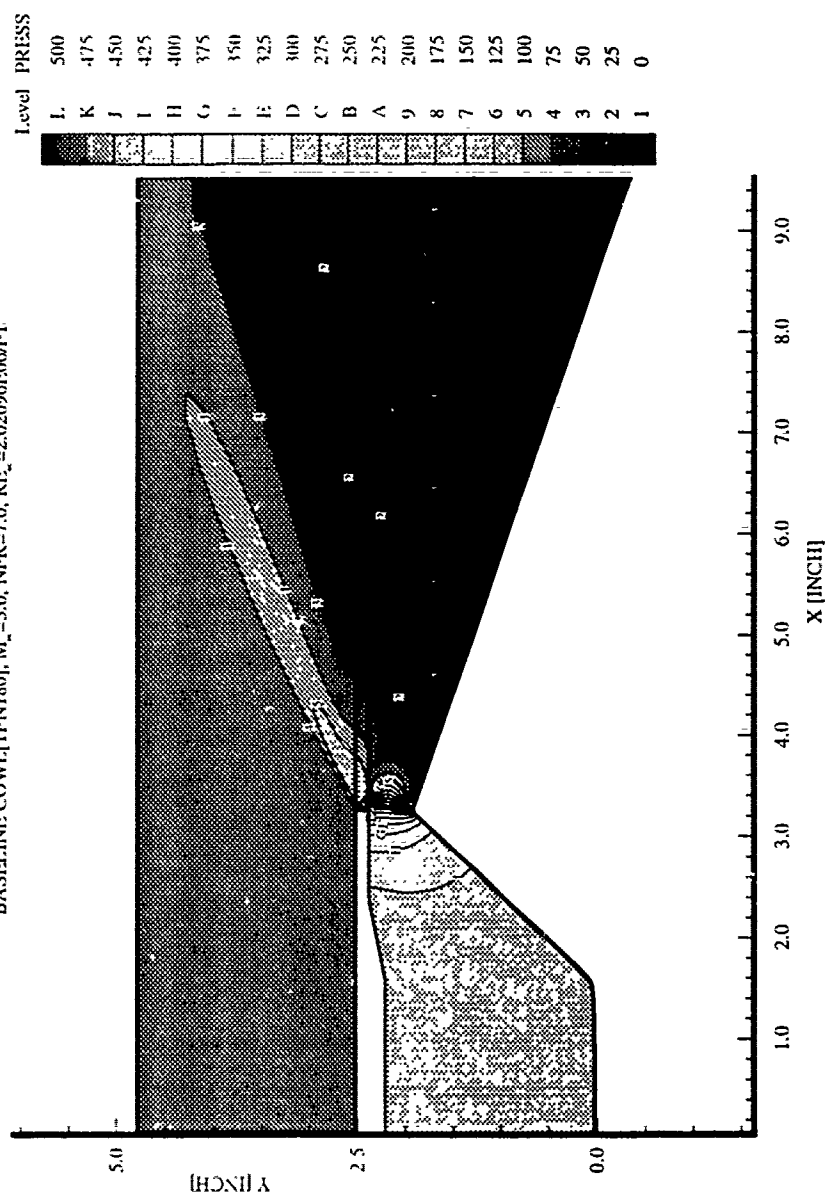


Figure C-8 Nozzle/Afterbody Pressure Contour: Baseline Cowl, $M_\infty=3.0$, NPR=7.0

NOZZLE/COWL PRESSURE CONTOUR

BASILINE COWL, $M_\infty=1.9$, $NPR=12.0$, $Re_\infty=2.09328E06$ ft

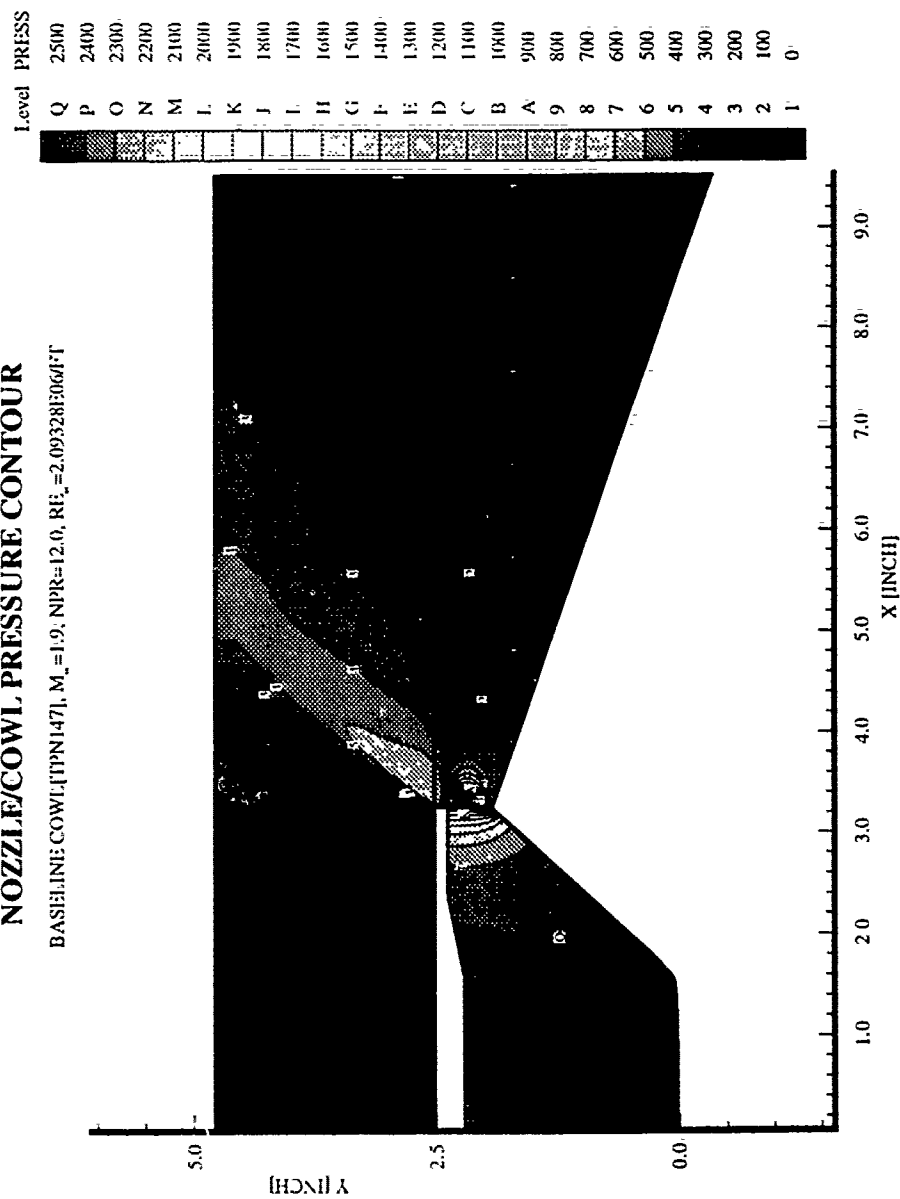


Figure C-9 Nozzle/Afterbody Pressure Contour: Baseline Cowl, $M_\infty=1.9$, $NPR=12.0$

NOZZLE/COWL PRESSURE CONTOUR

BASELINE COWL, [TPN183], $M_\infty=3.0$, NPR=12.0, $Re_\infty=2.03679 \times 10^6/\text{ft}$

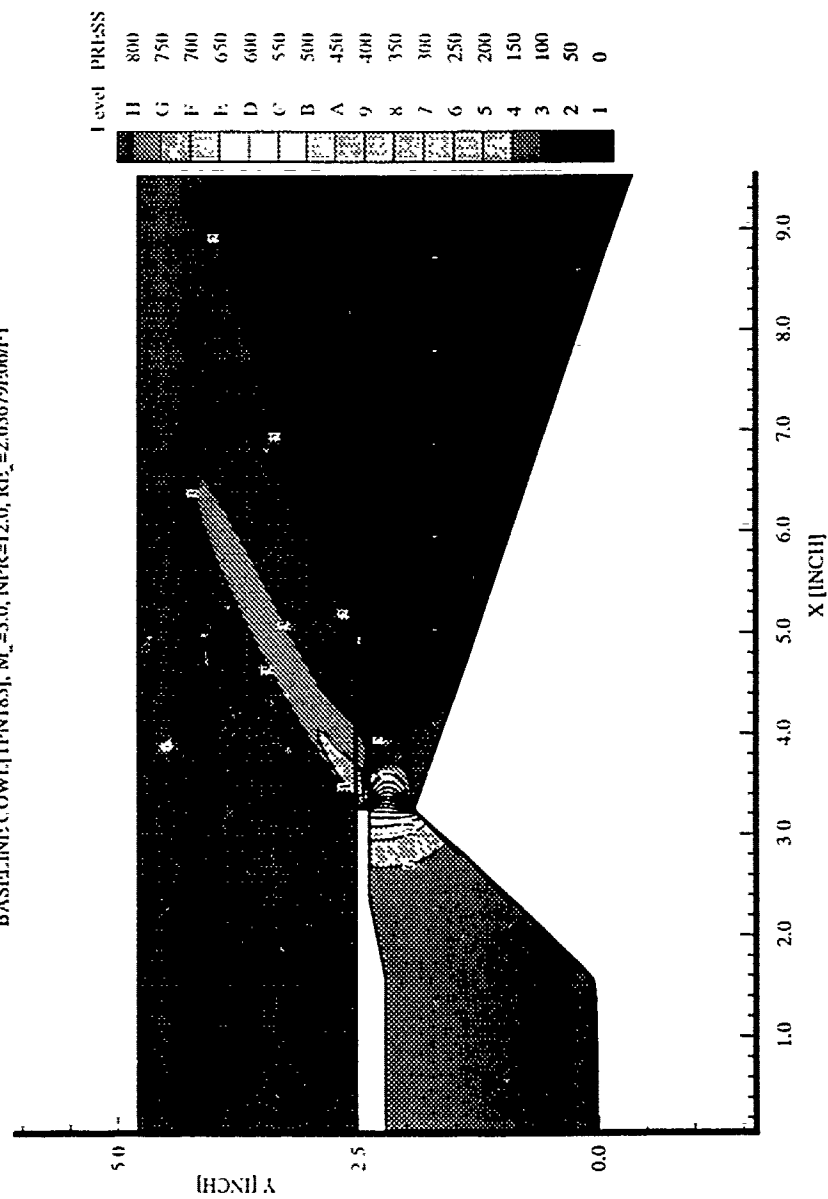


Figure C-10 Nozzle/Afterbody Pressure Contour. Baseline Cowl, $M_\infty=3.0$, NPR=12.0

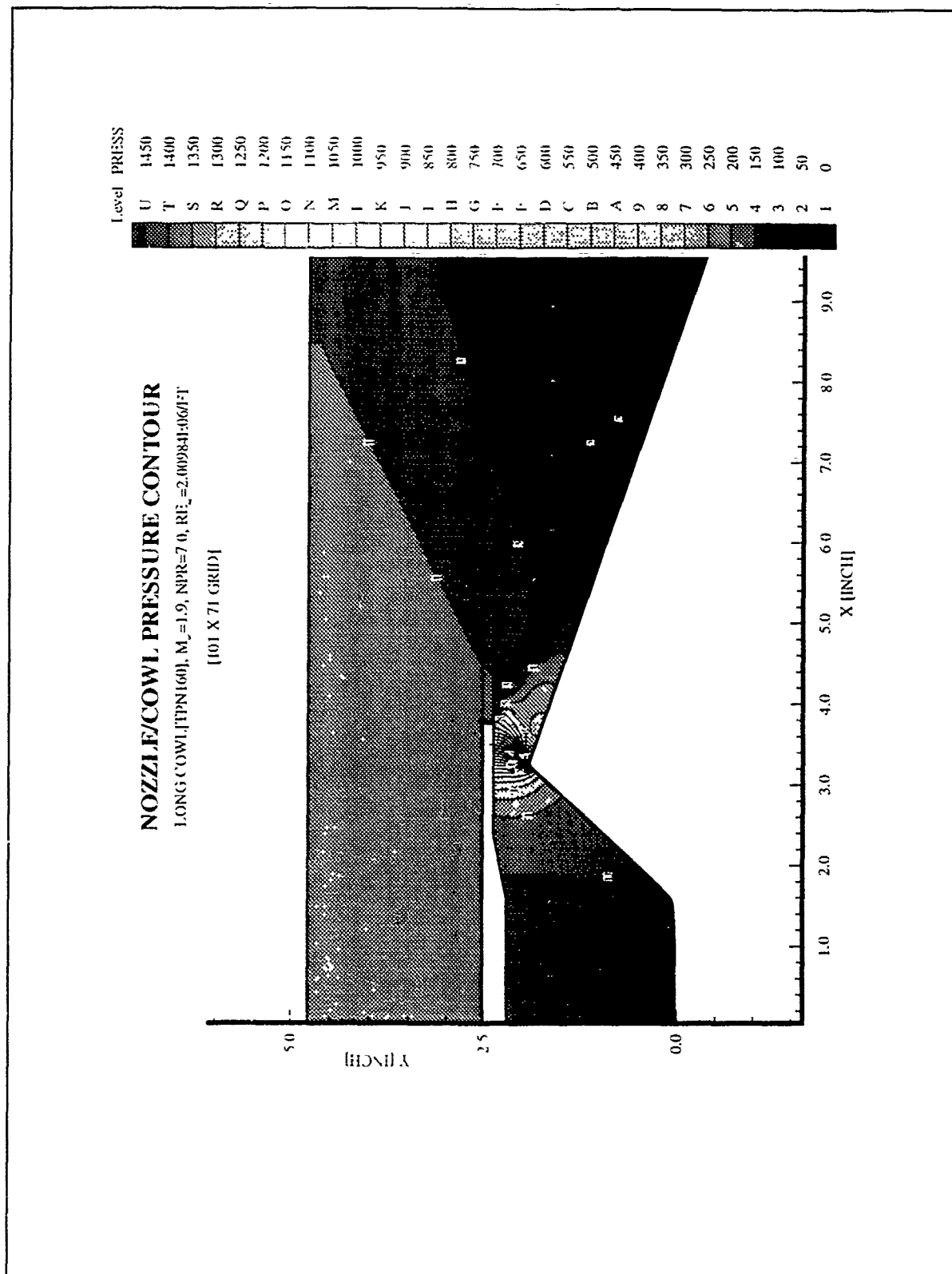


Figure C-11 Nozzle/Afterbody Pressure Contour: Long Cowl, $M_\infty=1.9$, NPR=7.0

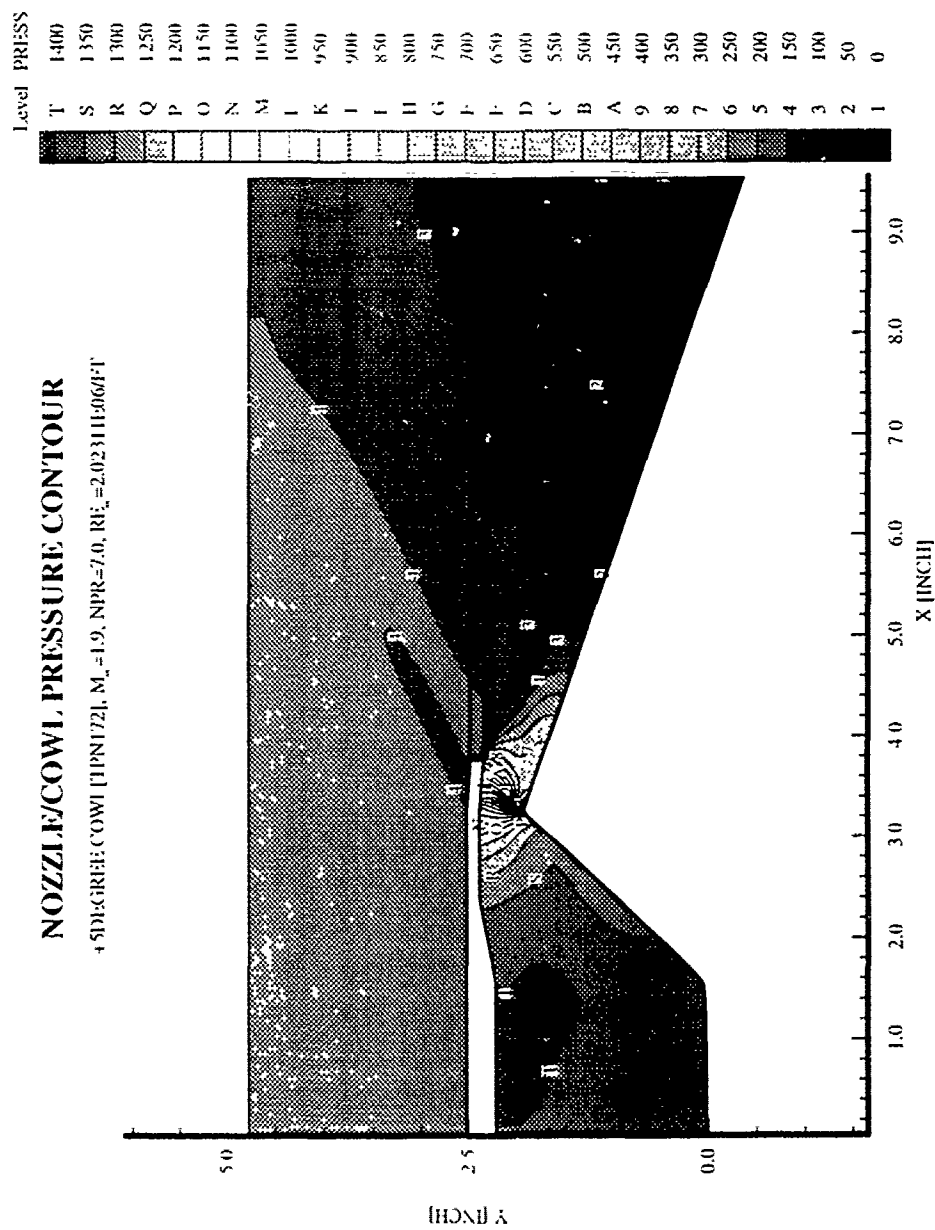


Figure C-12 Nozzle/Afterbody Pressure Contour +5 Degree Cowl, $M_\infty=1.9$, NPR=7.0

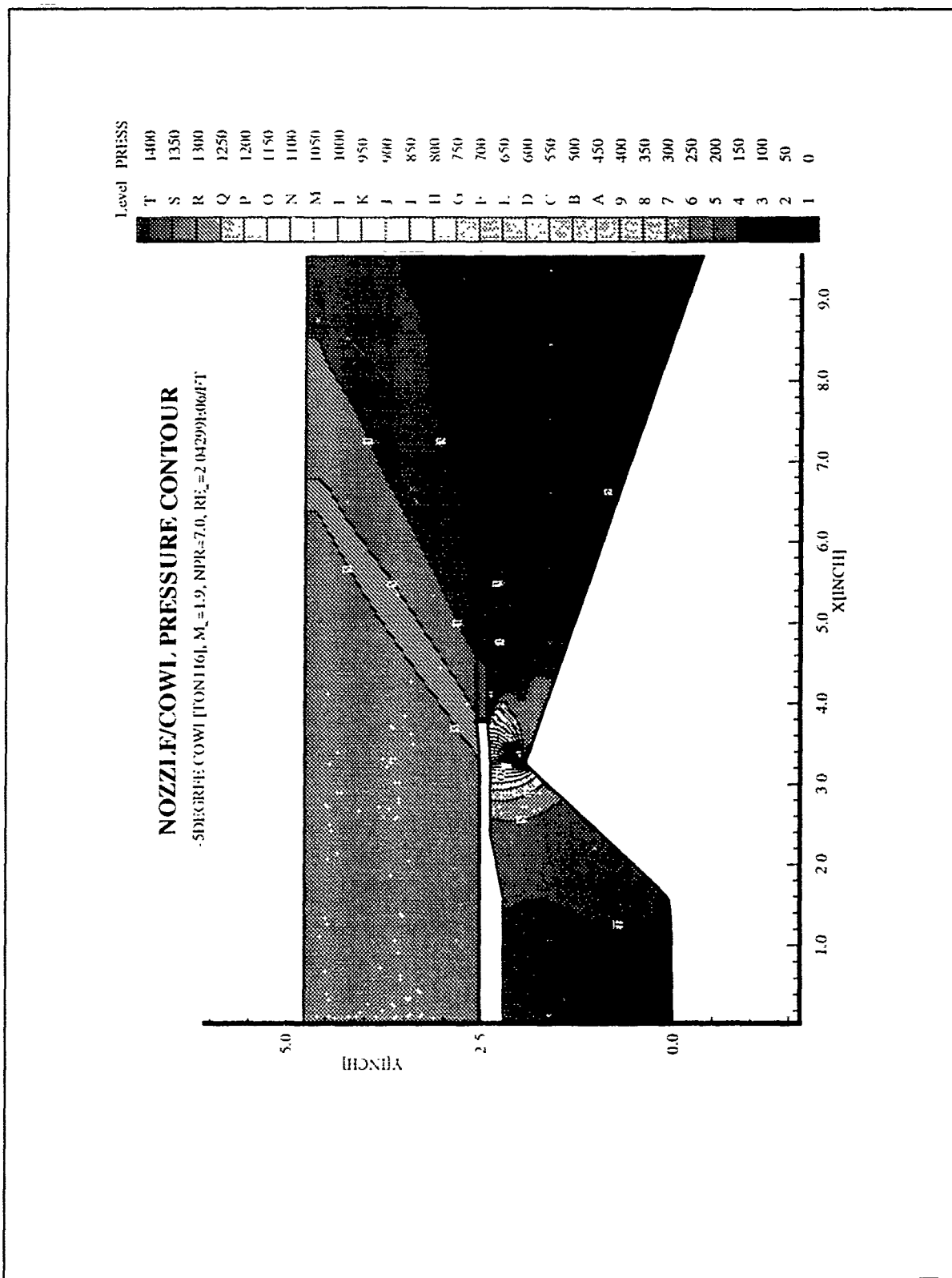


Figure C-13 Nozzle/Afterbody Pressure Contour: -5 Degree Cowl, $M_\infty = 1.9$, $NPR = 7.0$

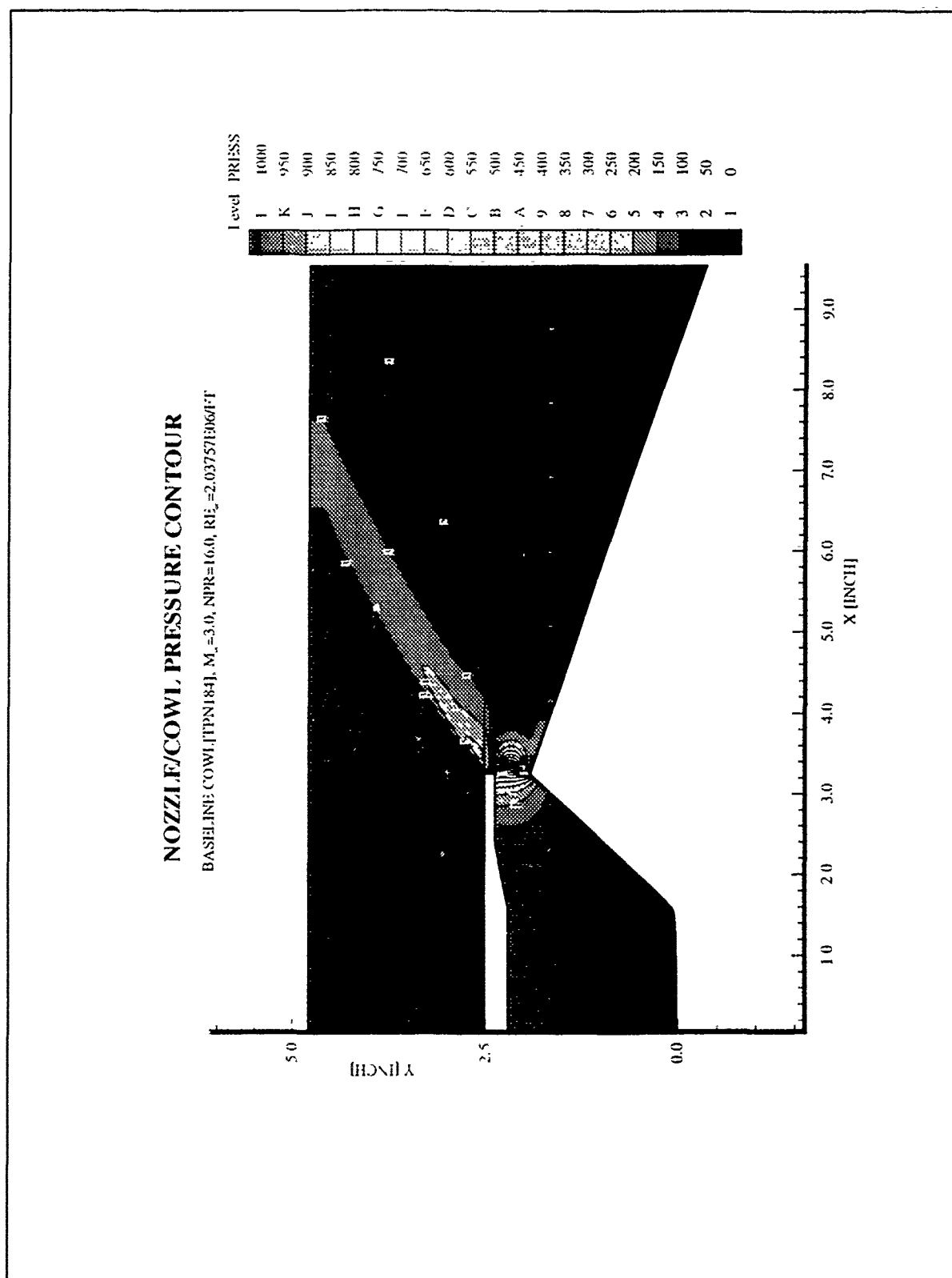


Figure C-14 Nozzle/Afterbody Pressure Contour. Baseline Cowl, $M_\infty=3.0$, NPR=16.0

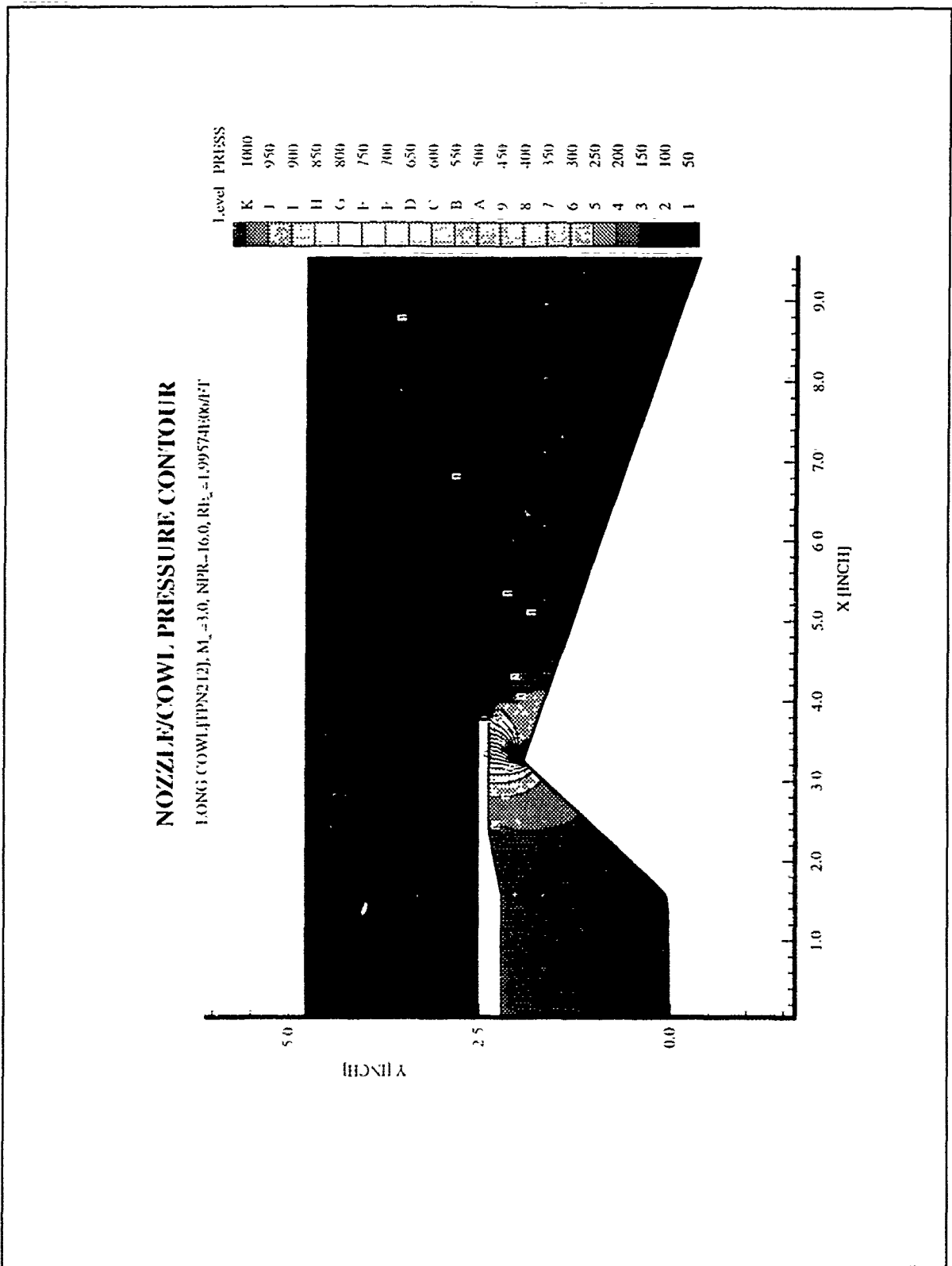


Figure C-15 Nozzle/Afterbody Pressure Contour: Long Cowl, $M_\infty=3.0$, NPR=16.0

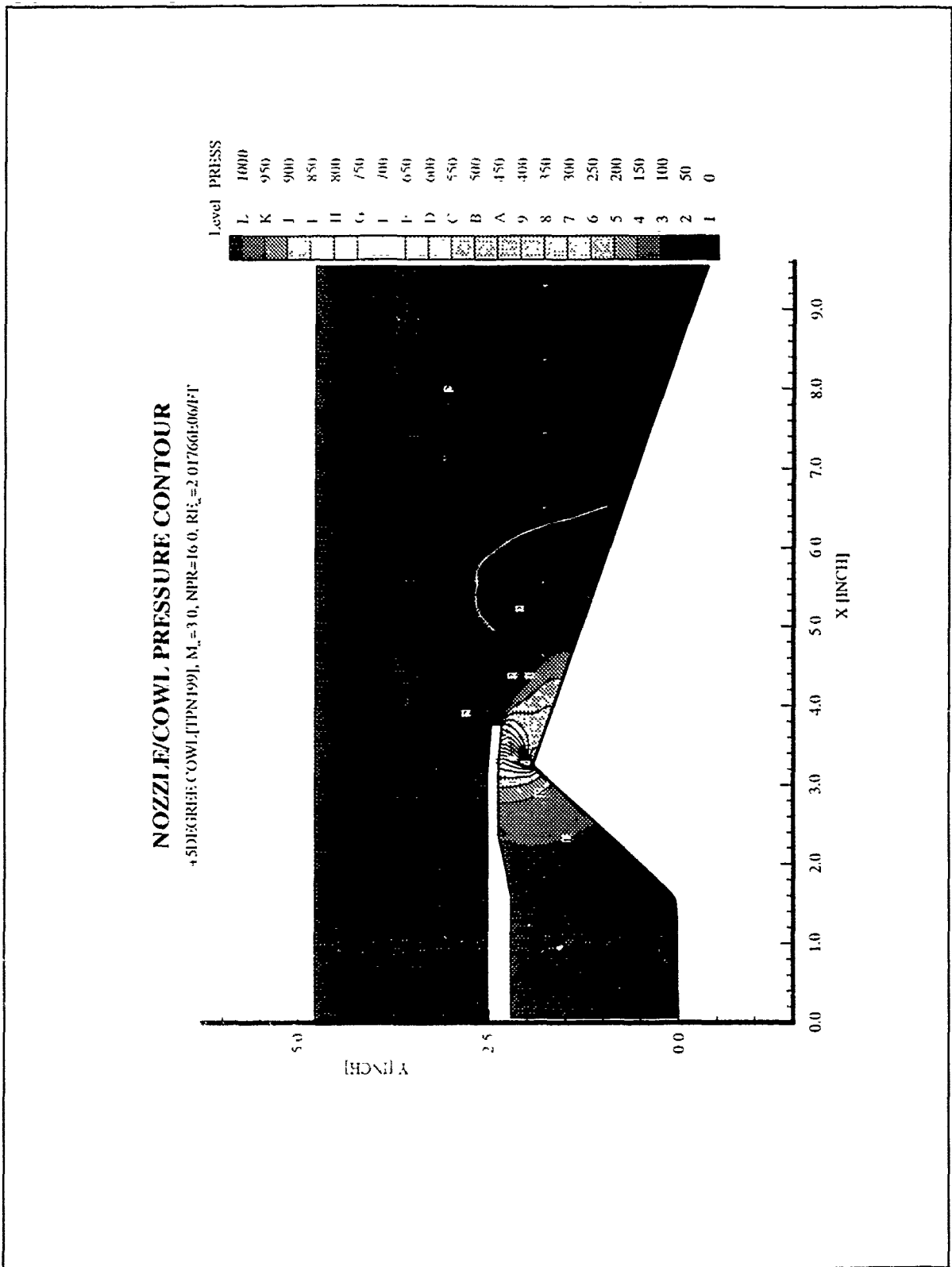


Figure C-16 Nozzle/Afterbody Pressure Contour. +5 Degree Cowl, $M_\infty=3.0$, NPR=16.0

APPENDIX D: MACH NUMBER CONTOUR

NOZZLE/COWL MACH NUMBER CONTOUR

BASILINE COWL [TPN151], $M_\infty = 1.9$, NPR=1.0, $Re_\infty = 2.03139E6/ft$

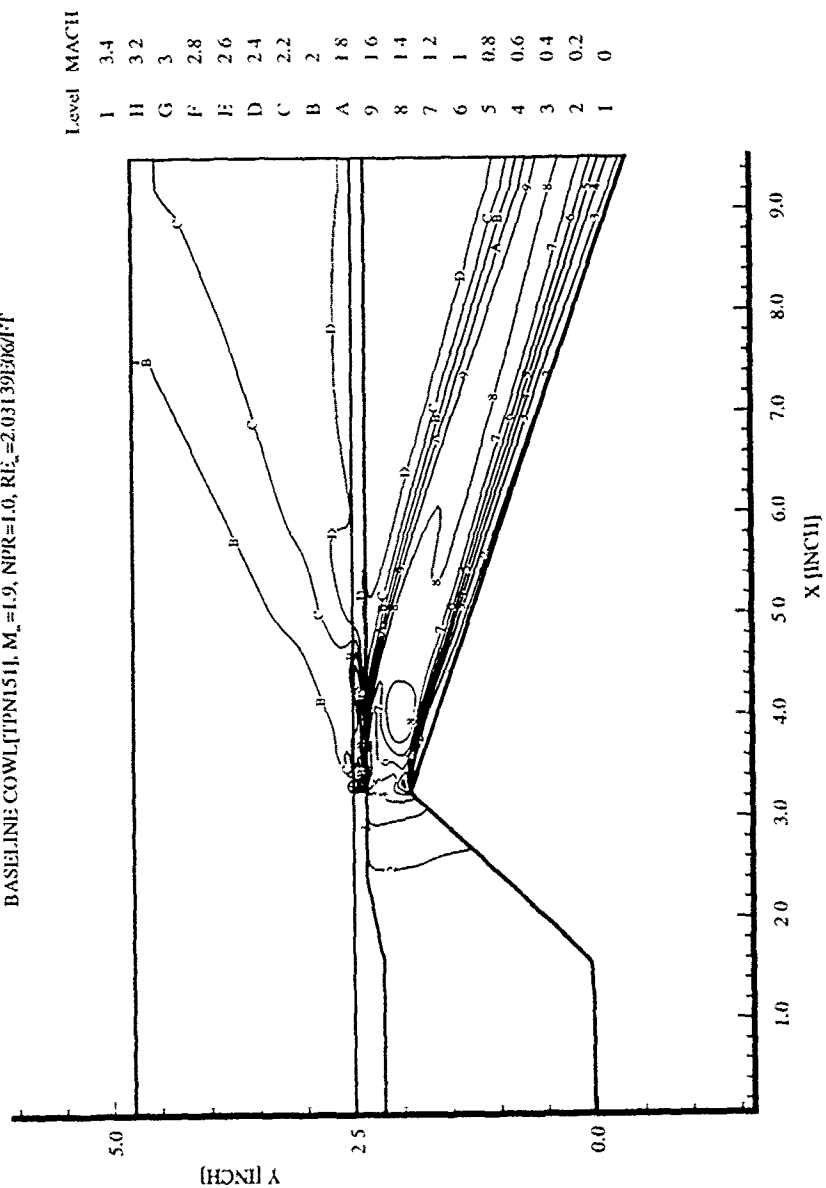


Figure D-1 Nozzle/Afterbody Mach Number Contour: Baseline Cowl, $M_\infty=1.9$, NPR=1.0

NOZZLE/COWL MACH NUMBER CONTOUR

BASELINE COWL [TPN177], $M_\infty=3.0$, NPR=1.0, $Re_\infty=1.9989E06/ft$

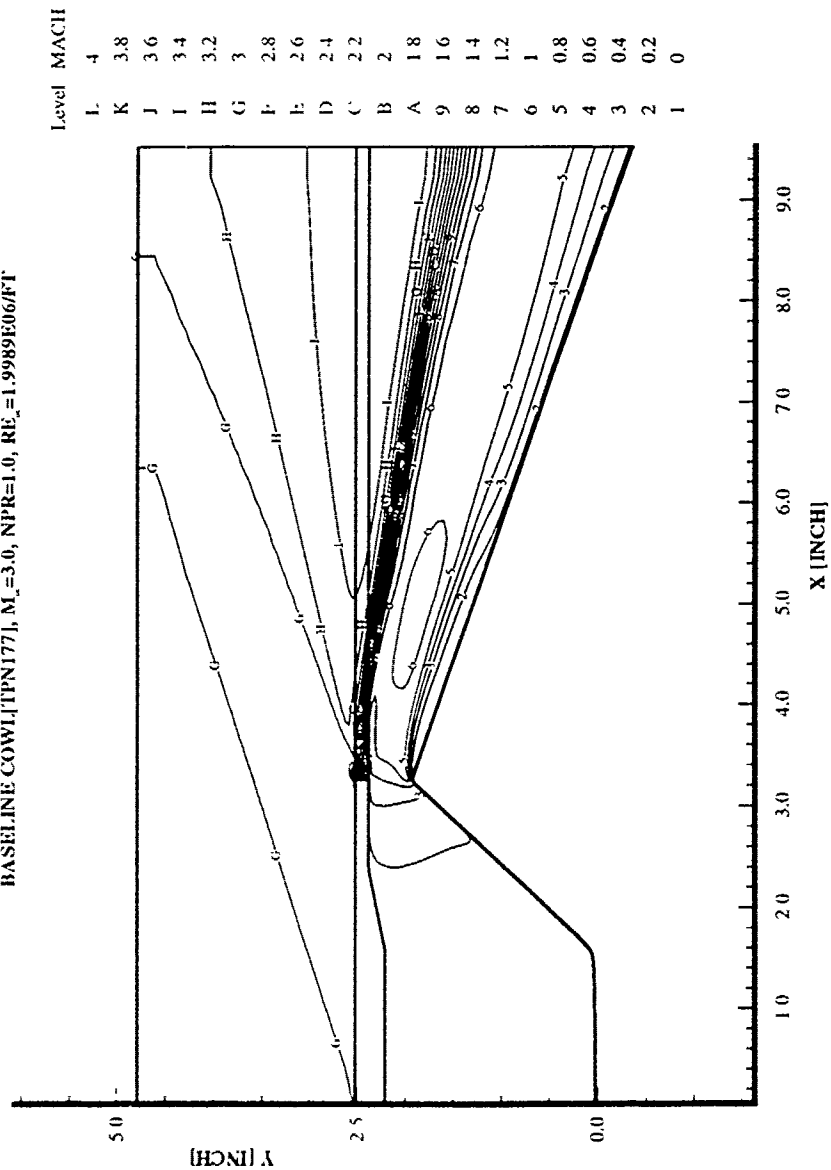


Figure D-2 Nozzle/Afterbody Mach Number Contour: Baseline Cowl, $M_\infty=3.0$, NPR=1.0

NOZZLE/COWL, MACH NUMBER CONTOUR

BASELINE COWL, JTPN1501, $M_\infty = 1.9$, NPR=3.0, $Re_\infty = 2.0468E6/ft$

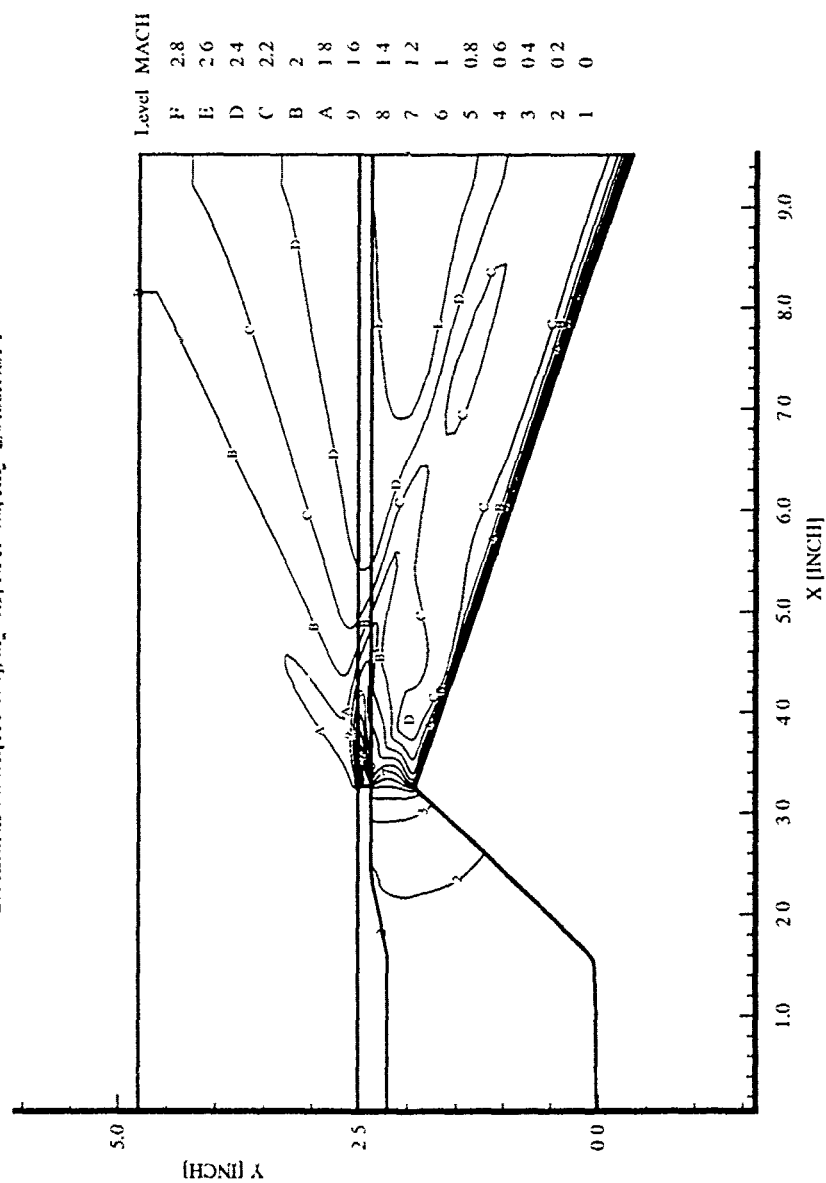


Figure D-3 Nozzle/Afterbody Mach Number Contour: Baseline Cowl, $M_\infty = 1.9$, NPR=3.0

NOZZLE/COWL, MACH NUMBER CONTOUR

BASILINE COWL, [TPN178], $M_\infty=3.0$, $NPR=3.0$, $Re_\infty=2.05247 \times 10^6$

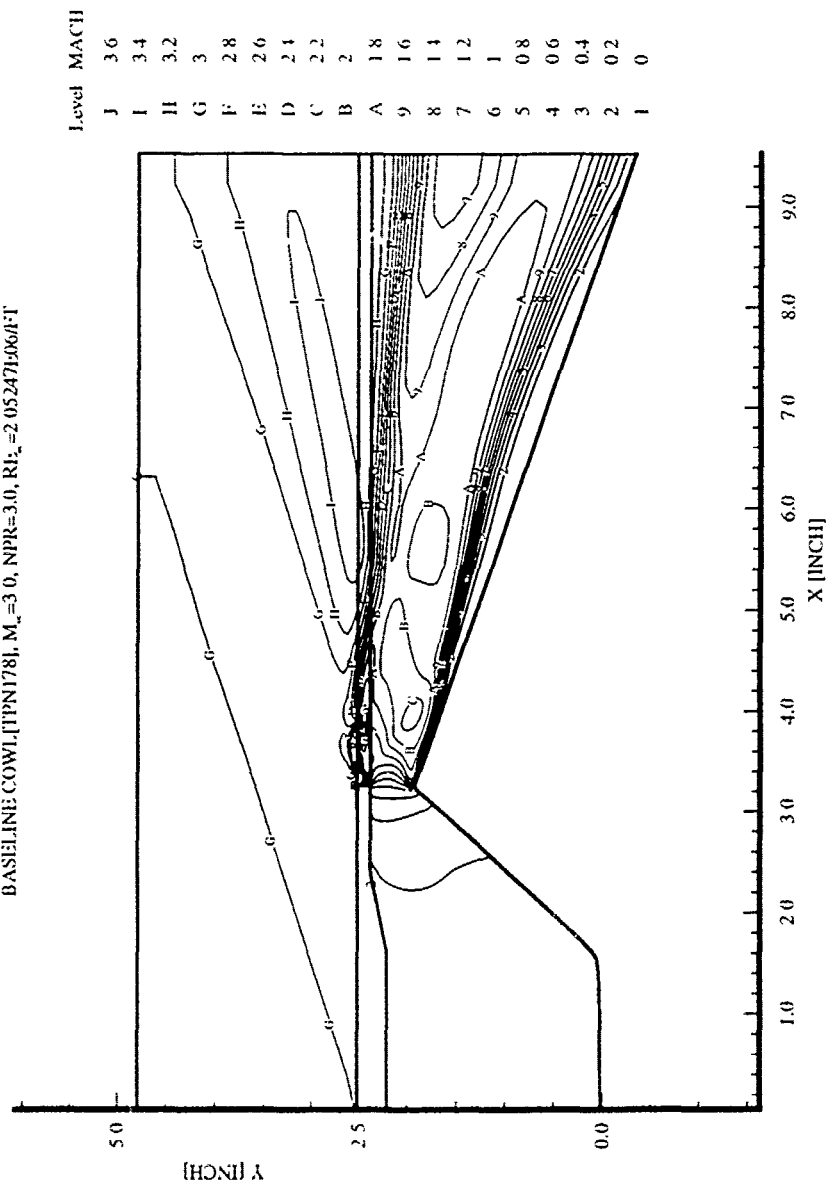


Figure D-4 Nozzle/Afterbody Mach Number Contour: Baseline Cowl, $M_\infty=3.0$, $NPR=3.0$

NOZZLE/COWL MACH NUMBER CONTOUR

BASIS IN: COWL [TPN149], $M_\infty = 1.9$, NPR=5.0, $Re_\infty = 2.04307 \times 10^6 / ft$

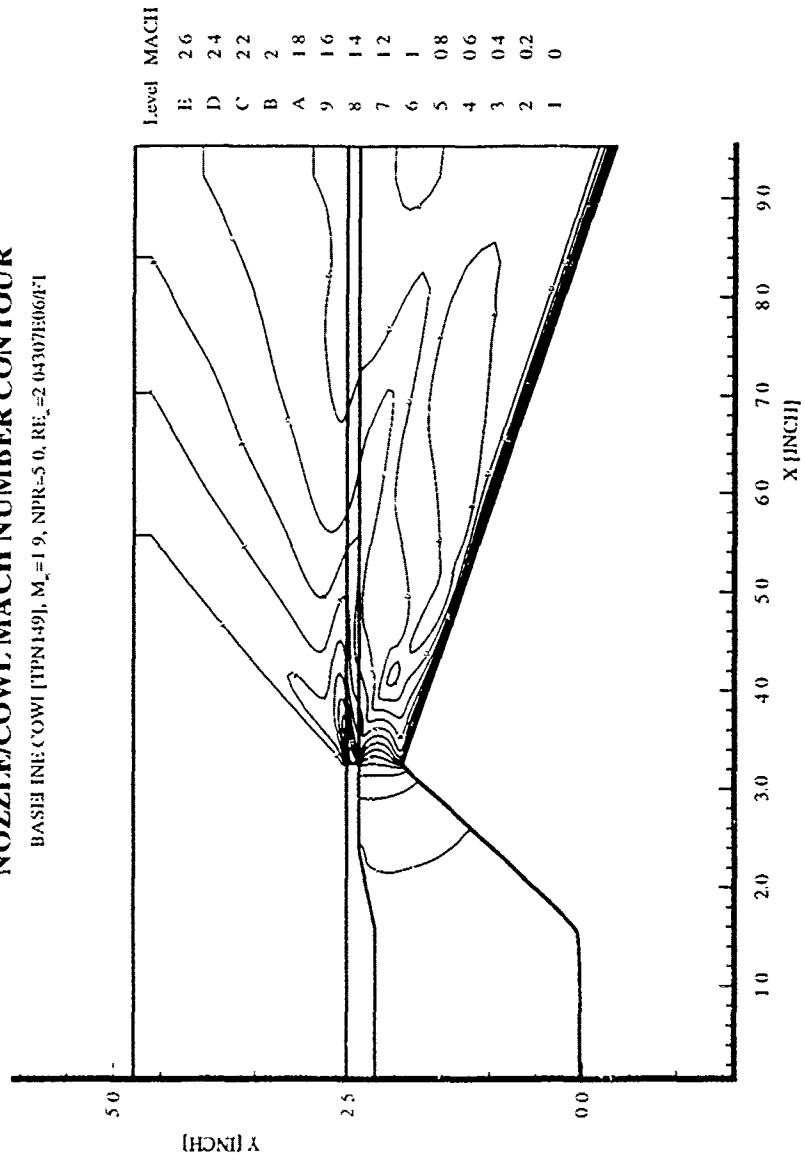


Figure D-5 Nozzle/Afterbody Mach Number Contour: Baseline Cowl, $M_\infty = 1.9$, NPR=5.0

NOZZLE/COWL MACH NUMBER CONTOUR

BASELINE COWL [TPN179], $M_\infty=3.0$, NPR=5.0, $RE_\infty=2.03911 \times 10^6/ft$

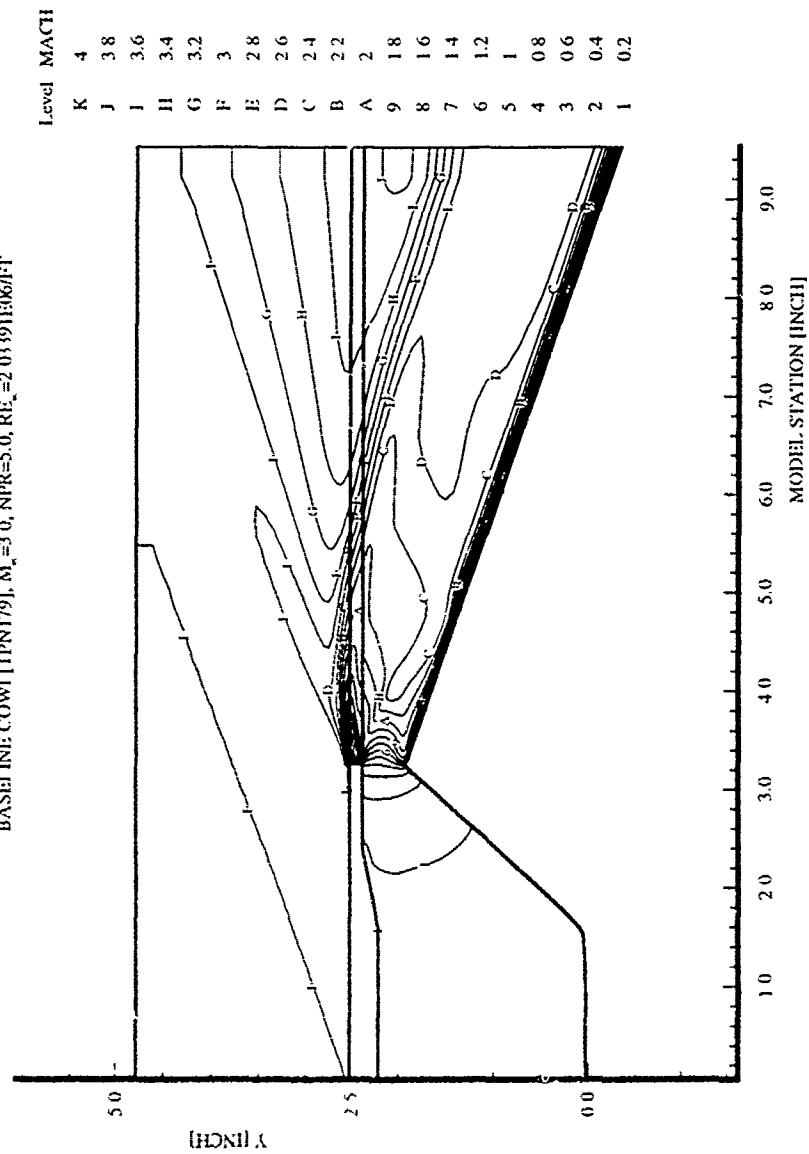


Figure D-6 Nozzle/Afterbody Mach Number Contour: Baseline Cowl, $M_\infty=3.0$, NPR=5.0

NOZZLE/COWL MACH NUMBER CONTOUR

BASIS LINE: COWL [TPN148], $M_\infty = 1.9$, NPR=7.0, $Re_\infty = 2.07852E+06/ft$

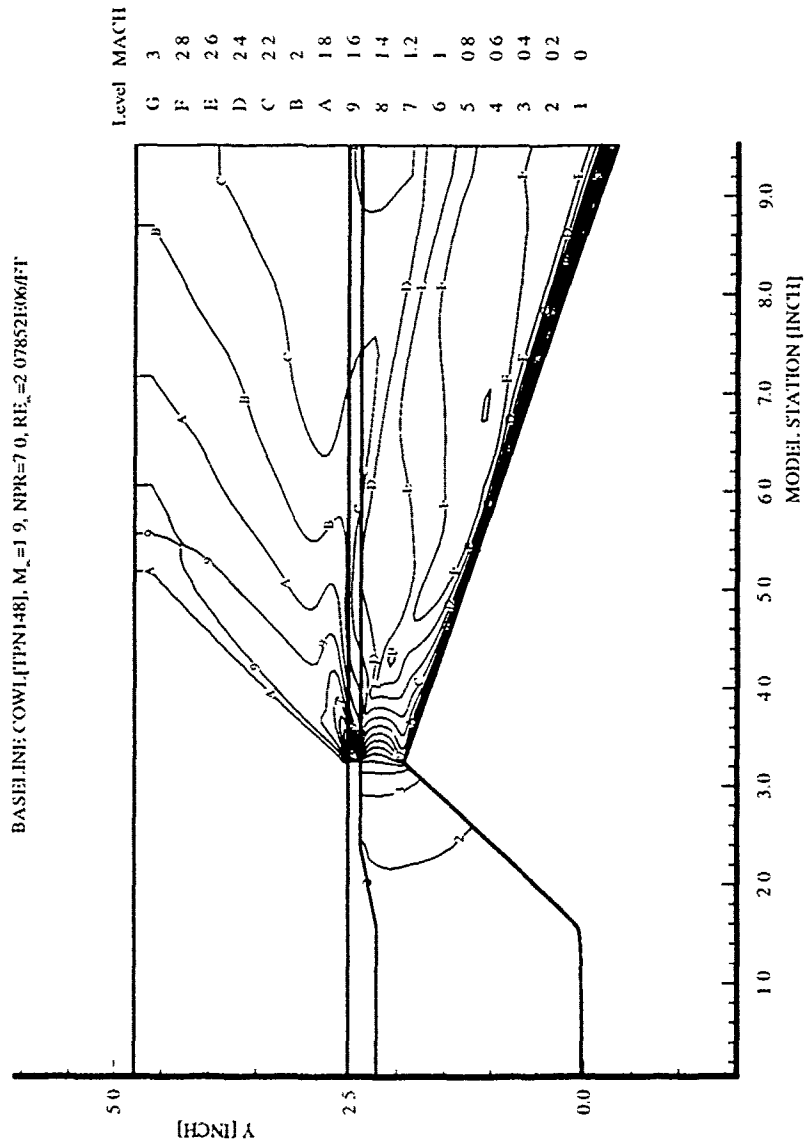


Figure D-7 Nozzle/Afterbody Mach Number Contour: Baseline Cowl, $M_\infty=1.9$, NPR=7.0

NOZZLE/COWL MACH NUMBER CONTOUR

BASILINE COWL [TPN180], $M_\infty=3.0$, NPR=7.0, $Re_\infty=2.02096 \times 10^6$

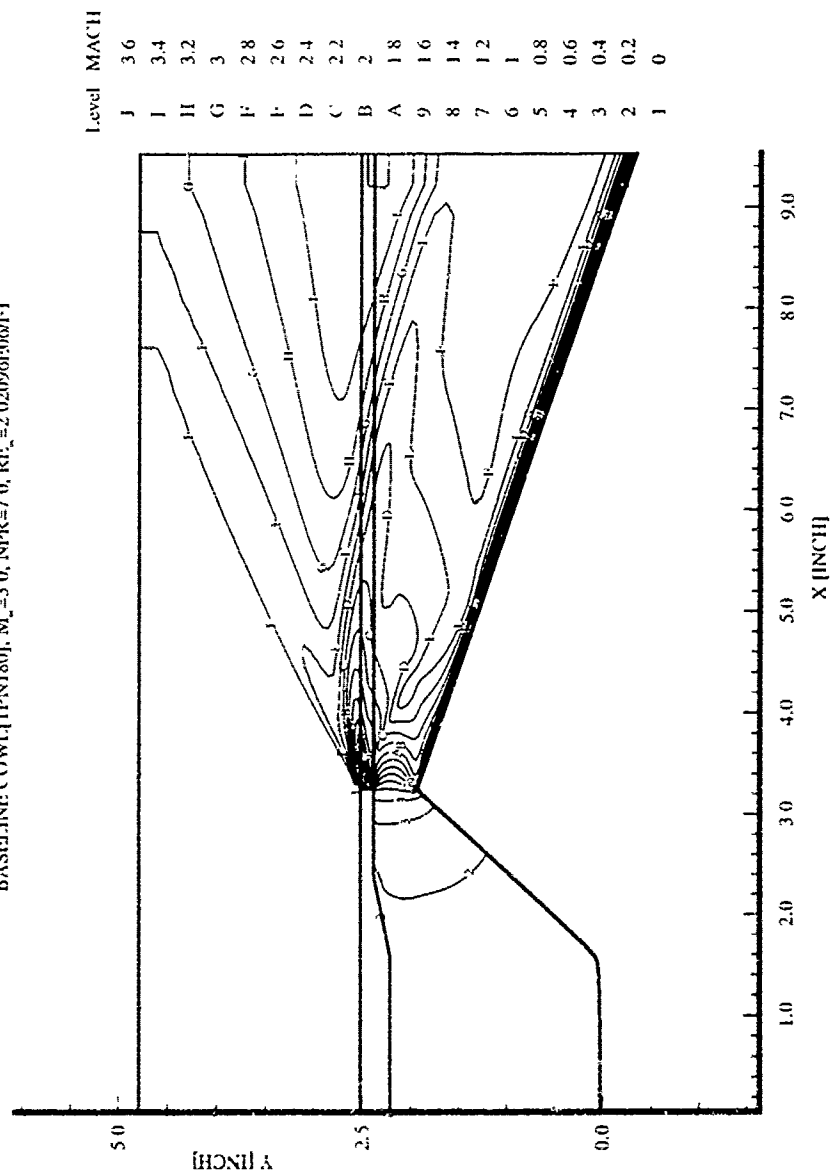


Figure D-8 Nozzle/Afterbody Mach Number Contour: Baseline Cowl, $M_\infty=3.0$, NPR=7.0

NOZZLE/COWL MACH NUMBER CONTOUR

BASIS LINE COWL (IPN147), $M_\infty=1.9$, NPR=12.0, $Re_\infty=2.093281 \times 10^6$

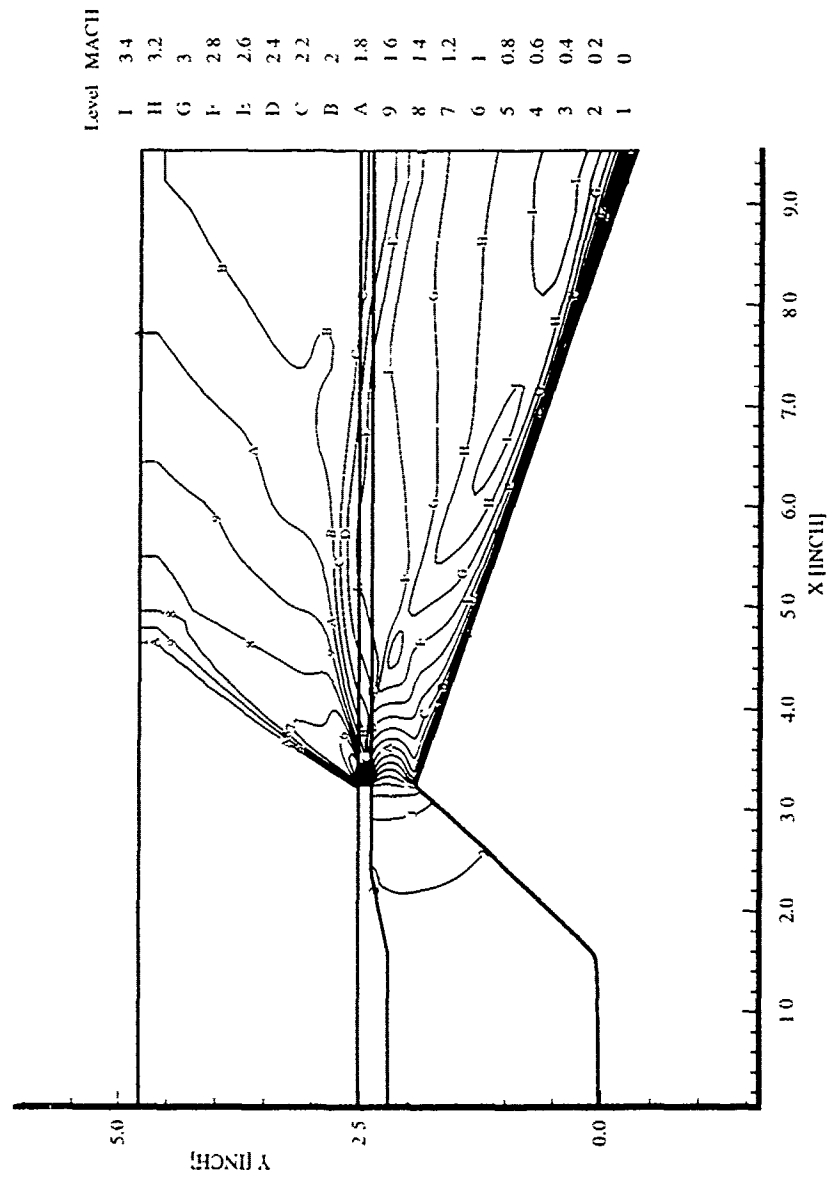


Figure D-9 Nozzle/Afterbody Mach Number Contour: Baseline Cowl, $M_\infty=1.9$, NPR=12.0

NOZZLE/COWL, MACH NUMBER CONTOUR

BASILINE COWL, ITPN183, $M_\infty=3.0$, NPR=12.0, $Re_\infty=2.03679 \times 10^6$ FT

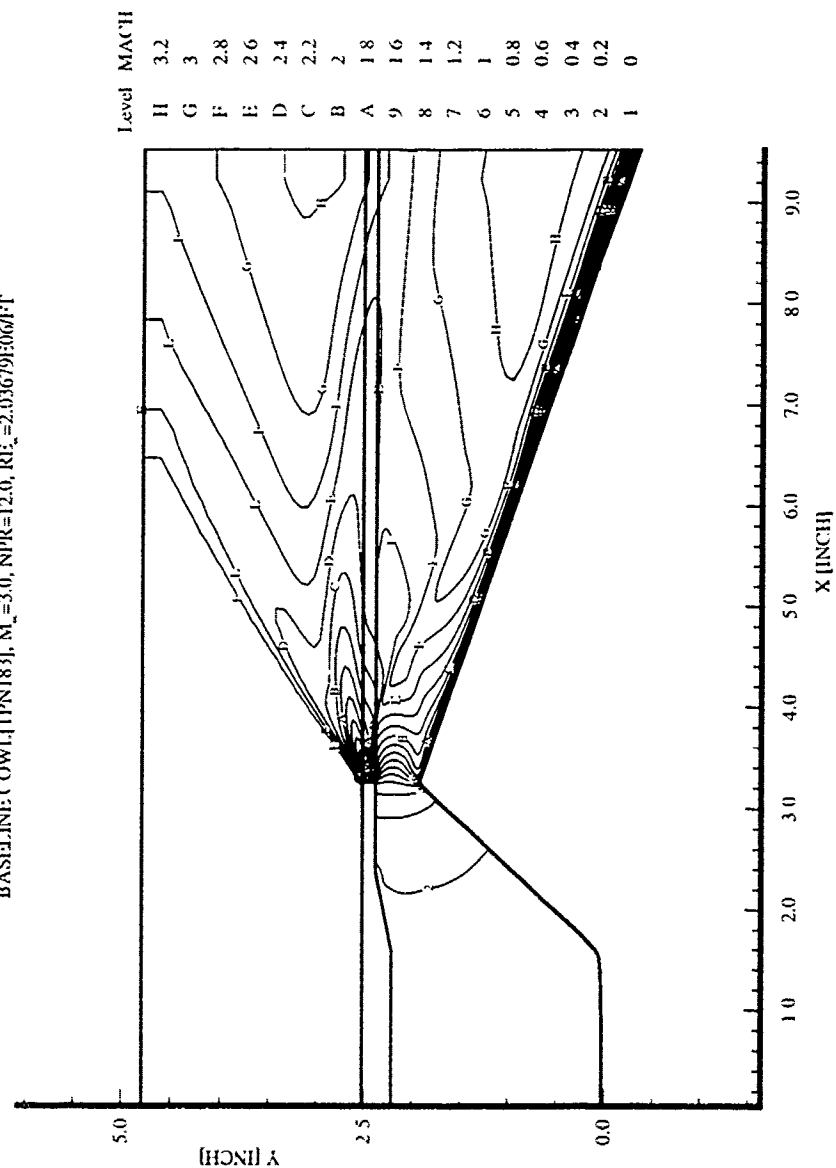


Figure D-10 Nozzle/Afterbody Mach Number Contour: Baseline Cowl, $M_\infty=3.0$, NPR=12.0

NOZZLE/COWL MACH NUMBER CONTOUR

LONG COWL [TPN160], $M_\infty = 1.9$, $NPR = 7.0$, $Re_\infty = 2.00984 \times 10^6 / ft$

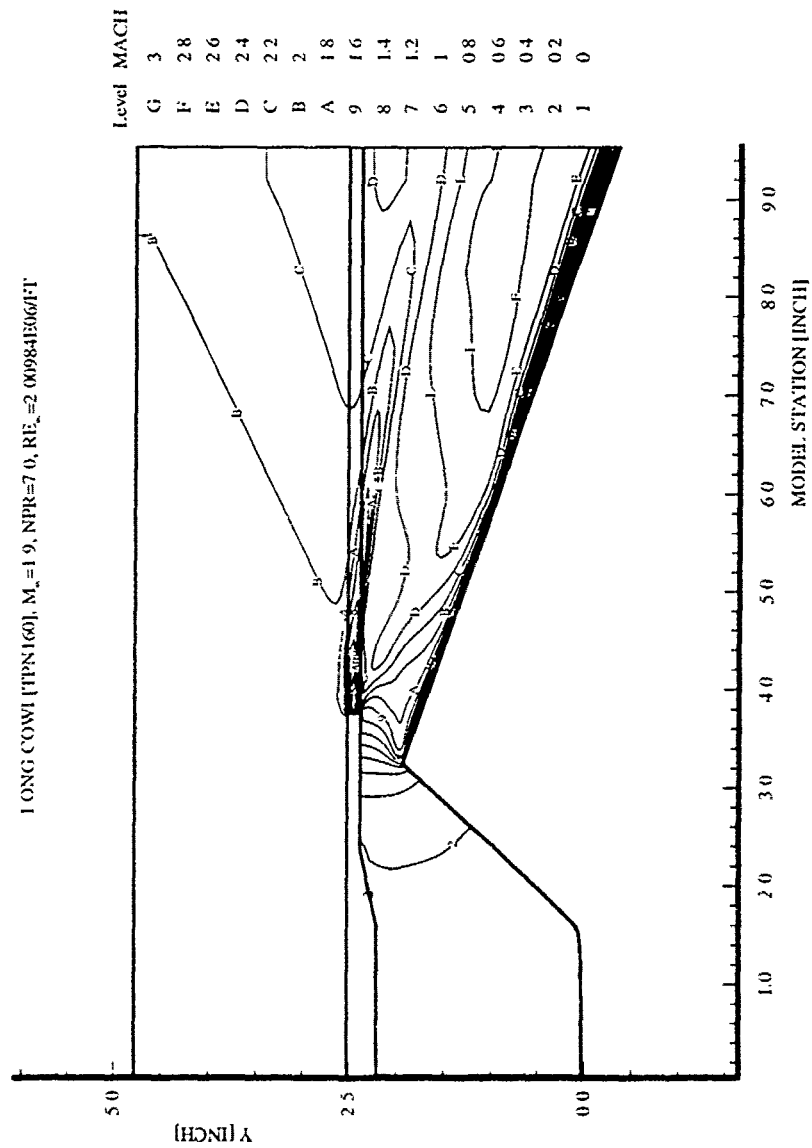


Figure D-11 Nozzle/Afterbody Mach Number Contour: Long Cowl, $M_\infty = 1.9$, $NPR = 7.0$

NOZZLE/COWL MACH NUMBER CONTOUR

+5 DEGREE COWL [TPN172], $M_\infty = 1.9$, NPR=7.0, $Re_\infty = 2.0231 \times 10^6/ft$

Level	MACH
O	4.6
N	4.4
M	4.2
L	4
K	3.8
J	3.6
I	3.4
H	3.2
G	3
F	2.8
E	2.6
D	2.4
C	2.2
B	2
A	1.8
9	1.6
8	1.4
7	1.2
6	1
5	0.8
4	0.6
3	0.4
2	0.2
1	0

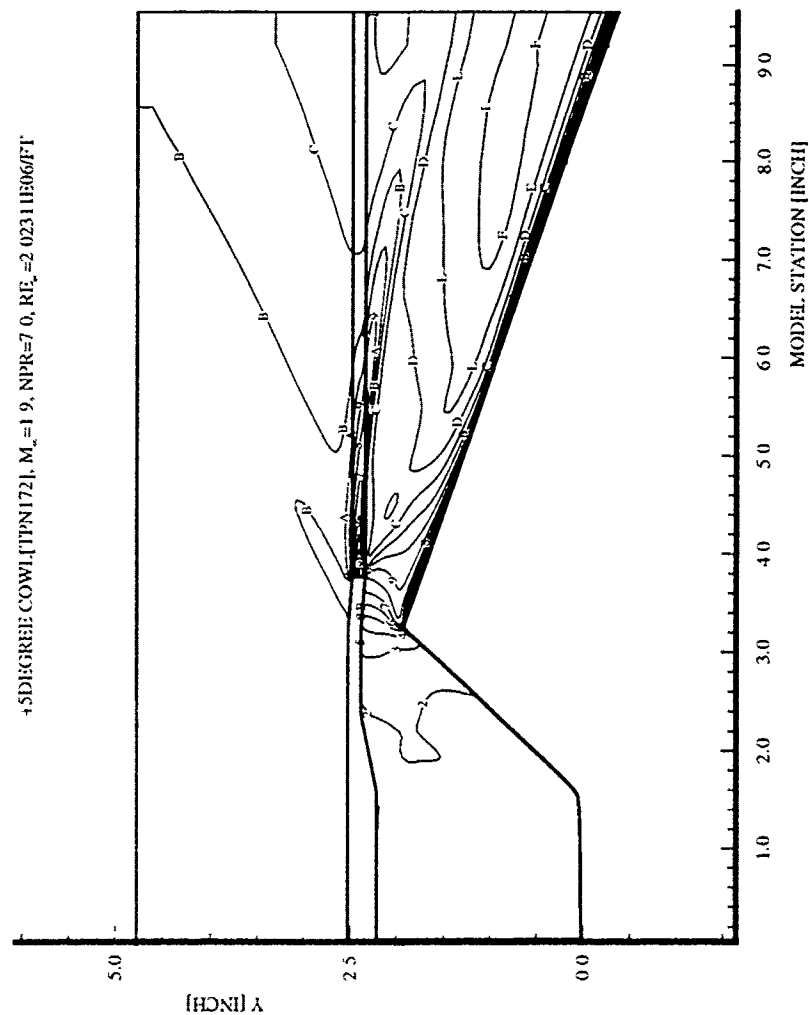


Figure D-12 Nozzle/Afterbody Mach Number Contour: +5 Degree Cowl, $M_\infty=1.9$, NPR=7.0

NOZZLE/COWL MACH NUMBER CONTOUR

-5 DEGREE COWL, $M_\infty=1.9$, $NPR=7.0$, $Re_\infty=2.04299 \times 10^6 ft^{-1}$

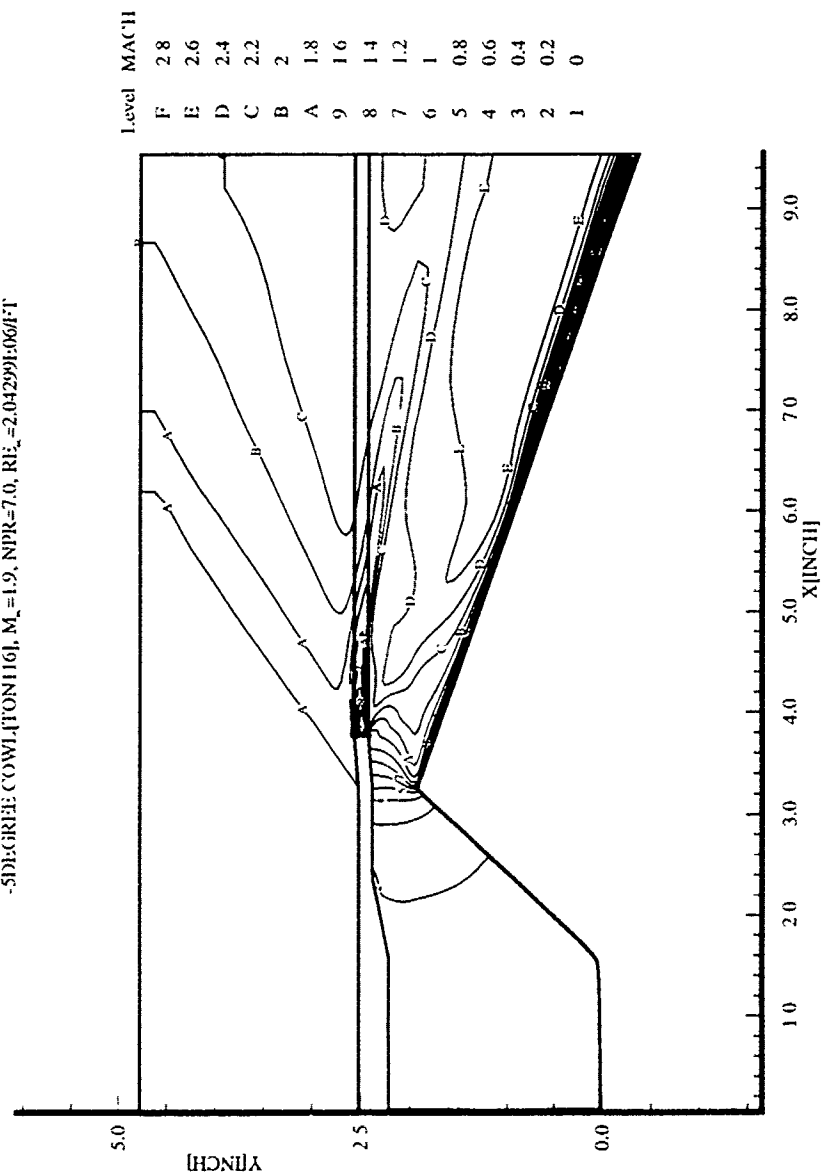


Figure D-13 Nozzle/Afterbody Mach Number Contour: -5 Degree Cowl, $M_\infty=1.9$, $NPR=7.0$

NOZZLE/COWL MACH NUMBER CONTOUR

BASILINE COWL [TPN184], $M_\infty=3.0$, NPR=16.0, $Re_\infty=2.03757E6/l^*$

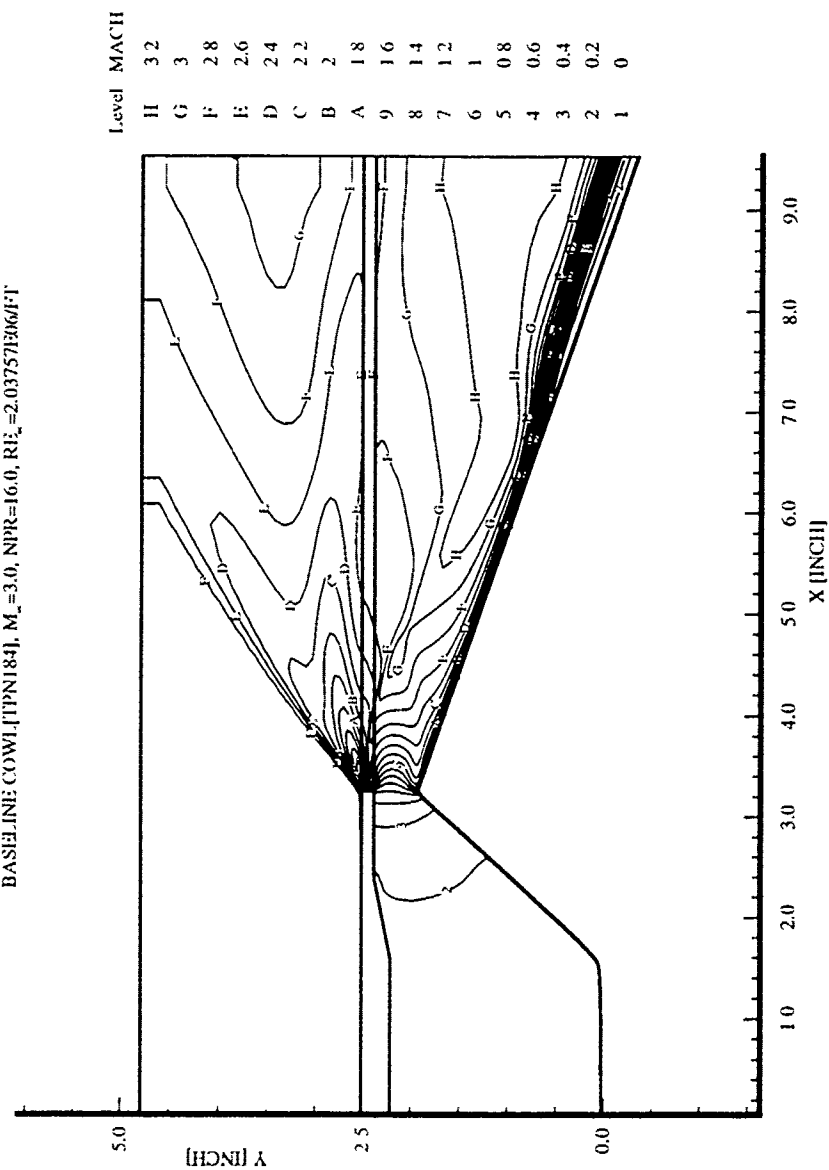


Figure D-14 Nozzle/Afterbody Mach Number Contour: Baseline Cowl, $M_\infty=3.0$, NPR=16.0

NOZZLE/COWL MACH NUMBER CONTOUR

LONG COWL, [TPN212], $M_\infty=3.0$, NPR=16.0, $Re_\infty=1.99574 \times 10^6$ / ft

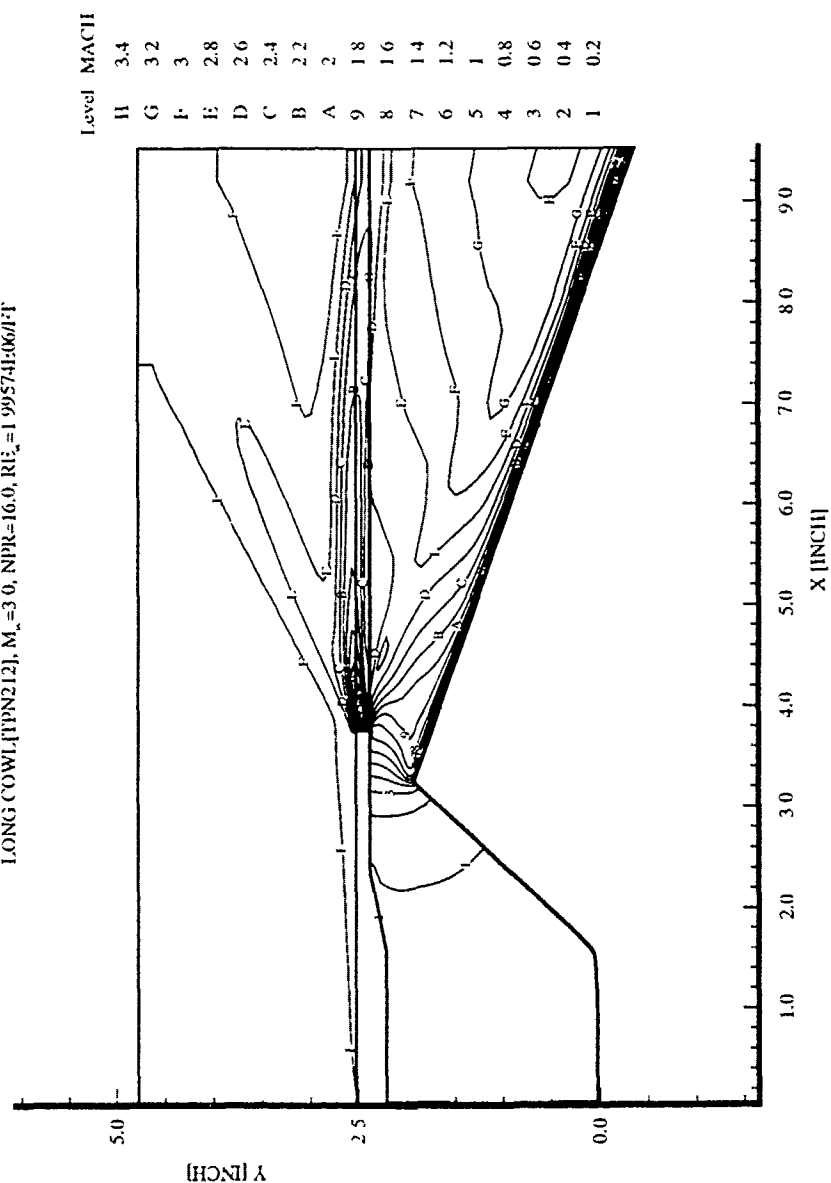


Figure D-15 Nozzle/Afterbody Mach Number Contour: Long Cowl, $M_\infty=3.0$, NPR=16.0

NOZZLE/COWL MACH NUMBER CONTOUR

+5 DEGREE COWL [TPN199], $M_\infty=3.0$, NPR=16.0, $R_{LE}=2.0176613064 \cdot 10^{-6}$

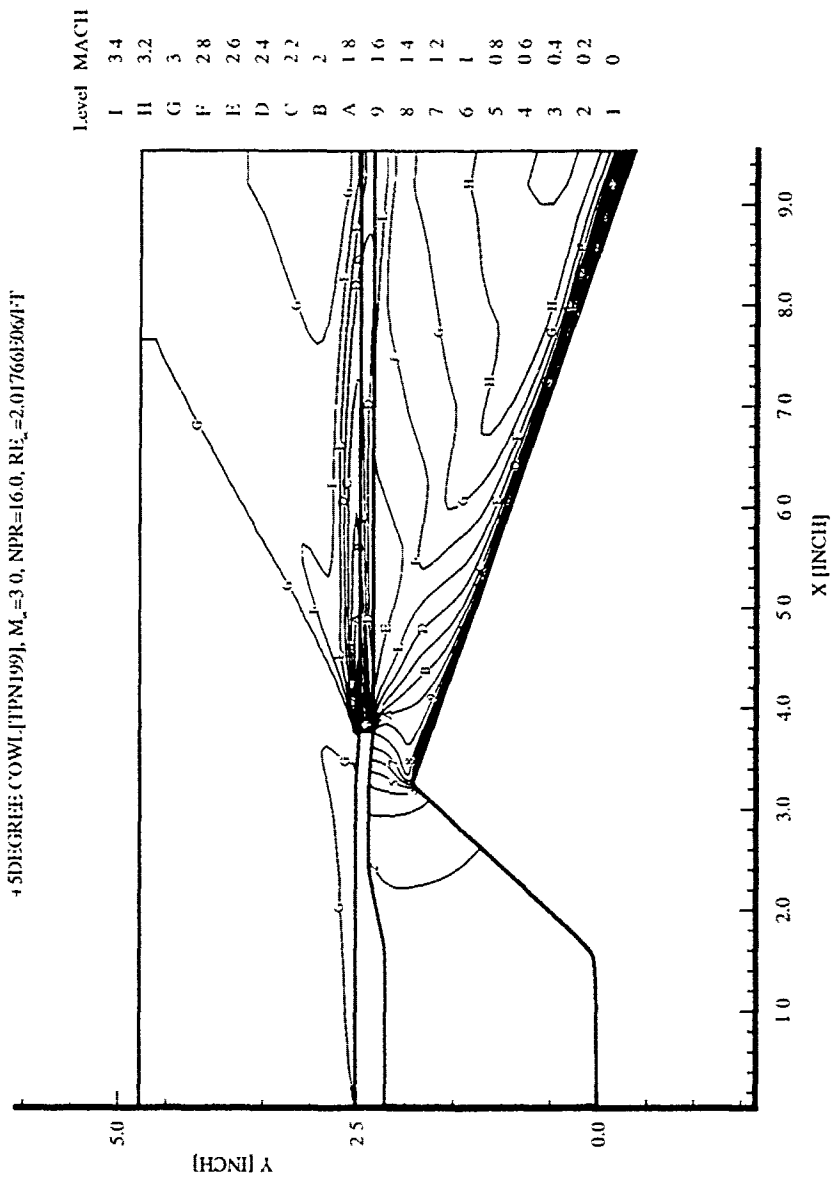


Figure D-16 Nozzle/Afterbody Mach Number Contour: +5 Degree Cowl, $M_\infty=3.0$, NPR=16.0

Vita

Yonghee Hyun was born on June 7, 1960, in Kwangju, the Republic of Korea and graduated from Song-Won Senior High School in 1979. He entered the Korean Air Force Academy and graduated with a Bachelor of Science in Aeronautical Engineering. After graduation from the Korean Air Force Academy, he was trained as a Weapons System Officer for one year and was assigned to the 153th Fighter Squadron, 17th Tactical Fighter Wing of the Korean Air Force in April 1983. His second assignment was as instructor of Electronic Warfare Officers at the 29th Tactical Fighter Weapons Group (like Fighter Weapons School in the United States Air Force). After three years of service at the 29th Group, he entered the U.S. Air Force Institute of Technology in June 1991.

REPORT DOCUMENTATION PAGE

Form Approved
JMI No. 9704-01864. AUTHOR: Yonghee Hyun, Major, ROKAF
5. REPORT TYPE AND DATE COVERED: Master's Thesis
6. PERFORMING ORGANIZATION NAME(S) AND ADDRESS(ES): Air Force Institute of Technology
Wright-Patterson AFB, OH 45433-7765
7. PERFORMING ORGANIZATION REPORT NUMBER: AFIT/GAE/ENY/93J-02
8. SPONSORING MONITORING AGENCY NAME(S) AND ADDRESS(ES):
9. SPONSORING MONITORING AGENCY REPORT NUMBER:
10. DISTRIBUTION CODE: UL

1. TITLE AND SUBTITLE: A Comparison of Computational and Experimental Data for a Subscale High Speed Propulsive Nozzle at Low Mach Numbers

2. FUNDING NUMBERS

3. AUTHOR(S)

Yonghee Hyun, Major, ROKAF

4. PERFORMING ORGANIZATION NAME(S) AND ADDRESS(ES):

Air Force Institute of Technology
Wright-Patterson AFB, OH 45433-77656. PERFORMING ORGANIZATION
REPORT NUMBER

AFIT/GAE/ENY/93J-02

8. SPONSORING MONITORING AGENCY NAME(S) AND ADDRESS(ES):

10. SPONSORING MONITORING
AGENCY REPORT NUMBERApproved for public release; distribution
unlimited

This computational study of a hypersonic sub-scale nozzle/cowl configuration compares numerical solutions with experimental data for nozzle performance at off design conditions (subsonic through supersonic Mach numbers). A combination of Van Leer and Roe flux-splitting algorithms was used to solve the flow field. The explicit formulation assumed laminar planar flow and the perfect gas equation of state. A validation for the numerical algorithm was accomplished by comparing with experimental data for a variety of cases. Grid refinement, geometry, and operating conditions all influenced the comparison of the experimental and computational data. Generally, as the Mach number and nozzle pressure ratio increased, the consistency between the experimental results showed better agreement, although the computational investigation was performed on the basis of planar, laminar flow. For the different cowl configurations, the results for baseline and -5 degree cowl show a better agreement than the long and +5 degree cowl.

14. SUBJECT TERMS
Hypersonic Nozzle, Navier-Stokes Solutions, Laminar, Unsteady Flow, Flux-Vector Splitting, Flux Difference Splitting15. NUMBER OF PAGES
148

16. PRICE CODE

17. SECURITY CLASSIFICATION
OF REPORT

Unclassified

18. SECURITY CLASSIFICATION
OF THIS PAGE

Unclassified

19. SECURITY CLASSIFICATION
OF ABSTRACT

Unclassified

20. LIMITATION OF ABSTRACT

UL